Numerical Simulation of a Convergent Divergent Supersonic Nozzle Flow

by

Ekanayake, E. M. Sudharshani

B.Aero Eng.(Hons) (RMIT University)

Dissertation submitted in fulfilment of the requirements for the Master of Science (Applied Mathematics)

School of Mathematical and Geospatial Sciences

RMIT University

Melbourne

Australia

July 15, 2013

DECLARATION

The candidate hereby declares that the work in this thesis, presented for the award of the Master Degree and submitted in the School of Mathematical and Geospatial Sciences, RMIT University:

- **has been done by the candidate alone and has not been submitted previously, in whole or in part, in respect of any other academic award and has not been published in any form by any other person except where due reference is given, and**
- **has been carried out under the supervision of Dr. Yan Ding and Dr. John A. Gear**

.....

Ekanayake, E.M.Sudharshani

Certification

This is to certify that the above statements made by the candidate are correct to the best of our knowledge.

.....

Dr. Yan Ding

Supervisor

.....

Dr. John A. Gear

Supervisor

Acknowledgements

I would like to thank my supervisors Dr. Yan Ding and Dr. John A Gear, senior lecturers at the School of Mathematics and Geospatial Sciences, RMIT University for supporting me theoretically and practically to successfully complete this project.

I welcome this opportunity to thank my supervisor Dr. Yan Ding for giving me the opportunity to conduct this research and helping me to receive a RTS scholarship by RMIT University to pursuer this project. I would like to again thank my supervisors for their support, encouragement and belief during this project, which was solely pursued due to my interest in the topic.

I would also like to acknowledge the School of Mathematics and Geospatial Sciences and Graduate Research Office (GRO), RMIT University for the financial support to represent RMIT University at the Engineering Mathematics and Applications Conference (EMAC), 2009 in Adelaide, Australia and 17th Australasian Fluid Mechanics Conference, 2010 in Auckland, New Zealand.

I would also like to thank my beloved family, Saliya , Dharshanika Ekanayake and my sister-in-law Jimeal R Ekanayake and friends, notably Cynthia Andrews who helped me through this journey.

I would like to dedicate this thesis to my father, the late E.M. Abeysingha Banda who passed away in a horrific car accident in May 1982 and my mother, Mallika Ekanayake who made countless sacrifices as a single mother to fulfil her duties.

Contents

List of Figures

List of Tables

Publications

[1] Ekanayake, E.M.S., Gear, J.A., and Ding, Y. *Flow simulation of a two dimensional rectangular supersonic convergent divergent nozzle.* ANZIAM Journal Vol. 51. (EMAC2009), pp. C377-C392, 2010.
http://anziamj.austms.org.au/ojs/index.php/ANZIAMJ/article/view/2577

[2] 17th Australasian Fluid Mechanics Conference Proceedings, 2010. Ekanayake, E.M.S., Gear, J.A., and Ding, Y. *Numerical Simulation of a Supersonic Convergent Divergent nozzle with Divergent angle variations for Underexpanded Condition.*
http://www.mech.unimelb.edu.au/people/staffresearch/AFMS/17/327_Paper.pdf

Nomenclature

A_t	–	*nozzle throat area*
A_e	–	*nozzle exit area*
AR	–	*Aspect ratio*
CD	–	*Covergent Diveregent*
NAR	–	*Nozzle Area Ratio* (A_e/A_t)
NPR	–	*Nozzle Pressure Ratio* (P_{res}/P_a)
P_{res}	–	*resevoiur pressure*
P_a	–	*ambient pressure*
U_i	–	*mean velocity componant of turbulence at point i*
$u_i(t)$	–	*fluctuating velocity componant of turbulent at a variable point i,(t)*
y^+	–	*non – dimentional distance from the 1st wall – adjacent grid point to the wall*
u^*	–	*friction velocity*
δ	–	*boundary layer thickness*
R_e	–	*Reynolds number*
$\dot{q}$	–	*rate of heat added to a system*
$\mathbf{V}$	–	*Velocity vector of u,v,w componants in x, y, z directions*
u,v,w	–	*velocity componants in x, y, z directions respectively*
$\nabla\bullet$	–	*divergence property of a variable*
Ω	–	*volume of a cell (control volume)*
ω	–	*specific turbulence dissipation*
k	–	*turbulent kinetic energy*
ε	–	*turbulence dissipation rate*
e	–	*energy*
F_x,F_y,F_z	–	*surface forces in x, y, z directions*
SIBL	–	*Shock Induced Boundary Layer*
SWBLI	–	*Shock Wave Boundary Layer Interaction*
TKE	–	*Turbulent Kinetic Energy*
SST	–	*Shear Stress Transport*
RANS	–	*Reynolds Average Navier Stokes*

Summary

Supersonic nozzles have many applications in the aerospace industry, including high-speed military and combat jets, rocket nozzles and missiles. The traditional Convergent Divergent (CD) nozzle is a relatively simple devise used commonly among most jets and rocket nozzles. Depending on the requirement of the thrust and its applications, the geometrical configuration of the nozzle varies.

The shape of the nozzle is key to the expansion process, and plays a vital part towards designing the flow to minimise the thrust lost. It is crucial during engine performance the thrust generated by expanding the exhaust gas retains its maximum potential.

When gas is expanded through a CD nozzle supersonically, the flow undergoes many forms of unique phenomena, including flow separation, unsteadiness, flow mixing, turbulence, Shock Induced Boundary Layer (SIBL) separation and Mach Shock Diamonds. Some of these phenomena lead to energy loss, thereby reducing the overall thrust generated by the nozzle. The thrust loss due to shock waves and boundary layer separations generated internally in the nozzle region remains poorly understood, hence failed to reach maximum potential of an engine.

To reach its functional potential, the design of an exhaust nozzle serves two main purposes. Firstly, to control engine exit pressure to reach to ideal design conditions, which could be achieved by varying the Nozzle Area Ratio (NAR), the area of the nozzle exit over that of nozzle throat. Secondly, to convert the potential energy of the expanding gas into kinetic energy efficiently.

In this research, two nozzle configurations, with two symmetric and two asymmetric geometry shapes are investigated. In order to investigate the influence of an asymmetric geometry shape over symmetric on nozzle performance, contraction angles at the throat of the divergent section to the symmetric geometry shape is introduced. The numerical analysis is focused on the influence of the nozzle geometry, the NAR and Nozzle Pressure Ratio (NPR) on the flow properties downstream (divergent section) and the external (jet plume) region of the nozzle. The main focus of this research is on nozzles operating at a high NPR to investigate the formation of the jet plume shocks and direction of the expanding gas of the asymmetric nozzle shapes.

The two symmetric model configurations, NAR 1.5 and NAR 1.66, have a divergent angle at the throat of 2.801 and 3.89 degrees respectively. The two asymmetric geometry configurations,

NAR 1.14 and 1.21, consists a divergent angle of 2.801 degrees at the throat with contraction angle variations in the divergent section. The asymmetric nozzle NAR 1.14 is comprised of two contraction variations angles of 29.64 and 2.801 degrees at the bottom wall, while NAR 1.21 consists of two contraction angle variations of 8 and 15 degrees at the top and bottom walls of the nozzle, respectively.

ANSYS CFX is used to solve time-dependent RANS (Reynolds Average Navier Stokes) equations for the supersonic two dimensional (2D) nozzle flow, together with the Shear Stress Transport (SST) turbulence model. Capturing the boundary layer flow characteristics under strong adverse pressure gradients is of particular interest of separated flows. The SST model has transcended in performance that captures the instability characteristics such as *Lambda* shock waves, *Reflection* and *Incident* shocks, as well as boundary layer separation, re-circulation zones, shear layer stresses caused by strong adverse pressure gradients accurately.

The NPR for both symmetric and asymmetric are varied between 1.27 - 12 under sea-level conditions. In the first stage of the numerical simulation, the flow characteristics under low NPRs (1.27 - 2.4) are tested to investigate the internal flow separations and shocks. The second stage of the numerical simulation focusses on nozzle operating at higher NPRs varying between 3.4 - 12.0 to investigate the jet flow patterns at the plume regions and deflection properties. The NAR is varied to investigate the gas flow direction and speed, for the asymmetric nozzle in *Underexpanded* conditions at high NPRs. Computational results obtained under low NPRs between 1.27 - 2.4 for symmetric models NAR 1.5, 1.66 is closely validated with the results presented by Xiao, et al solved for Mach numbers for separation of the supersonic flow, for models NAR 1.5 [31] and NAR 1.66 [32]. Internal nozzle flow separation, boundary layer separation and *Lambda* shocks under adverse pressure gradients were further verified with the computational results presented under low NPRs Xiao, et al [31], [32].

Investigation carried among the two symmetric nozzle geometries (NAR 1.21 and 1.14) at low NPRs, the internal shock patterns have taken a different structure for asymmetric model, NAR 1.21. Typical *Lambda* shocks associated to internal flow separation was not observed for the asymmetry type model, NAR 1.21 consisting contraction angles at both top and bottom walls. At high NPRs, the Mach contour values of the asymmetric nozzle, NAR 1.21 is slightly less than of asymmetric model NAR 1.14. However, overall the asymmetric nozzle type, NAR 1.21 have produced Mach numbers lesser in value than of symmetric models for a given NPR. The asymmetric type, NAR 1.14 generated the highest Mach number values when the nozzle

is highly *Underexpanded*. The shock waves become more enlarged as the nozzle pressure is increased for a given distance of the jet plume region, of the asymmetric models in comparison to the symmetric nozzles. The size of the Mach disks and the free jet boundary tend to increase with the increase of NPR for both symmetric and asymmetric models. Mach disk diameters are high in asymmetric nozzles in comparison to symmetric models in high *Underexpanded* conditions. When varying the divergent section of the asymmetric nozzles, the flow path is vectored away from the axis line at high NPRs. The flow is significantly offset in the desired direction and is considerably different from the traditional Mach Diamond shock patterns observed in symmetric nozzle shapes at the jet plume region.

Asymmetric nozzle geometries have a major contribution towards the size of the Mach disks and Diamond shock patterns within the jet plume region. This variation observed in asymmetric nozzle, where contraction angles are introduced to both top and bottom nozzle walls, could be implemented to direct the exhaust flow in the desired path in a jet nozzle during sharp turns. Another possible suggestion would be on a missile nozzle configurations, the variation on both top and bottom walls may enhance to vector the thrust when navigating through parabolic trajectories. Varying the angle of the top and the bottom walls has a significant effect on the exhaust flow direction. This could be implemented in future high speed nozzle designs.

Chapter 1

Introduction

1.1 General Overview of the Problem and Motivation

The Convergent Divergent (CD) nozzle is a major deign configuration within a jet propulsion system that plays a vital role for a vehicle operating under supersonic conditions. The shape of the nozzle is critical for designing a nozzle configuration for high speed aircrafts to minimise thrust loss and expand the exhaust gas supersonically to maximise its potential. Performance of the vehicle predominately depends on the configuration of the divergent section, which ensures that the direction of the escaping gases is directly backwards, as any sideways components would not contribute to thrust.

The gas is expanded through a CD nozzle from subsonic to supersonic conditions, the flow under goes many forms of unique phenomena that increase the kinetic energy including flow separation, unsteadiness, flow mixing, Shock Induced Boundary Layer (SIBL) separation and Mach shock Diamonds. Some of these phenomena may lead to pressure loss, thereby reduce the overall thrust generated by the nozzle. Additionally when the flow of the nozzle is either *Overexpanded* or *Underexpanded*, the loss in thrust due to Mach shock Diamonds makes the nozzle less efficient [16, 21, 25, 31]. Past investigations have shown that flow phenomena occurring internally (shocks and flow separations) and externally (Mach shock Diamonds) to the nozzle still carry many performance draw backs which remain unsolved.

To reach its functional potential the design of an exhaust nozzle serves two main purposes. First, it controls engine back pressure to reach ideal design conditions, which is accomplished through nozzle area variations. Second, the design converts potential energy of the expanding

gas to kinetic energy by accelerating the exhaust gas, which accomplished by efficiently expanding the gases to the ambient pressure [16]. To obtain a maximum thrust at a given pressure ratio, theoretically the exit pressure should be equal to the external ambient pressure. For a vehicle operating at a constant pressure, the gas can be expanded for the design conditions only at one altitude, which is unrealistic to maintain in real operating environments.

Majority of the past literature is focused on internal flow instabilities. The limited focus has been on the flow properties of the divergent section (internal flow) of an symmetric nozzle shapes [19],[20],[21],[25], [28],[27],[31],[32],[33]. Little focus has been given towards the instabilities associated with the jet plume region (external region) and Mach Diamond Shocks under higher NPRs (*Underexpanded condition*). The flow characteristics associated with an asymmetric geometry configuration under supersonic conditions has been less favorable in past, hence focus onto this project is initiated. Most literature on experimental and computational studies carried out by varying the NARs of the nozzle have been performed in typical conventional CD nozzles under low NPRs [19],[31],[32],[33]. Possible optimisations that could be made at the conceptual level through initial geometry design configurations were identified and investigated during this project. Flow expanding through an asymmetric nozzle and its influences on the flow properties downstream is focused.

The project mainly focuses on emphasising the design optimisations of the nozzle geometry, hence the outcomes towards efficiency of the expanding exhaust gas and thrust properties. Varying the nozzle divergent angle, the exit contraction angle and the NAR are some of the possible design configurations to the divergent section of the traditional CD nozzle. The symmetric and asymmetric models are simulated for both low (1.27 - 2.7) and high (3.4 - 12.0) NPRs at sea-level conditions.

The geometry variations made at the divergent section of the nozzle is analysed which may help to reduce internal characteristics of the nozzle flow, boundary layer separation, shock induced separation and reverse flow, separation bubbles when exhaust gas is expanded to supersonic conditions.

1.2 Model Basis and Problem Approach

The model basis is developed to improve the divergent flow properties. This include the internal and external flow characteristics influenced by the changes with the geometry associated. The

design configurations of the divergent section of the CD nozzle are motivated by a few factors, which are the loss in thrust, flow properties of the expanding gas, asymmetric geometry study and lack of research conducted under supersonic flow conditions.

In this thesis, a total of four model cases were studied, with two symmetric and two asymmetric models. The four model shapes are shown in the Figure 1.1. As illustrated in Figure 1.1(1a), the nozzle shape is a traditional symmetric CD nozzle with a divergent angle of 2.801 degrees. The shape of the **Model 1a (NAR 1.5)** is based on the nozzle geometry configuration investigated under supersonic condition for NAR varying between 1.0 - 1.8 in the literature [28],[31],[33].

In this thesis, **Model 1a (NAR 1.5)** is used as a base model. Asymmetry (See Figure 1.1(b) and Figure 1.1(c) introduced to the base model is to understand the issue of reduction in internal flow separation and shock generation and establish some new design configurations to increase the Mach numbers of the flow downstream and deflection of the expanding gas. Based on dimensions described in [28],[31],[33], a base CD nozzle geometry shape, NAR 1.5 is chosen with a divergent length of 117 mm and throat height of 22.9 mm. Convergent length of the nozzle is 150 mm from the throat of the nozzle. Using these dimensions as consistent lengths for all models, the divergent angle at the throat and a contraction angle variation at the top and bottom walls were introduced. A detail description of the geometrical parameters selected for the four nozzle configurations are presented in Chapter 4.

To analyse the design at a conceptual level, geometry of the divergent section of the base model NAR 1.5 nozzle (see **Model 1a (NAR 1.66)**, Figure 1.1(1a)) are subjected to three approaches.

(1) Symmetric type : Increasing the divergent angle from 2.801 degrees to 3.89 degrees [31] (see **Model 1b**, Figure 1.1(1b)).

(2) Asymmetric type : Introducing contraction angles at the bottom wall at distances of l_1 and l_2 of the divergent section, while keeping the divergent angle at the throat unchanged (see **Model 2 (NAR 1.14)**, Figure 1.1(2)).

(3) Asymmetric type : Introducing contraction angles at the top and bottom walls at distances of l_3 and l_4 of the divergent section, while keeping the divergent angle at the throat unchanged (see **Model 3 (NAR 1.21)**, Figure 1.1(3)).

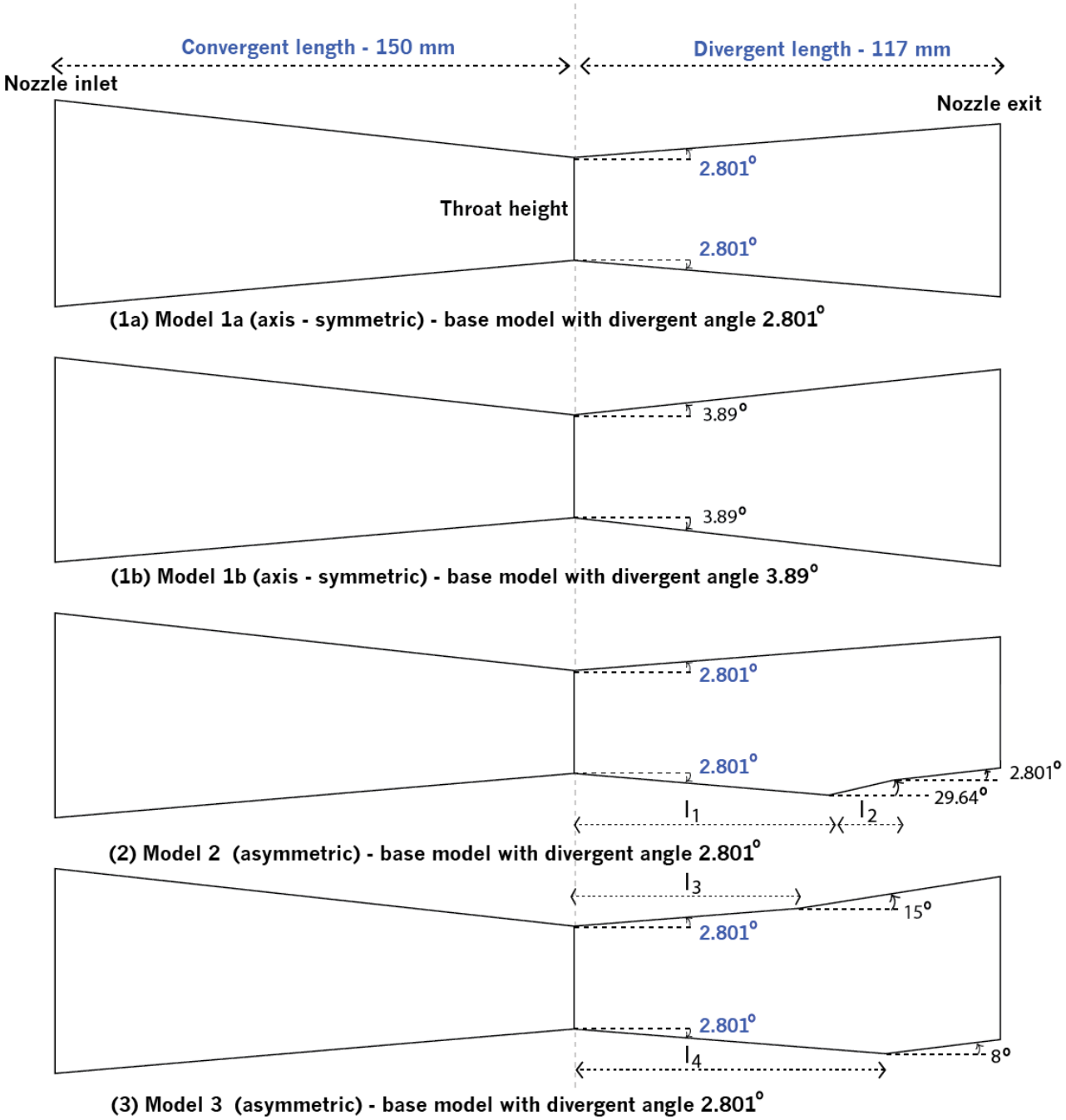

Figure 1.1: Geometry set-up: **Model 1a** (NAR 1.5), **Model 1b** (NAR 1.66), **Model 2** (NAR 1.14), **Model 3** (NAR 1.21).

The idea behind the introduction of the asymmetry at **Model 2** and **Model 3** through geometry variations to observe the changes in flow, hence investigate shock formations and flow separations at the divergent and the outside of the jet plume region.

The asymmetry models introduced through contraction angles in this thesis not been previously investigated, neither experimentally nor computationally to the best of my knowledge. The novel apparatus investigated during this study is distinct from all the other conventional convergent-divergent nozzles, consequently contributes to the understanding of the rationale between the internal and external flow structures and the nozzle geometry shapes.

1.3 Objective of the Study

This thesis investigate the relationship between the nozzle variations introduced at the divergent section and the influence of this variation towards expanding gas properties from a traditional symmetric CD nozzle.

The primary focus is to study the influence of asymmetry introduced through contraction angles of the divergent section of the traditional CD nozzle. The following objectives are focused:

The nozzle at high NPRs (3.4 - 12.0), the NAR of the traditional CD nozzle is varied to investigate the shock wave structure and other flow parameters, such as Mach numbers, the exhaust speeds of the jet flow, jet plume shocks, turbulent kinetic energies, flow velocity profiles and internal pressure variations of the symmetric and asymmetric nozzles. Varying NAR through contraction angles at high NPRs and its influence towards the nozzle exhaust direction (jet deflection angle) on asymmetric nozzle shapes is focused.

The nozzle at low NPRs (1.2 - 3.4), the contraction angles introduced to the divergent section of the nozzle (two asymmetric models) is to understand the flow structure at the divergent section of the nozzle. Asymmetry incorporated through parallel angle variations (contraction angles) to the top and bottom walls is simulated into this study to observe the internal shocks, flow separations. Trust loss in internal flow separation and shock formations contribute significantly towards reduction in velocity exiting the nozzle, hence, the this study focuses on the flow characteristics associated with internal flow separation that occurs under low NPRs, for asymmetric geometries. Further, as a key interest of this study, the formation of internal shocks such as *Lambda*, *Incident* and *Reflection* shocks in the asymmetric model

shapes under low NPRs is focused.

Due to the complexity of the flow phenomena, the aim is to establish some sensible knowledge about the degree of the influence between above mentioned flow properties and its performance on the asymmetric nozzle shapes, hence contribute some conceptual design ideas to future nozzle research. It was outside of the scope of this research to test the validity of this geometry variations (symmetric and asymmetric nozzles) through experimental analysis.

1.4 Outline of the Thesis

The subsequent chapters of this thesis are organised as follows:

- **Chapter 2** - Presents the physics behind the problem and the literature review of previous theoretical and experimental research conducted.
- **Chapter 3** - Describes the governing equations of gas dynamics, including the Reynolds Average Navier Stokes (RANS) equations. The chapter also discusses the nature of turbulence and turbulence models used with the research industry including the fundamental concepts behind the SST turbulence model.
- **Chapter 4** - Presents the computational model set-up in ANSYS CFX, including the geometry set-up, meshing, initial conditions, boundary and operating conditions and other modelling parameters.
- **Chapter 5** - Presents the comparison and discussion of the results for the traditional convergent divergent model with asymmetric nozzle with different area ratios.
- **Conclusion** - Describes the conclusions arising out of the research.

Chapter 2

A Literature Review on Fluid Flow through a Nozzle

2.1 Flow through Covergent-Divergent Nozzle

Supersonic Convergent-Divergent (CD) nozzles are used not only on military jets but also in rocket nozzles and significantly on current high speed missiles. The purpose of a jet nozzle is to convert thermal energy into kinetic energy to obtain high speed exhaust, and hence to propel the expanded gas along the desired direction.

Nozzles come in a variety of shapes depending on the application. The contour of the divergent section of a nozzle plays a crucial role in the expansion characteristics of the gas. The convergent section is designed with a bigger volume to receive the maximum mass flow into the nozzle. The flow is then compressed (total mass flow) at the throat and expanded to reach its ideal condition, through the divergent section of the nozzle.

Most nozzles within the aerospace discipline have a convergence section to build-up pressure that is from is highly heated exhaust gas accelerated from the combustion. To achieve the optimum performance, the shape of the divergence section may be either contoured convergent or divergent depending on the application. Some jet engines incorporate a simple *convergent* type nozzle, which consists of a convergent end downstream. When the *convergent* type nozzle is chocked some of the expansion takes place downstream in the jet wake [7]. Much of the gross thrust, produced from the jet momentum with additional thrust from pressure will generate an imbalance between the throat static pressure and atmospheric pressure. At high NPRs, the exit pressure is greater than ambient pressure and the expansion take place downstream of the

convergent nozzle, which is inefficient [7]. The expansion taking place outside the nozzle is improved using *narrow* convergent nozzle, which give high speed exhaust but reduced thrust, where as *wide* convergent nozzles give lower speed but produce higher thrust [7].

In contrast to *convergent* type nozzles, jet engines incorporating a CD nozzle will allow most of the expansion to take place inside of the nozzle to maximize the thrust [7]. The pressure

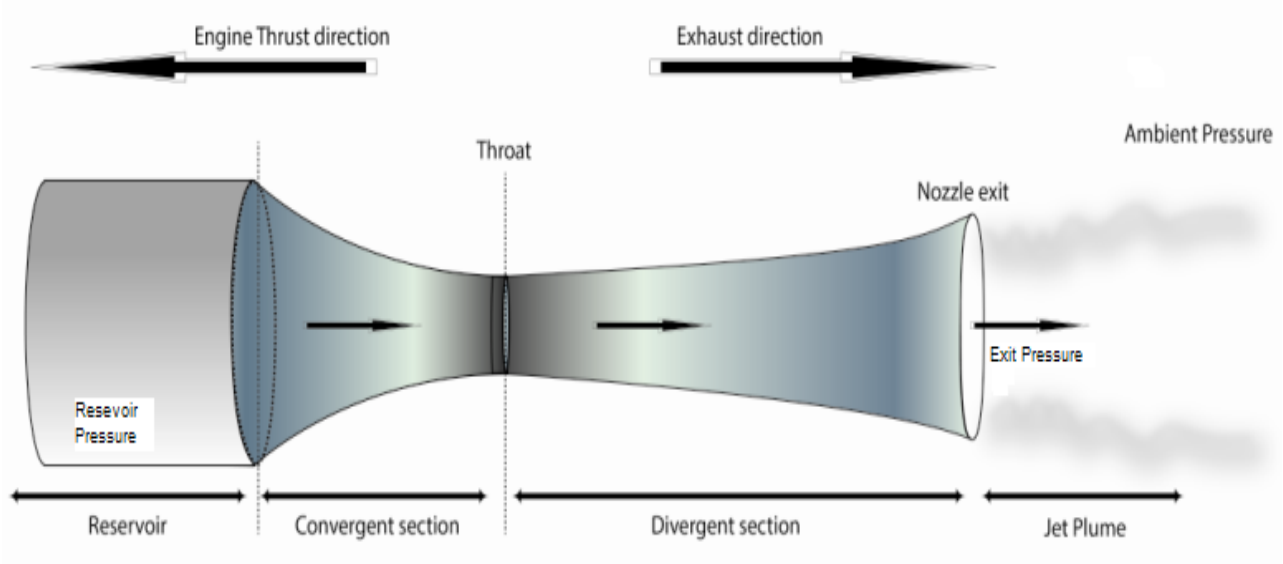

Figure 2.1: Typical Convergent-Divergent nozzle.

difference between the exit pressure P_e, in some literature also known as the back pressure P_0 and the reservoir pressure (P_{res}) makes the flow move from subsonic region to supersonic region through the nozzle (see Figure 2.1). This flow motion from convergent to divergent section is achieved, when the exit pressure (downstream flow) lower than the inlet pressure. A suitable correlation between NPR and NAR will expand the exhaust gas to supersonic flow with minimum thrust loss.

High pressure is at the convergent chamber/resevior of the nozzle, and low pressure at the exit of the nozzle. Here, we refer to the exit pressure (P_e) which is also the back pressure (P_0) as shown in Figure 2.1). The transformation of the flow, from subsonic to supersonic through a typical CD nozzle as illustrated in Figure 2.1, 2.2 undergoes the following seven steps:

(a) Upon lowering the exit pressure, the flow starts increasing speed. The flow at the throat and the divergent section is subsonic (see Figure 2.2(a)).

(b) On lowering the exit pressure further, the flow becomes *Choked* at the throat. The maximum flow rate occurs at the throat. Flow at the divergent section decelerates and is still

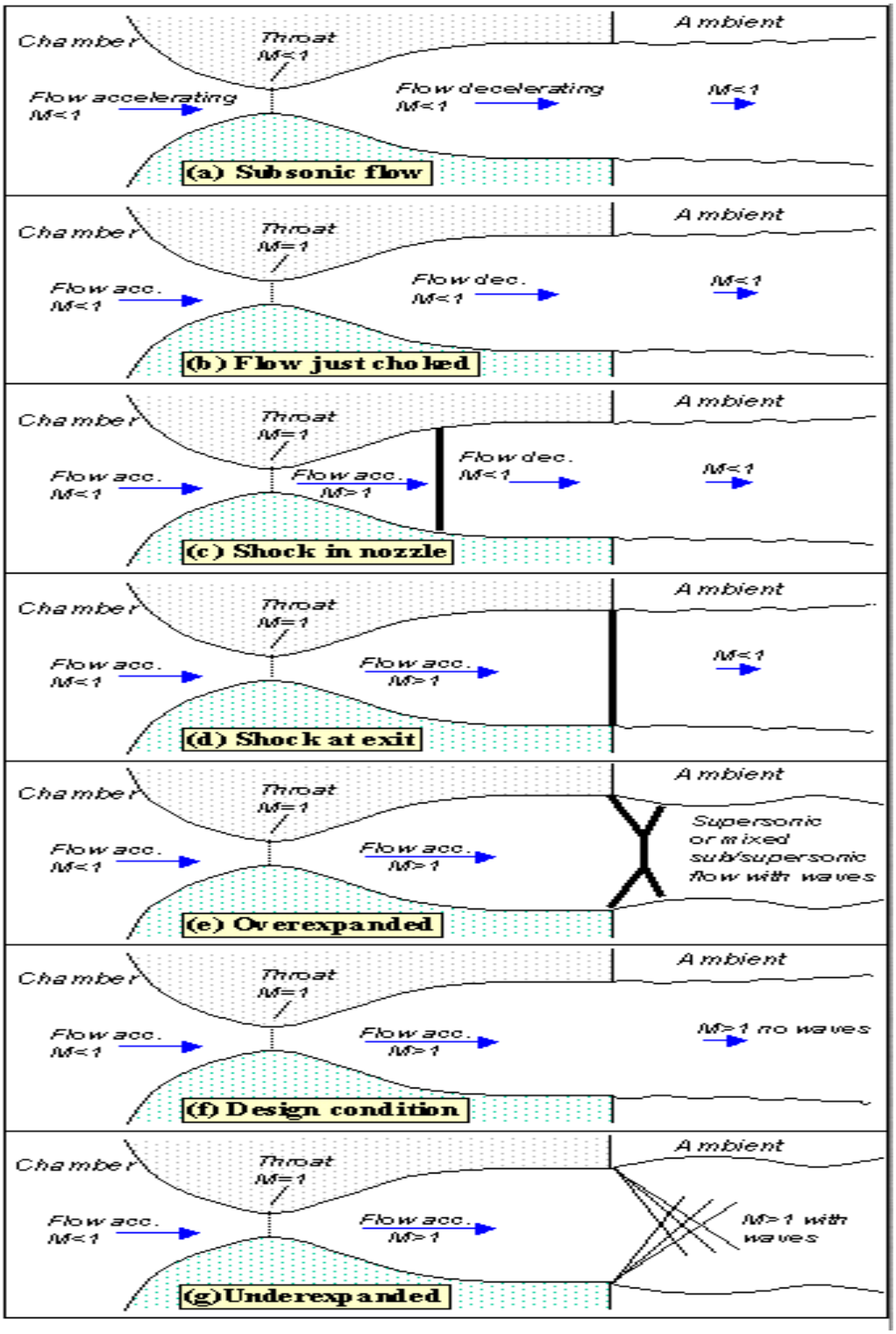

Figure 2.2: Graphical presentation of flow through a CD nozzle [3].

subsonic. Further lowering the back pressure will no longer increase the speed across the throat above Mach 1.0 (see Figure 2.2(b)).

(c) Lowering the exit pressure further accelerates the flow to supersonic speed in the divergent section of the nozzle, while at the throat the flow is still at Mach 1. This flow acceleration is terminated by the formation of a *Normal shock* created at the divergent section starting near the throat. Further lowering the back pressure makes this *Normal* shock move away from the throat downstream. The shock wave produces a near-instantaneous deceleration of the flow to subsonic speed (see Figure 2.2(c)). The pressure rises instantaneously across the shock.

(d) The *Normal* shock wave sitting at the throat moves downstream due to the further reduction of pressure and eventually reaches the exit of the nozzle, still remaining as a *Normal* shock wave. The flow behind the *Normal* shock is subsonic (see Figure 2.2(d)).

(e) Lowering the exit pressure causes the *Normal* shock wave at the exit of the nozzle to bend into the jet plume creating a complex flow pattern, with a mixture of subsonic and supersonic flows. *Normal* shock wave will turn oblique at the exit of the nozzle wall. The shock reflects inward to the jet plume region contracts the jet, a condition known as *Overexpansion* of the nozzle (see Figure 2.2(e)).

(f) Lowering the exit pressure further we obtain the ideal design condition, where flow is uniformly supersonic. Continuous thrust is achieved, and the nozzle exit pressure is equal to external ambient pressure. The flow remains supersonic in the exhaust plume and is shock free (see Figure 2.2(f)).

(g) Lowering the exit pressure further generates a new imbalance between the exit pressure of the nozzle and the ambient pressure. A new expansion waves forms at the nozzle exit, initially turning the flow at the jet edges outward to the plume region and setting up a different type of complex wave pattern. This condition is known as the *Underexpansion* of the nozzle (see Figure 2.2(g)). The pressure falls across an expansion wave.

When the external ambient pressure is high (at low altitude), more energy is needed to expand the gas. When more energy is provided to expand the gas the flow at the exit of the nozzle over expands, and is forced back inward by the high pressure (ambient pressure) at the exit of the nozzle. At high altitudes less energy is needed to expand the gas, as the ambient pressure and temperature are much less than at sea-level conditions. Jet aircrafts cruise at very high altitudes for this reason. Low pressure means higher speeds are achieved with minimum fuel burn.

Nozzle contours can also be designed for reasons other than for maximum thrust. Contours (shapes) can be tailored to yield certain desired pressures or pressure gradients to minimise flow separations. Military aircrafts flying above Mach 1.2 are categorised as supersonic jets. See Table 2.1 for a description of some of the jet fighters and their maximum cruise speed [2].

Table 2.1: **Jet aircrafts versus maximum Mach number.**

Aircraft type	**Mach speed (Maximum)**
F/A-18E Super Hornet (US)	Mach 1.8+ at 12,190 m
Concorde (UK)	Mach 2.05 at 60,000 ft
F-22 Rapter (US)	Mach 2.25 at 24,000m
YF-23 Black Widow II(US)	Mach 2+ at 65,000 ft
MiG-29 Super Fulcrum (Russia)	Mach 2.3 at 59,060 ft.
F-14D Tomcat (US)	Mach 2.34 at 58,000 ft
Su-30 MKI (India)	Mach 2.35+ at 11,000 m
T-50 (Russia)	Mach 2.45 at 17,000 m
F-15 Eagle (US)	Mach 2.5 at 60,000 ft
MiG-25 Foxbat (Russia)	Mach 2.8 at 118,900ft.
XB-70 Valkyrie (US) retired 1969	Mach 3.1+ at 21,000 m
MiG-25R Foxbat-B (Russia)	Mach 3.2 at 123,524 ft
SR-71A Blackbird (US)	Mach 3.2+ at 24,000 m

2.2 Exhaust Jet Plume and Shock Diamonds

Aerospace propulsion system devices operating at supersonic speeds such as supersonic jet engines, next generation hypersonic ramjet and scramjets, rocket nozzles and supersonic missiles, experience a form of repeating shock pattern known as Shock Diamonds (also known as Mach Diamonds or Mach disks) at the jet plume of the nozzle. The exhaust gas pressure (exit pressure P_e) at nozzle exit, being different from the atmospheric ambient pressure (P_a), generates Mach shock patterns. They are unknown as *Overexpanded* and *Underexpanded*.

Overexpansion of the nozzle occurs when - $P_e < P_a$ (see Figure 2.3)

Underexpansion of the nozzle occurs when - $P_e > P_a$ (see Figure 2.4)

Under the two flow conditions *Overexpanded* or *Underexpanded*, the shocks generated in both of these flow situations, some amount of thrust is lost and this reduces overall efficiency of the jet. When the exit pressure is lower than the ambient pressure the exhaust flow condition is *Overexpanded*, see Figure 2.6. When the exit pressure is higher than the ambient pressure the

Figure 2.3: Mach Diamonds during take-off of SR 71 (Flow *Overexpanded*) [1].

exhaust flow condition is *Underexpanded*, see Figure 2.4. These diamond shocks are stationary wave patterns, they can be observed at cruising altitude (see Figure 2.4) and at low atmosphere near sea-level (see Figure 2.3).

Figure 2.4: Mach Shock Diamonds formation of F-22A manoeuvring at high altitude (Flow *Underexpanded*)[4].

The Diamond shocks repeat back and forth between the opposing free jet boundaries as a process of compression and expansion of waves (see Figure 2.5 and Figure 2.6). The friction

created along the free jet boundary between the air and exhaust gas results in a turbulent shear layer. This layer creates a viscous damping effect that gradually dissipates the wave structure. This viscous friction eventually equalizes the pressure differences between the exhaust and ambient atmosphere so that the shock diamonds can no longer be formed [1]. Repeated reflections and re-reflections, will appear until the disturbances are damped out by the viscous effects.

The flow physics of *Overexpansion* and *Underexpansion* flow conditions are further addressed in Section 2.3.

2.3 Nozzle: *Overexpanded* and *Underexpanded*

With the increase of NPR a *Normal* shock (shock perpendicular to the axial direction of the flow) is generated just after the flow passes the throat of the nozzle (chocked nozzle) and will move downstream of the nozzle. Once the *Normal* shock reaches the exit of the nozzle, under the condition that the exit pressure is less than the ambient pressure (P_e<P_a), the shock tends to compress inward, or in the form of an *Oblique* shock. The ambient pressure (atmospheric pressure) causes the shock to compress inward forming a complex flow pattern, which is a combination of subsonic and supersonic flows, known as *Overexpansion*. A shock triple point is created at the point of intersection where these *Oblique* shock waves meet with the Mach disks (See Figure 2.5).

For a gas exhausted from an axisymmetric nozzle to lower pressure surroundings (P_e>P_a), *Underexpansion*, the flow will follow *Prandtle-Meyer expansion* at the exit corner of the nozzle [1]. These *Expansion* waves will be reflected from the constant pressure jet boundary as *Compression* waves. The *Compression* waves will intersect each other when the exit pressure is higher than ambient pressure. This leads to shock waves being formed in the plume as a result of coalescence of the *Compression* waves.

Downstream a snowballing compressive effect will result in an imbedded shock wave that is strong and curved. A Mach configuration of shock patterns will be formed with a Mach disk at the triple point in the intersection of the *Oblique* shock waves, known as *Underexpansion* (see Figure 2.6). This continues formation of new flow patterns are the *Compression* and *Expansion* waves repeating downstream along the plume region for both *Overexpanded* and *Underexpanded* conditions.

The formation of the shock patterns gradually tends to minimise with the increase of the

distance from the exit of the nozzle. Over time, viscous dissipation effects along the free stream jet boundary ceases the generation of further shocks along the jet boundary layer.

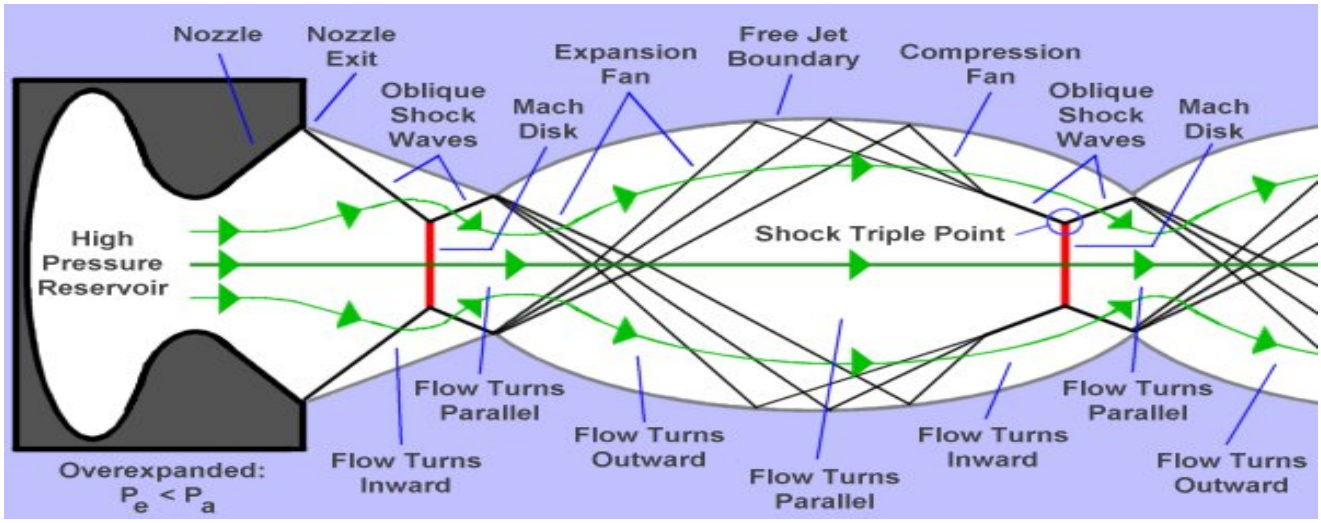

Figure 2.5: Overexpansion of the nozzle P_e<P_a [1].

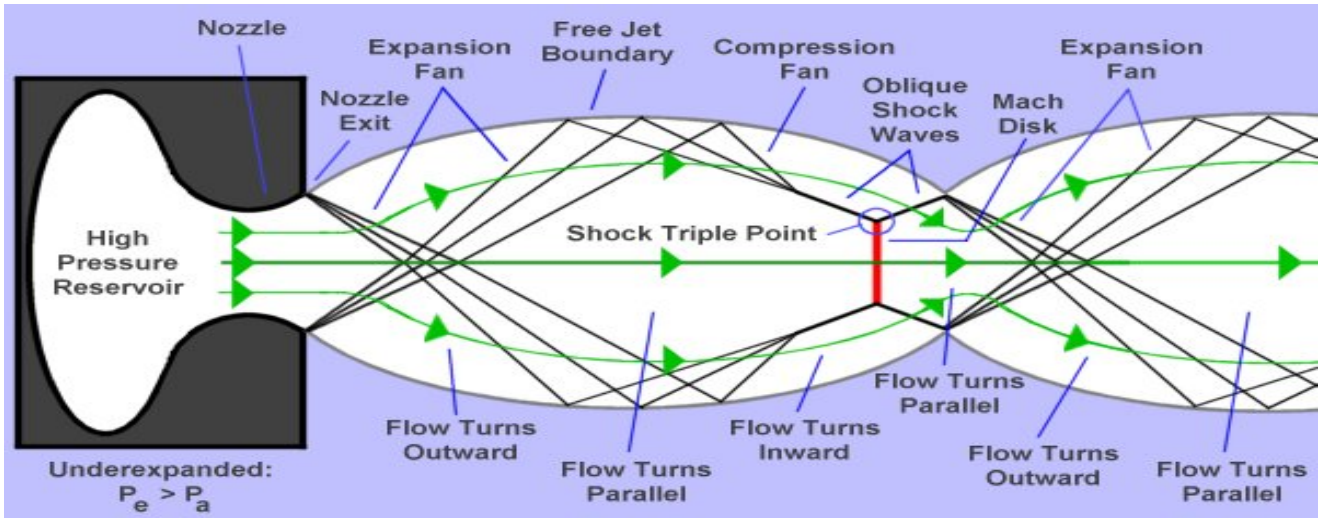

Figure 2.6: Underexpansion of the nozzle P_e>P_a [1].

It was found that *Underexpansion* and *Overexpansion* experienced by a jet nozzle at the jet plume has a significant influence on reducing the overall thrust produced by the exhaust gas. In real conditions the *Incident* shock of the Mach disk configuration is not always straight. Mach disks created due to the compression and reflection of the jet wall boundary at the jet plume has a significant effect on the overall nozzle efficiency.

The correlation between Mach disk diameter and distance to the Mach disks from the exit

of the nozzle is dominated by the geometry configuration at the divergent section of the nozzle at high NPRs.

2.4 Review of Some Recent Achievements on CD Supersonic Nozzles

Most investigations, both experimental and computational, have been conducted more for gases operating under low NPRs than of high NPRs. A summary of a literature on supersonic nozzle as follows.

Low NPRs

The compressible jet plume emerging from a planner convergent-divergent nozzle has been investigated experimentally and numerically [33] by Xiao, et al, [2009]. The numerical simulations were carried out for NAR range of 1.0 - 1.8 and NPR varying between 1.2 - 1.8. Among the several turbulence models used, the Shear Stress Turbulence (SST) model proved to be in the best agreement with the experimental results. It was found that the jet mixing was governed by NAR, and NPR to a lesser extent. As a summary of the investigation, the increasing NAR results in an increased growth rate and faster axial decay of the peak velocity. From the numerical results it was found that as NAR increased, the peak turbulent kinetic energy in the plume rose and moved towards the nozzle exit. Xiao, et al,[2009] also concluded, that the significant increase in turbulent kinetic energy inside the nozzle was associated with asymmetric flow separation. The nozzle was tested for ambient temperature (T_a) of 294 K and pressure of 14.85 psi, while the temperature of the reservoir (T_{res}) was set at $T_{res} = T_a$= 294 K. External free stream velocity was Mach 0.1 and downstream static pressure was set to ambient pressure. Reynolds number of 2.5×10^6 for a wall grid value of $Y^+<1$.

Xiao, et al, [2007] simulated compressible jet flow through a planer nozzle under the *Over-expanded* condition to observe the instability of the jet plume region [32]. Computation was carried out for a nozzle with NAR 1.0 - 1.8 for a low pressure range of NPR 1.2 - 1.8. The results show that for NPR 1.2 - 1.8, the jet mixing is governed by NAR and lesser by NPR. Xiao, et al, [2007] found that the increase in the exit-to-throat area ratio shows a significant increase of mixing rate. They also concluded that increase in TKE inside the nozzle results from the asymmetric flow separation. Further, they conclude that the asymmetric separation played an

important role in the instability of the jet plume region. In their study, the commercially available FLUENT code was used to solve the RANS equations with the two-equation turbulence model, SST. They found that the SST model exhibits the closest agreement with their experimental data. Using the SST model RANS predicted the flow field with acceptable accuracy and provided additional details that could not be obtained through experimental tests. In conclusion, the study conducted by Xiao, et al, [2007] demonstrated the significance of the numerical computation towards optimizing configurations for most effective mixing enhancements.

Xiao, et al, [2007] also solved the separation of the supersonic nozzle flow using a two equation k-ω turbulence model [31]. The NAR 1.5 was kept fixed with a divergence angle of 3.89 ^{0} and NPR was varied. Asymmetric flow separation was observed at NPR, 1.5 - 2.4. The main focus of their investigation was to study the flow structure associated with instability. They developed a code to solve the numerical equations for the convective fluxes, and the pressure term was included. The computation with a total of 41,585 grid elements was adequate enough for both internal and external bodies of the nozzle to capture instabilities. The simulation was run under steady-state mode while the nozzle was tested for ambient temperature at 290 K and pressure of 14.85 psi. Looking at the flow pattern it was observed that the *Lambda* foot shock above NPR $\geq$ 2.4 was symmetric. Unsteady movements were not able to be captured from the computational runs [31].

The investigation by Menon, N. and Skews. B.W, [2008] on low NPRs, some similar numerical and experimental research was also conducted for medium to high NPRs [21]. Effects of pressure, aspect ratio (nozzle width over height) and Mach number of an *Underexpanded* rectangular nozzle for NAR 1.5 was investigated by. The Spallart-Allmaras (1 equation) turbulence model built into the commercially available FLUENT 6 software package was used in steady-state mode. It was concluded that the non-dimensionalised Mach stem height decreases with NPR 2 and 3 as the aspect ratio of the nozzle is increased. The non-dimensionalised Mach stem height increases with increasing aspect ratios for low NPR of 2, but decreases with increasing aspect ratios for low NPRs. It was also concluded that the greater the NPR, the greater the expansion of the jet. It was observed, increasing the aspect ratio caused a greater distortion of the jet boundary. Increases to the Mach number caused the shock cell length to increase [21].

Khan A.A. and Shembharkar T.R., [2008] investigated a two-dimensional CD nozzle for low/high NPRs for corresponding shock presence inside the divergent section of the nozzle [19].

Shock location, shock structure and after-shocks were compared with the computed results. FLUENT code was used for a NAR of 1.5 with a half angle of 2.12 ^{0} and solved in steady state mode. A grid range of 5,000 - 20,000 quadrilateral elements were used, with grid elements ranging from 15,000 - 20,000 by a grid adaptation. The ambient temperature was set at 300K and total pressure 3.5×10^5N/m^2. A standard k-ϵ turbulence model with a wall function was used to solve the complex flow structure. The curvature of the pressure contours indicated that the flow was not totally uniform across the height of the nozzle due to the presence of boundary layers on the wall. The shock structure did not remain symmetric with respect to nozzle center line at higher NPR values. It was found from these experimental results that this asymmetry was attributed to the flow unsteadiness. Along the centreline region for NPR>1.20, *Normal* shocks did not sit alone but were followed by aftershocks. A summary of some of the low NPR investigations carried out on a CD nozzle in recent years is presented in Table 2.2.

Table 2.2: **Summary of some numerical investigations on Low NPR analysis in recent years**.

Year	Journal Title	NAR	NPR	Computational Setup and Details	Results/Conclusions
2009	Experimental and Numerical study of Jet Mixing from a shock-Containing Nozzle. [33]	1.0 - 1.8	1.2 - 1.8	FLUENT / SST Model 74,000 grid cells/ R_e=2.5×10^6 P_a = 14.85psi/ T_a = 294K	Jet mixing is governed by NAR and less effected by NPR. Increase in NAR peaks TKE in plume rise.
2008	Viscous Flow Analysis in a Convergent Divergent Nozzle [19]	1.5 fixed	1.20 - 2.26	FLUENT/ k-ε Model 20,000 grid cells P_{res}=50.8psi/ T_a=300K	After shocks stronger at high NPRs. Flow de-acceleration through shocks and re-expands to high speeds.
2008	Rectangular underexpanded gas effects: effect of pressure ratio, aspect ratio and Mach number.[21]	1.5 Fixed	2.0 - 3.0	Spallart-Allmaras Model FLUENT 6	Experimental and numerical analysis on effects of nozzle aspect nozzle aspect ratio, pressure and Mach number.
2007	Numerical Study of Jet Plume Instability from an Overexpanded Nozzle. [32]	1.0 - 1.8	1.2 - 1.8	FLUENT / SA, k-ω, k-ε, SST RSM Model/ 74,000 grid cells P_a = 14.85psi/ T_a = 530R	Increase in NAR peak the TKE in the plume rises and moves towards the nozzle exit.
2007	Numerical Investigation of Supersonic Nozzle flow separation. [31]	1.5 fixed	1.27 - 1.61	In house Code/ k-ω Model 41,585 grid cells/R_e=5.5×10^6 P_a=14.85psi/ T_a=290K	Higher values of NPR symmetric shocks is formed. Shear layer separation is a main factor for instability.

Medium to High NPRs

Matsuo, et al, [2008] studied the influence of nozzle geometry on a highly *Underexpanded* sonic jet [25]. Their investigation proved that the distance from the nozzle exit to the Mach disk

is an increasing function of the jet-pressure ratio and also influenced by the nozzle geometry. However, the effect is not significant when the effective diameter concept is considered. They also found that pressure ratio was a key parameter in determining the jet boundary, as increasing pressure expands the jet boundary. They concluded that the location of the Mach disk is a linear function of the peak value of the local angle of the jet boundary at near-field. During their investigation, NPR was varied from 4.0 - 12.0. The nozzle was simulated at ground level conditions. The tests were carried out for three nozzle cases, one cylindrical straight nozzle with a curvature at the entrance, and two nozzles with a sharp edge with orifice convergence angle of 75 ^{0} and 90 ^{0} respectively [25].

The investigation by Menon, N. and Skews, B.W, [2009] on high NPRs, a numerical study has been undertaken on *Underexpanded* sonic jets issuing from nozzles of varied inlet geometries [22]. The numerical simulation of the *Underexpanded* jet impingement flow was carried out using the commercially available code Fluent 6. The flow was modeled as a viscous flow, with the one equation Spallart-Allmaras turbulence model for closure of the Reynolds Averaged Navier-Stokes equations. Is was concluded during the investigation, the Mach stem height in the jet issuing from the contoured nozzle has been the greatest over the range of pressure ratios varying from 2.0 - 10.0 is investigated. The curvature of the Mach stem in the direction of the flow and the curvature is more pronounced as the pressure ratio is increased. Further, the formation of a vena-contracta resulting in a narrowing in the jet boundary is observed in the case of the 45 degrees and the orifice inlet nozzles.

Yuceil, K. B. and Otugen M.V., [2002] carried out an experimental study of investigating the spreading and centerline property decay rates of *Underexpanded* supersonic jets [35]. Five different *Underexpanded* sonic jets were studied with jet exit-to-ambient pressure ratios of 1, 2.5, 7.5, 15.5, and 20.3, corresponding to fully expanded jet Mach numbers at 1, 1.68, 2.38, 2.85, and 3.03, respectively. The scaling analysis presented in this report lead to a set of parameters that can be used to obtain universal asymptotic values for jet growth and centerline property decay rates. It provides the initial diameter, velocity, density and temperature of an expanded equivalent jet whose static pressure is that of the ambient. Further, the experimental results show that, in the farfield, the asymptotic decay rate of the centerline velocity is a strong function of the *Underexpansion* ratio, decreasing with increasing velocity.

Mohamed, A. and Hamed, A., [2003] used a CD nozzle in the experimental study has an exit to throat area ratio (NAR) of 2.79 for a design Mach number, M_d of 2.5 and a design

pressure ratio, NPR_d, of 19.4 [24]. The rectangular cross section is 25.4 mm x 4.92 mm at the exit plane for an aspect ratio (AR) of 5.1. Tests were performed over a range of nozzle pressure ratios, NPR, between 4.0 - 9.0. The change in NPR was achieved by changing the inlet stagnation pressure to operate in the external *Overexpanded* regime. The increase rate of the shock cell length was dependant on the nozzle design Mach number, and on the shape of the jet cross section. They concluded, the dissipation rate was higher for elliptic and highest for rectangular jets, compared to circular jets of the same equivalent diameter.

Wlezien, R. W. and Kibens, V., [1988] investigated non-axis-symmetric nozzles are constant-diameter tubes with various cutout exit shapes. Variation to the nozzle geometry by introduction of azimuthal asymmetry, a technique for controlling development of high-speed jets [30]. NPR tested for 2.2, 2.8, 3.4 and 4.0 for a divergent angles up to 30^0 for three nozzle shapes (1-tab nozzles, inclined nozzles and 2-tab nozzles). Applications of this technique include thrust vectoring, mixing enhancement, and noise reduction. The investigation has touched upon only a few aspects of flows from non-axisymmetric nozzles. It was concluded, that many parameters govern the flow and noise fields and that relatively small changes in geometry or flow conditions can produce large, seemingly unpredictable variations in thrust, mixing, and noise. Supersonic jets from non-axisymmetric nozzles exhibit a wider range of acoustic and flow properties than does an axis-symmetric reference nozzles. Further, the mean flow-properties such as deflection and divergence can be controlled to provide directional thrust.

The investigation carried by Menon, N. and Skews, B.W., [2009] describes the experimental studies performed by Teshima, K., [1994] on a rectangular nozzle with aspect ratios 2, 3, 4, 5 and 64 for *Underexpanded* condition tested for NPRs up to 500 [29]. A summary of some of the high NPR investigations carried out on CD supersonic nozzles is presented in Table 2.3.

Evidence from the previous experiments also proves that a non-circular nozzle shape expands the gas faster, hence have higher exhaust velocity speeds than of a circularly contoured nozzle shape [21], [5], [24].

Considering all aspects discussed above, this study is focused on investigating a two dimensional convergent divergent nozzle with a rectangular cross-section (unit length width), axis-symmetric and asymmetric nozzle shapes under both low NPR (1.27 - 4.0) and high NPRs (4.0 - 12.0) conditions.

Table 2.3: **Summary of some numerical investigations on High NPR analysis in recent years**.

Year	Paper title	NAR	NPR	Computational setup and Details	Results/Conclusions
2008	Influence of nozzle geometry on the near-field structure of highly Underexpanded sonic jet [25].	convergence angle 75^0 and 90^0	4.0 - 12.0	In house code, Modified k-R model	Distance from the nozzle exit to the Mach disk is an increasing function of jet-pressure ratio and nozzle geometry.
2009	Effect of nozzle inlet geometry on Underexpanded supersonic jet characteristics [22].	AR 1 - 4 Rectangular nozzle	2.0 - 10.0	Spallart-Allmaras model, Fluent 6	Curvature of the Mach stem pronounced as the pressure as ratio is increased.
2002	Scaling parameters for underexpanded supersonic jets [35]	Nozzle exit diameter 4.45 mm	1.0 - 20.3	Experimental analysis	The asymptotic decay rate of the centerline velocity strong function of the *Underexpansion* ratio.
2003	Supersonic Rectangular Over-Expanded Jets of Single and Two-Phase Flows [24].	AR = 5.5 and throat NAR 2.79	19.4	Experimental analysis	Dissipation rate was higher for rectangular jets compared to circular jets.
1988	Influence of Nozzle Asymmetry on Supersonic Jets [30].	Divergence angle 30^0	2.2 - 4.0	Experimental analysis	Flowfield characteristics and screech instabilities in supersonic jets.
1994	Structure of supersonic free jets issuing from a rectangular orifice [29].	AR of 1,2,3, 5 and 64	500	- -	Rectangular jets under *Underexpanded* condition for high NPRs.

2.5 Turbulence

Turbulence is not a feature of fluids but of fluid flows and consists of many characteristics which may vary depending on the environment. Turbulence flow is three dimensional, chaotic, stochastic and random, hence behavior of turbulence could not be precisely defined nor predicted. Turbulence causes the formation of eddies of many different length scales. Kinetic energy of the turbulent motion is contained in the large scale structures and this energy cascades from large scale structures to smaller scale structures by an inertial and essentially inviscid mechanism. This process continues, creating smaller and smaller structures that produce a hierarchy of eddies. Eventually this process creates structures that are small enough that molecular diffusion becomes important and viscous dissipation of energy finally takes place.

The flows which is originally been laminar, and develops to turbulent with the arises of the instabilities at high Reynolds numbers of a turbulent jet flow is shown in Figure 2.7.

Turbulence does not maintain itself, but depends on its environment to obtain energy. The common source of energy for turbulent fluctuations is shear in the mean flow. Turbulence occurs when the inertia forces in the fluid become significant compared to viscous forces, and

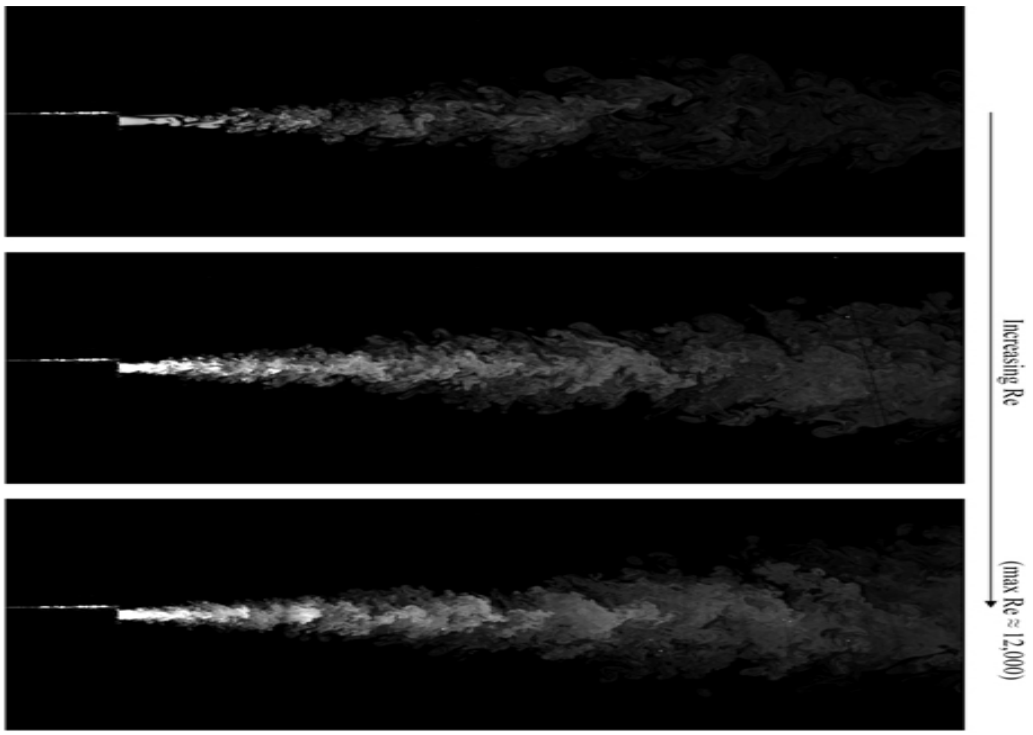

Figure 2.7: Turbulent jet flow [17].

is characterised by a high Reynolds Number [17].

However, with the development of advance mathematical codes, super computers and new generation high-speed wind tunnel testing facilities, a number of turbulence models have been developed to simulate the turbulence phenomenon under various conditions successfully, provided further understanding of the chaotic behaviour.

2.6 Turbulence Models in ANSYS CFX

Single equation turbulence model will not satisfy all scales to be analysed in turbulence. For this reason a number of turbulence models built from zero to a few equations combined depending on the applications. Several algebraic models, including Spalart-Allmaras Model, k-ε model, k-ω model and Shear Stress Model (SST) model are RANS based linear eddy models is used in CFD software, ANSYS CFX which is described in Section 3.3. Each turbulence model has its own strengths and weaknesses.

2.6.1 k-ε Model

The k-ε model is a two equation model where k is turbulent kinetic energy that determines the energy of the turbulence. The ε is turbulence dissipation rate that determines the scales of the turbulence. The k-ε model is a first order closure model. The k-ε model is promisingly accurate for free-shear layer flows with relatively small pressure gradients and for wall-bounded and internal flows where mean pressure gradients are very small. This model fails to model flows containing large adverse pressure gradients. The standard k-ε model is used in most cases because of its robustness, economy and reasonable accuracy for a range of flows, but it fails to predict for non-equilibrium boundary layers. The k-ε model tends to predict onset separation too late and under predicts the separation size. Thus, the model is not very accurate for devices such as diffusers, nozzles, turbine blades and aerodynamics bodies.

2.6.2 k-ω Model

The model includes two transport equations representing turbulence properties to take into account the history effects such as convection and diffusion of turbulent energy. The k-ω model is a first order closure model. The first transport variable k is turbulent kinetic energy and the second variable ω is the specific dissipation rate characterising the turbulent behavior. The k-ω model model is very accurate capturing flow characteristics at boundary layers but weak for 3D modelling and has no advantage for calculating Reynolds stress. Therefore, less cost effective in 3D flow modelling.

2.6.3 SST Turbulence Model

The Shear Stress Transport (SST) Model (Menter, 1993) [23] is currently a popular turbulence model for compressible viscous flow analysis for high Reynolds numbers internal and external flows. Many practical flows occur at conditions where compressibility effects are important. For flows under adverse pressure gradients, a turbulence model to capture boundary layer separation is important. The boundary layer separation occurs at small scales, and capture regimes with large and small scales such as separation zones and shocks, an accurate and favorable turbulence model is required. Additionally a model should be able to predict either surface heat fluxes or shear stress to obtain accurate modeling of separation flows.

Among the k-ε and k-ω models, SST is a mixture of k-ε and k-ω models. The model

is being popular for supersonic and beyond flow regimes. Stress transport models use the Reynolds stress equations to provide the turbulent stresses in the mean-momentum equations. The SST model is a first order closure model. It uses formulation of the k-ω equation model for the inner part of the boundary layer, and gives the model the ability to directly reach the wall through the viscous sub-layer while switching to the k-ε formulation to model the free-stream flow. This blending of the formulations gives the smooth transition that stands out from other turbulence models used for problems associated with high Reynolds numbers.

A turbulent viscosity limiter, an additional smooth blending function F_{sst}, within the range of $1>F_{sst}>0$, is used in the SST model [20]. When the model is used for flow simulation with boundary layer separation zones, the limiter F_{sst} switches to 0 for wake and free shear regions and 1 for bulk region creating a smooth transition between the regions. The F_{sst} is modified in the term $\upsilon = a_1 k/\Omega$, of Bradshaw's turbulent viscosity in the BSL model, resulting in the limited turbulent viscosity formulation $\upsilon = a_1 k/\max(a_1\omega, \Omega F_{sst})$, in the Mentor's SST model [20]. The a_1 is known as the Bradshaw constant, Ω in here is mean flow vorticity magnitude, k is turbulent kinetic energy, υ is kinematic turbulent viscosity and ω is specific turbulence dissipation rate [20].

The SST model was initiated with accompanying shear stress and is proportional to turbulent kinetic energy in the wake of the boundary layer, which is suited for accurately capturing flows subjected to adverse pressure gradients. The additional correction function F_{sst} embedded in the equation provides for greater accuracy compared to other turbulence models testing for flows under strong pressure gradients.

Table 2.4 gives a summary of the turbulence models used in ANSYS CFX.

2.7 Boundary Layer Separation

The study of flow separation from the surface of a solid body and the determination of surrounding changes in the flow field that develop as a result of the separation are among the most fundamental and difficult problems of fluid dynamics. When a stationary object (like the nozzle) is subject to moving fluid or an object is moving through a stationary fluid (such as the aerofoil), a boundary layer of the fluid is created around the solid object. The boundary layer could be either laminar or turbulent based on the local Reynolds number.

Within this boundary layer, viscous forces (frictional forces between the solid and fluid)

Table 2.4: **Turbulence models**.

RANS Eqn Level	**Category**	**Turbulence models**
First order closure	zero - equation model	Algebraic model
First order closure	one - equation model	Spalart-Allmaras Model
First order closure	two - equation model	k-ε Model k-ω model SST (Shear Stress Transport Model)
Second order closure	- -	RST (Reynolds Stress Transport Model) ARS (Algebraic Reynolds Stress Model)
RANS based	non-linear	LES (Large Eddy Simulation)

develop in the fluid layer next to the solid surface. Flow separation along the solid surface occurs when the boundary layer moves downstream against the adverse pressure gradient until the speed of the flow in the fluid layer next to the solid surface decreases to zero or reverses back (negative velocity), as illustrated in Figure 2.8.

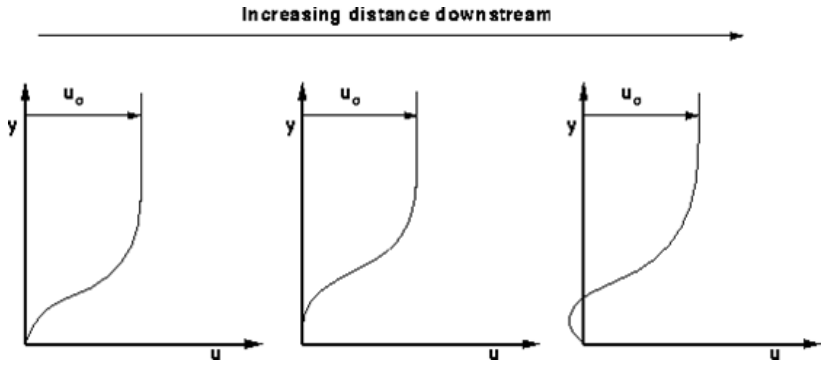

Figure 2.8: Reverse flow due to adverse pressure gradient [6].

The negative velocity makes the flow close to the surface reverse, which increases drag and reduces the flow velocity. The flow becomes detached from the surface, and vortices and eddies develop and generate turbulence.

As a result of the boundary layer separation, the thickness of the boundary layer increases dramatically with influence of the negative velocity gradient causing the fluid layer next to the surface to reverse back, see Figure 2.8.

This separation of the boundary layer increases the drag. The increase in the fluid pressure in the direction of the flow is known as the adverse pressure gradient. This increase in pressure hence increases the potential energy of the fluid while decreasing the kinetic energy that results

in decrease of the flow acceleration.

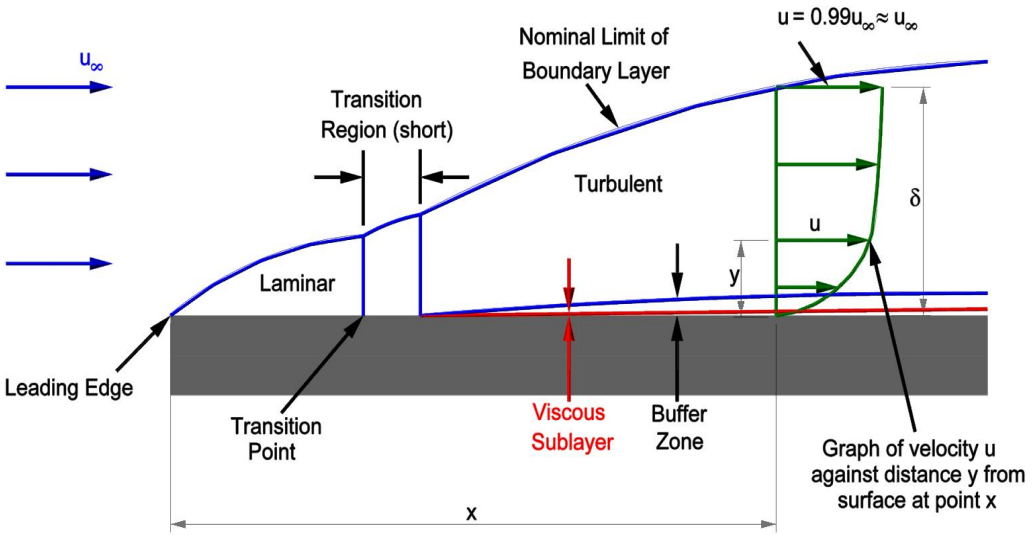

Figure 2.9: Laminar to turbulent boundary layer separation [15].

When this phenomenon occurs, the boundary layer thickness (δ - distance required for the velocity profile to reach the free stream value, see Figure 2.9) increases accordingly. The boundary layer thickness for turbulent flow is given as $\delta \sim \mathrm{x/R_e}^{-1/5}$.

When the boundary layer thickens it reduces the velocity gradient ($\mathrm{d}x/\mathrm{d}t$) concomitantly decreasing the shear wall stress. As the pressure gradient increases the wall shear stress could reach zero causing the flow to separate. At large adverse pressure gradients, separation is bound to occur.

Figure 2.10 illustrates the phenomenon of boundary layer separation and development of *Reflection* and *Incident* shock over a flat plate is shown in [12]. The increase of the adverse pressure gradient is influenced by the increase of the fluid speed along the boundary layer. As a result of the detachment of the boundary layer and the flow separation, the *Compression* waves are followed by *Incident* and *Reflection* waves and *Expansion* fans are generated. The situation is slightly different when the flow separation occurs in an internal flow (nozzle flows / pipe flows), but the principle behind the generation of the *Incident* and *Reflection* shock waves is the same.

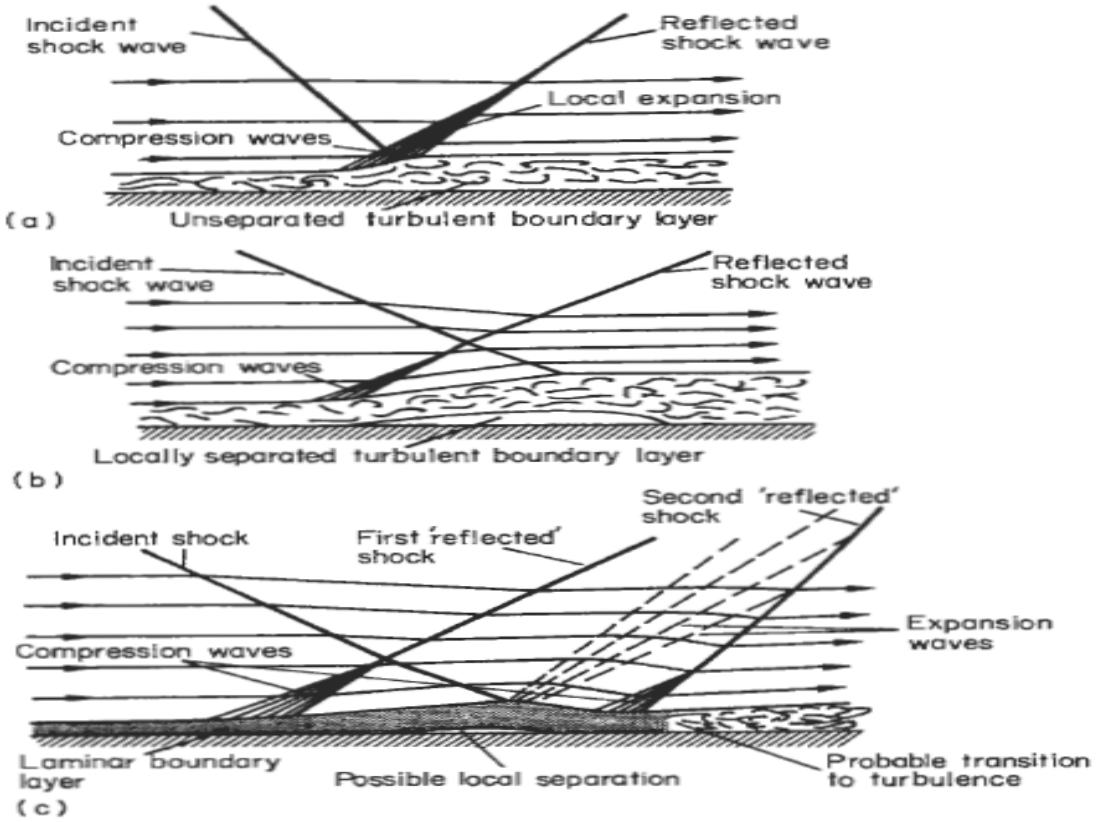

Figure 2.10: Boundary layer separation over a flat plate [12].

2.8 Boundary Layer and Nozzle Flow Separation

Flow separation at the divergent section of the nozzle is one of the many phenomena that occur in internal flows subjected to supersonic flow. When the shock wave interacts with the boundary layer, many diverse types of flow phenomena occur such as flow separation, unsteadiness, vortical flow, pressure waves, complicated mixing and turbulence [12]. The boundary layer separation is due to the shear of the inner layer between the flow and the nozzle wall: the detachment creates instability followed by many weak shocks, which decelerate the exhausting gas. The increasing adverse pressure gradient of the *Incident* shock causes the boundary layer to separate from the nozzle wall as a shear layer. The region bounding the shear layer and the nozzle wall is called the separation zone and is also known as the circulation zone [12], [14], [15] (see Figure 2.11).

Instability initiated by Shock Wave Boundary Layer Interaction (SWBLI), at the divergent section of a supersonic CD nozzle causes the exhaust gas to lose the build up fluid kinetic energy, hence decelerate flow speed, and decreasing the overall thrust. For internal flow, the effects of SWBLI are total pressure loss and unsteadiness, and loss of flow control performance

is key disadvantage. At higher Reynolds numbers, the small disturbances generated at the

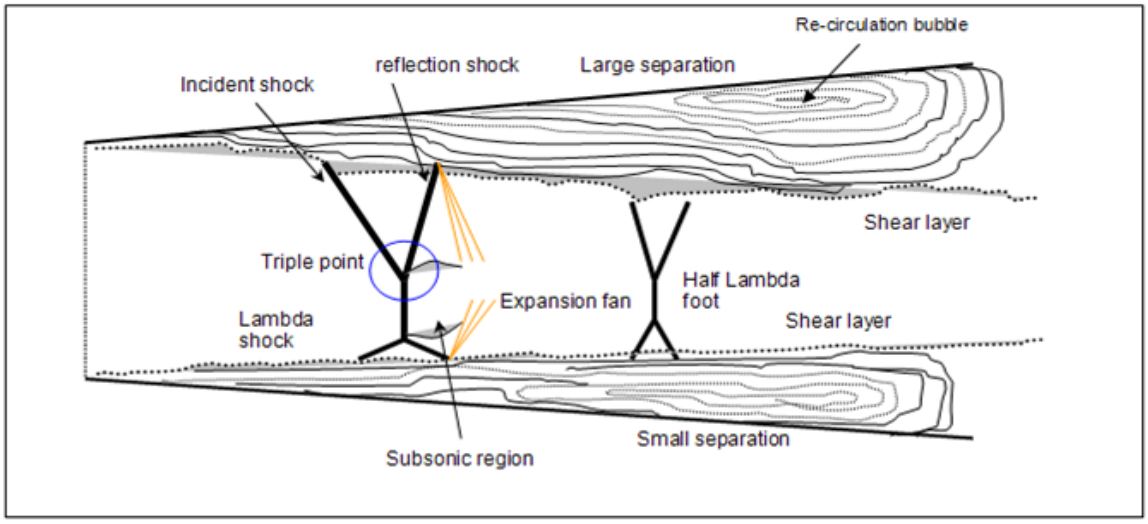

Figure 2.11: *Lambda* foot shock wave and circulation-bubble [14].

tip of sudden expansion amplify in the shear layers formed between the main flow and the re-circulation flow at the corners [26]. The results in shedding of eddy like patterns which alternate from one side to other with consequent asymmetry of mean flow. Although the flow was three-dimensional, its major features could be understood by considering the interaction of two dimensional shear layers [26].

Due to this instability a bifurcated structure as shown in Figure 2.12 created between the two flow separation zones [27]. The *Resultant* shock is created from an *Incident* shock that merges from the starting point of the top wall separation zone and is met at a common point called the triple point, where the *Reflection* shock and the vertical *Lambda* shock meet. The *Reflection* shock bounces back from the shear layer as an *Expansion fan* that bounces back again by reflecting from the opposite circulation zone (see Figure 2.12) as a *Compression wave* [12]. This pattern will move downstream repeating itself. The wavy slip streams that emerge from the triple point creates a zone of a convergent-divergent fluidic channel that generates a subsonic region. The triangle shape is called the *Lambda* foot, and the size of this *Lambda* foot shock becomes half the size down stream (see Figure 2.11) and eventually diminishes away between the exit and the plume region [15].

When the NPR is increased the *Lambda* foot shock moves away from the throat and the separation zone transforms from asymmetric to symmetric 2.12). The circulation zone flips between asymmetry to symmetry between the opposite walls and gradually diminishes away

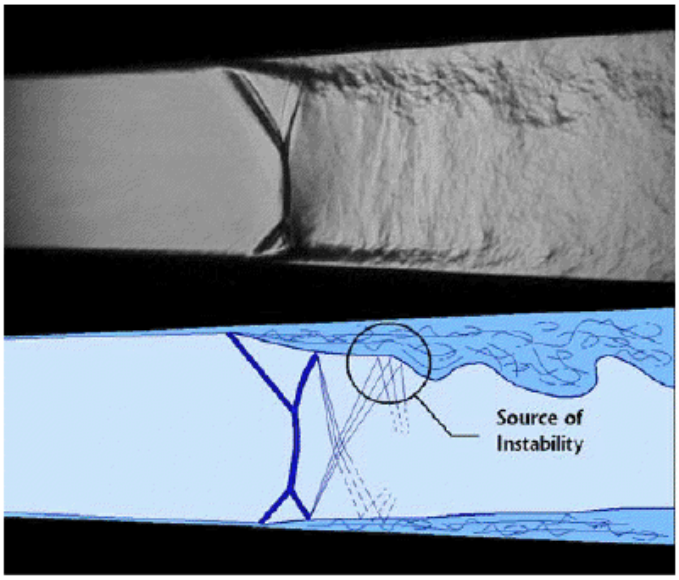

Figure 2.12: Flow separation and Shear layer instability seen through a spark schlieren [27].

at the exit of the nozzle.

For external flow, Shock Induced Boundary Layer (SIBL) separation can results in increased aerodynamic drag, loss of lift, aerodynamic heating, and increased instabilities such as inlet buzz and buffeting.

2.9 Summary of the Reviews and Concluding Remarks

Reviews from the previous literature on computational and experiments results, following conclusions were highlighted as the key areas of interest towards this study.

1. Supersonic jet and plume flow condition through a CD nozzle need further investigation on the asymmetric configurations of the nozzle.

2. The direction of interest on axis-symmetric nozzle configurations, initiates the importance of the flow phenomena including *Underexpanded*, *Overexpanded* flow conditions, nozzle internal shocks (*Lambda*, *Incident* and *Reflection* shocks) and Shock induced boundary layer separations associated to supersonic flow. The above mentioned flow phenomena and its influence on an asymmetric nozzle shape.

3. Most previous investigations was conducted on axis-symmetric nozzles where the flow characteristics are associated with low NPRs. Hence, as a key areas of interest on this study, the flow characteristics associated with high NPRs for a asymmetric nozzle shapes and the significance of the down stream flow characteristics at the jet plume region is noted.

Chapter 3

Modelling Descriptions

3.1 Governing Equations of Fluid Flow

To understand the physics of the fluid in motion related to any engineering problem, its important that we develop a accurate relationship among the variations of the fluid flow properties such pressure, temperature, velocity, density etc at discrete points in space and time. The fluid governing equations proves a theoretical solution to how these flow properties are related to each other by either integral, differential or algebraic equations. The following three fundamental laws known as the conservation laws are used to establish the governing equations of the fluid flow.

- **Conservation of Mass**

  rate of change of mass + net outward mass flux = 0

- **Conservation of Momentum**

  rate of change of momentum + net outward momentum flux = sum of forces

- **Conservation of Energy**

  rate of work of forces + net heat flux = change in total energy

The corresponding governing equations are continuity equation, momentum equation and energy equation.

3.1.1 Mass is conserved (Law of Mass Conservation)

Mass cannot be created in a fluid system, nor can it disappear. A conserved quantity cannot increase or decrease, it can only move from place to place.

Using this conservation principle with the Gauss's divergence theorem, applied for a control volume in integral form, can be simplified in the following equation [18], which is valid for all flows compressible or incompressible, viscous or invisid,

$$\frac{\partial}{\partial t}\oint_{\Omega}\rho d\Omega + \oint_{\Omega}\nabla \bullet (\rho \mathbf{V})\, d\Omega = 0. \tag{3.1}$$

where ρ is density and Ω is control volume. The term $\nabla\bullet$ represents the divergence of the vector $\mathbf{V}$. The fluid velocity is $\mathbf{V} = u\boldsymbol{i}+v\boldsymbol{j}+w\boldsymbol{k}$ where u, v, and w are the velocity components in $\boldsymbol{i}$, $\boldsymbol{j}$ and $\boldsymbol{k}$ directions. Based on above law, the conservation of mass for compressible flow can be presented in differential conservation form [18],

$$\frac{\partial \rho}{\partial t} + \frac{\partial(\rho u)}{\partial x} + \frac{\partial(\rho v)}{\partial y} + \frac{\partial(\rho w)}{\partial z} = 0. \tag{3.2}$$

The above partial differential equation (3.2) in divergence form gives [8],

$$\frac{\partial \rho}{\partial t} + \nabla \bullet (\rho \Omega) = 0. \tag{3.3}$$

3.1.2 Momentum is conserved (Newton's Second Law)

Newton's second law is applied to a control volume or element to derive the momentum equation. Variations of momentum are caused by the net force acting on a control volume. This principle is applied to the control volume Ω using two distinct classes of forces, (1) body forces (external forces) and (2) surface forces which incorporate pressure forces and viscous forces. These types of fluid forces, are embedded into the momentum equations. The surface forces that act on the faces of the control-volume are proportional to the volume surface area, and are (a) pressure forces and (b) viscous forces. The frictional forces arise from relative motion of the fluid. For inviscid flow the only surface force is the pressure force [8].

Based on the Newton's second law, using divergence notation the integral form for momentum x direction [12]:

$$\oint_{\Omega}\frac{\partial(\rho u)}{\partial t}d\Omega - \oint_{\Omega}\nabla \bullet (\rho u \boldsymbol{V})\, d\Omega = \oint_{\Omega}\rho \boldsymbol{F}_x d\Omega - \oint_{\Omega}\frac{\partial p}{\partial x}d\Omega \tag{3.4}$$

where p is pressure, $\mathbf{F}_x$, $\mathbf{F}_y$ and $\mathbf{F}_z$ are additional surface forces, which are the shear and normal viscous stresses in x, y and z directions integrated over the control volumes.

The momentum equation in differential form along the x direction:

$$\frac{\partial(\rho u)}{\partial t} + \frac{\partial(\rho u u)}{\partial x} + \frac{\partial(\rho v u)}{\partial z} + \frac{\partial(\rho w u)}{\partial z} = -\frac{\partial p}{\partial x} + \rho F_x.$$

The u, v, and w are the velocity components in x, y and z directions.

The above equations could also be written using the divergence theorem in x direction,

$$\frac{\partial(\rho u)}{\partial t} + \nabla \bullet (\rho u \mathbf{V}) = -\frac{\partial p}{\partial x} + \rho F_x. \tag{3.5}$$

Similarly, we have the following equations describing the y and z momentums:

$$\frac{\partial(\rho v)}{\partial t} + \nabla \bullet (\rho v \mathbf{V}) = -\frac{\partial p}{\partial y} + \rho F_y, \tag{3.6}$$

$$\frac{\partial(\rho w)}{\partial t} + \nabla \bullet (\rho w \mathbf{V}) = -\frac{\partial p}{\partial z} + \rho F_z \tag{3.7}$$

3.1.3 Energy is conserved (First Law of Thermodynamics)

The first law of thermodynamics is applied to derive the energy equation. The law states that any changes in time of the total energy inside the volume are caused by the rate of work of forces acting on the volume and by the net heat flux into it.

Based on the above law the following equation is given in integral form [12]:

$$\oint_\Omega \dot{q}\rho d\Omega - \oint_\Omega \nabla\bullet(p\,\boldsymbol{V})\,d\Omega + \oint_\Omega \rho(\boldsymbol{f}\bullet\boldsymbol{V})\,d\Omega = \oint_\Omega \frac{\partial}{\partial t}[\rho(e+\frac{V^2}{2})]\,d\Omega + \oint_\Omega \nabla\bullet[\rho(e+\frac{V^2}{2})\,\boldsymbol{V}]\,d\Omega \tag{3.8}$$

using the divergence theorem, the energy equation in differential conservation form:

$$\frac{\partial[\rho(e+\frac{V^2}{2})]}{\partial t} + \nabla \bullet [\rho(e+\frac{V^2}{2})\mathbf{V}] = -\nabla \bullet (p\mathbf{V}) + \rho\dot{q} + \rho(\boldsymbol{f}\bullet\mathbf{V}) \tag{3.9}$$

where e is internal energy (per unit mass), and $\dot{q}$ is the rate of heat added. The term $(e+\frac{V^2}{2})$ is the sum of internal and kinetic energies per unit mass.

3.2 Turbulence Modelling

Turbulence as described in Chapter 2, consists of velocity fluctuations in all directions and has an infinite number of scales. To accurately accommodate this turbulent disturbance in the fluid motion, we have to interpret the transient velocity distribution as a instantaneous velocity distribution property. Considering infinitesimally small elements (expressed in differential form) we could specify instantaneous variables (specifying turbulence) in terms of mean velocity - U_i and fluctuating velocity - u_i(t) value as shown in Figure 3.1. The behavior of the instantaneous velocity can be expressed in two variable notations. The decomposition of variables, the mean and fluctuating values is known as the Reynolds averaging [34]. One reason

the decomposition of the variables is used is to measure flow quantities as we are interested in the mean values rather than the time histories. Another reason is that we require numerical results for a fine grid to solve all turbulent scales and this requires fine resolution of time hence turbulence is always unsteady.

The governing equations are then solved for the mean value U_i, (see Figure 3.1). Likewise, we can characterize the flow variables in mean (U_i, V_i, W_i, P_i, T_i, etc) and fluctuating ($u_i(t)$, $v_i(t)$, $w_i(t)$, $p_i(t)$, $t_i(t)$, etc) properties.

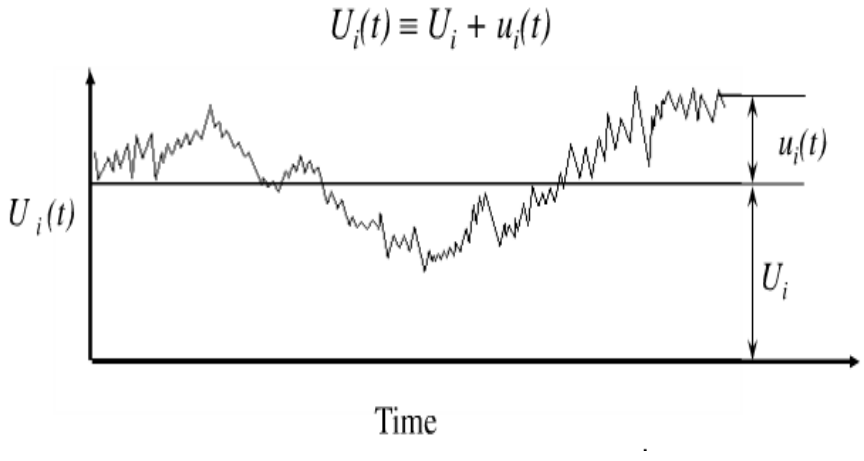

Figure 3.1: Turbulence mean and fluctuating parts [34].

3.3 Discretization of the Governing Equations in ANSYS CFX

The fundamental laws used to establish the fluid governing equations, the continuity equation, the momentum equation and the energy equation, are also the principle equations used in computational fluid dynamics (CFD). The Reynolds averaging adds unknown terms containing products of fluctuating terms (viscous stresses, which are known as Reynolds stresses) to the equations. These unknown Reynolds stresses need to be modeled with known equations to achieve closure to the equations. To obtain solutions for real flow situations, a numerical approach must be adopted. The RANS equations are replaced by algebraic approximations that can be solved using a numerical method [9].

The CFD software, ANSYS CFX first involves discretizing the spatial domain using a mesh. The mesh is used to construct finite volumes, which are used to conserve relevant quantities

such as mass, momentum, and energy. The mesh is three dimensional and all solution variables and fluid properties are stored at the nodes (mesh vertices). These conservation equations are integrated over each control volume, and Gauss Divergence theorem is applied to convert volume integrals involving divergence and gradient operators to surface integrals [9].

Many discrete approximations developed for CFD are based on series expansion approximations of continuous functions (such as the Taylor series). The order accuracy of the approximation is determined by the exponent on the mesh spacing or time step factor of the largest term in the truncated part of the series expansion, which is the first term excluded from the approximation. ANSYS CFX uses second order accurate approximations and finite-element shape functions to perform these approximations, where the tri-linear shape functions describe the variation of a variable within an element [9] such as hexahedral, tetrahedral, wedge, and pyramid.

3.4 Near wall treatment and Y^+ value

Near a solid surface where shear stresses are significant, the inviscid flow assumption is not valid. The molecules of the flow just above the surface are slowed down due to the fluid layer in contact with the solid boundary. The further fluid moves away from the solid surface, the fewer the collisions of fluid molecules with the object surface. This creates a thin layer of fluid near the surface in which the velocity changes from zero at the surface to the free stream value at a certain distance away from the surface. For viscous internal flow bonded by solid boundaries, specially subjected to adverse pressure gradients, the developing physical boundary layer grows in thickness. Therefore, a technique to accommodate the crucial changers in properties of fluid near the vicinity of the solid walls is important.

In CFD, local refinement of grid near solid boundaries is commonly used to investigate flow separations. The local refinement adequately allocates additional grid points near the wall, to catch the critical changes within the boundary layer [34].

$$y^+ = (\rho u^* y)/\mu. \tag{3.10}$$

According to the boundary layer theory, y^+ (shown in Equation 3.10) value is the non-dimensional distance. where ρ is density, u^* is friction velocity, y is distance from wall and μ is dynamic viscosity. Referring to Figure 3.2, when the mesh is fine enough to resolve the

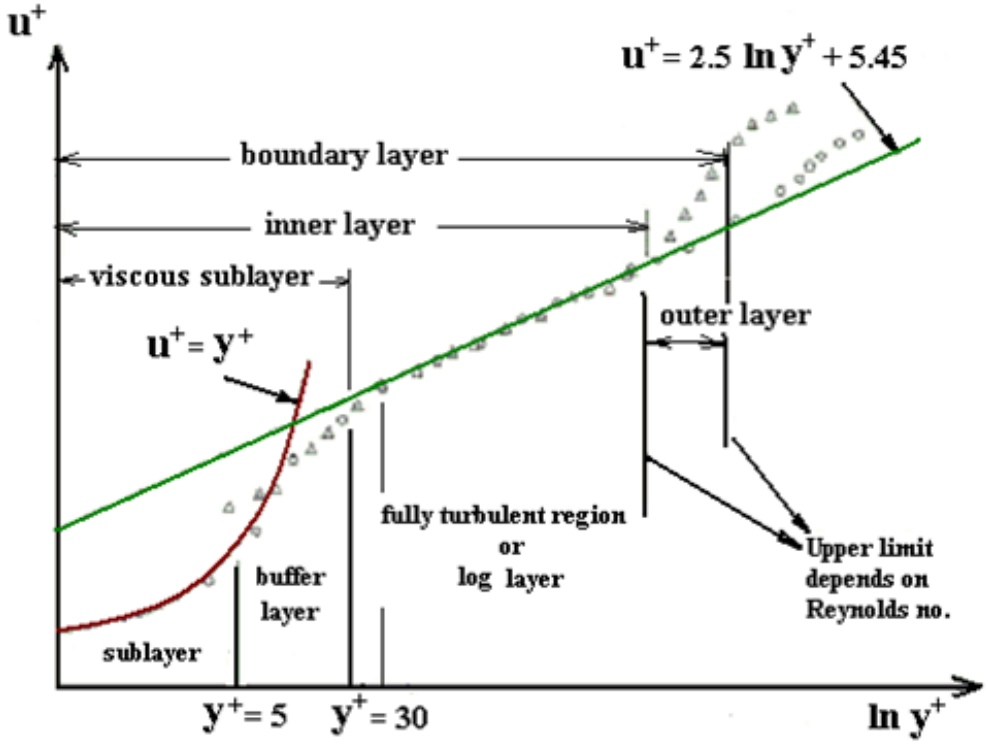

Figure 3.2: Experimental data and the wall laws [34].

laminar sublayer, the laminate stress-strain relationship can be used to derive the wall shear stress:

$$u^+ = y^+ \tag{3.11}$$

We define $u^+ = u/u^*$, where u is the velocity parallel to the wall. In terms of CFD, y value is the distance from the wall to the centroid of the first grid cell and is derived from y^+ of the equation (3.11).

This will decide how course or fine the mesh and plays and important part in turbulence modeling when determining the size of the cells near the walls. If the mesh is too coarse to resolve the laminar sub-layer and the centroid of the first grid cell adjacent to the wall is within the logarithmic, then the wall shear is obtained using log law relationship gives:

$$u^+ = 2.5\ lny^+ + 5.45 \tag{3.12}$$

Different wall models require different y values for the centroid of the wall adjacent grid cell. The turbulence model wall laws have restrictions on the y^+ value at the wall. A faster flow near the wall will produce higher values of y^+, hence the grid size near the wall must be

reduced.

For a fully resolved boundary layers subjected to adverse pressure gradients (separation regions) in SST turbulence model, the $y^+ < 2$ provides a good approximation of capturing the flow characteristics within the bounded region [10].

Chapter 4

Computational Model Settings

The symmetric and asymmetric nozzle geometries described in Chapter 2 is simulated using the CFD simulation software, ANSYS CFX 12. The model geometries were set in CFX - Design Modeler platform, is meshed (Discretization) in CFX - Mesh and solved using CFX - Solver.

4.1 Nozzle Geometries and Computational Setup

4.1.1 Nozzle Geometries

The axis-symmetric base model of this study, NAR 1.5 is based on dimensions described in study conducted by [28],[31],[33], with a divergent length (down stream) of 117 mm and a throat height of 22.9 mm. The convergent length is set to 150 mm. The Model 1a (NAR 1.5) as described in Chapter 2 with above mentioned dimensions is used as the base model, with a divergent angle of 2.801 degrees as shown in Figure 4.1 (1a). Using the dimensions of the base model Model 1a (NAR 1.5) as consistent lengths on all models, the NAR is varied. To analyse the design at a conceptual level, geometry of the divergent section of the base model NAR 1.5 nozzle is subjected to three approaches, and is illustrated in Figure 4.1.

(1a) Symmetric type : base model, where the divergent angle from 2.801 degrees (see Model 1a, Figure 4.1(1a)).

(1b) Symmetric type : Increasing the divergent angle from 2.801 degrees to 3.89 degrees [31] (see Model 1b, Figure 4.1(1b)).

(2) Asymmetric type 1: Introducing contraction angles at the bottom wall at distances of 68.13 mm (1st contraction angle) and 8.22 mm (2nd contraction angle) from the location of

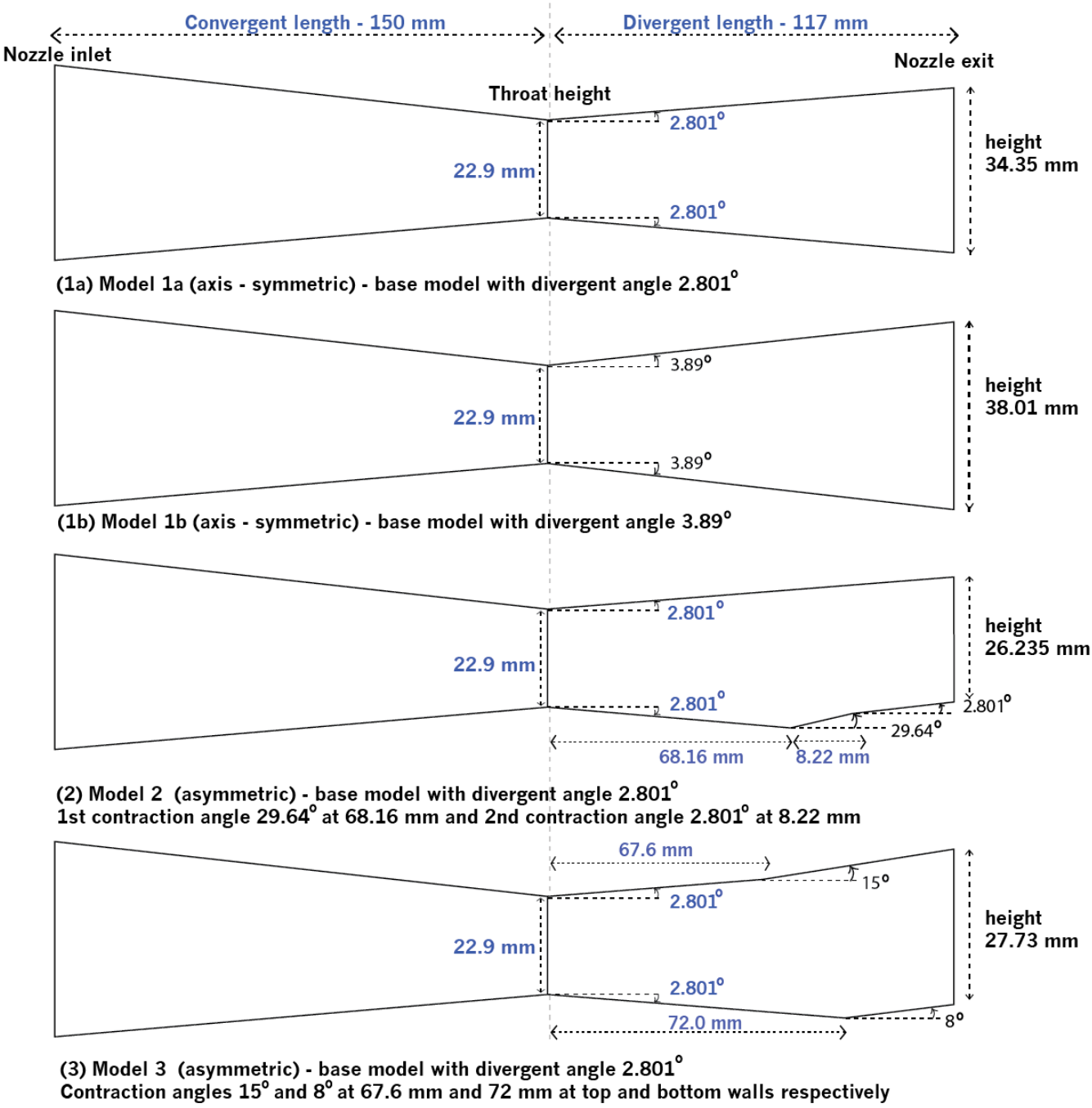

Figure 4.1: Geometry set-up: **Model 1a** (NAR 1.5), **Model 1b** (NAR 1.66), **Model 2** (NAR 1.14), **Model 3** (NAR 1.21).

the 1st contraction angle along the wall of the divergent section (see Model 2 , Figure 4.1(2)).

(3) Asymmetric type 2: Introducing contraction angles at the top and bottom walls at distances of 67.6 mm (1st contraction angle) and 72.0 mm (2nd contraction angle) of the divergent section (see Model 3 (NAR 1.21), Figure 4.1(3)).

The two asymmetric models, Model 2 and Model 3 have a divergent angle of 2.801 degrees at the nozzle throat. The asymmetry to Model 2 (NAR 1.14), 3 (NAR 1.21) is introducing contraction angles along the walls of the nozzle. The asymmetry is introduced to Model 2 by incorporating the bottom wall with two different contraction angles. The asymmetry is introduced to Model 3 by incorporating the top and bottom walls with two different contraction angles. The geometry parameters for the four models are listed in Table 4.1.

Table 4.1: **Nozzle divergent section geometry parameters for Model 1a (NAR 1.5), Model 1b (NAR 1.66), Model 2 (NAR 1.14), Model 3 (NAR 1.14).**

Nozzle Model type	**Divergent geometry parameters**
Symmetric type 1a (NAR 1.5)	Divergent length 117 mm, throat height 22.9 mm divergent angle 2.801 degrees at the throat no contraction angles nozzle exit height 34.35 mm
Symmetric type 2 (NAR 1.66)	Divergent length 117 mm, throat height 22.9 mm divergent angle 3.89 degrees at the throat no contraction angles nozzle exit height 38.01 mm
Asymmetric type 1 (NAR 1.14)	Divergent length 117 mm, throat height 22.9 mm divergent angle 2.801 degrees at the throat contraction angles at the bottom wall (1) 29.64 degrees (2) 2.801 degrees nozzle exit height 26.325 mm
Asymmetric type 2 (NAR 1.21)	Divergent length 117 mm, throat height 22.9 mm divergent angle 2.801 degrees at the throat contraction angles at the top wall 15 degrees and bottom wall 8 degrees nozzle exit height 27.73 mm

4.1.2 Computational model

The simulation area of interest, namely the convergent section, divergent section and jet plume section is modelled as a two region problem in the ANSYS CFX Design Modeler platform. Namely, Region 1 is convergent-divergent nozzle region and Region 2 as the jet plume region as illustrated in Figure 4.2. These two regions share a common region (nozzle/plume interface boundary) where the fluid is transferred from the nozzle to the plume. This common region is modelled as a fluid fluid interaction (FFI) interface, where the fluid at the exit of the nozzle interfaces (mix) with the fluid at the jet plume region.

As illustrated in 4.2 to capture the flow characteristics in the plume region, a second body, Region 2 is set-up with a width of 1000 mm and height of 300 mm. To accommodate the flow over the nozzle walls entering the plume region, the area shown as Region 2 defined at a distance of 50 mm from the nozzle exit. The plume region has an inlet area accommodating the nozzle walls and has a plume inlet has a inlet speed of 250 ms^{-1} to capture the fluid entering over the plume walls. The rest of the areas of Region 2 are set as openings boundary with ambient pressure and temperature conditions representing sea-level and high altitudes. The nozzle geometries of all four model shapes are two dimensional. Computational set up of the symmetric model NAR 1.5 is illustrated in Figure 4.2.

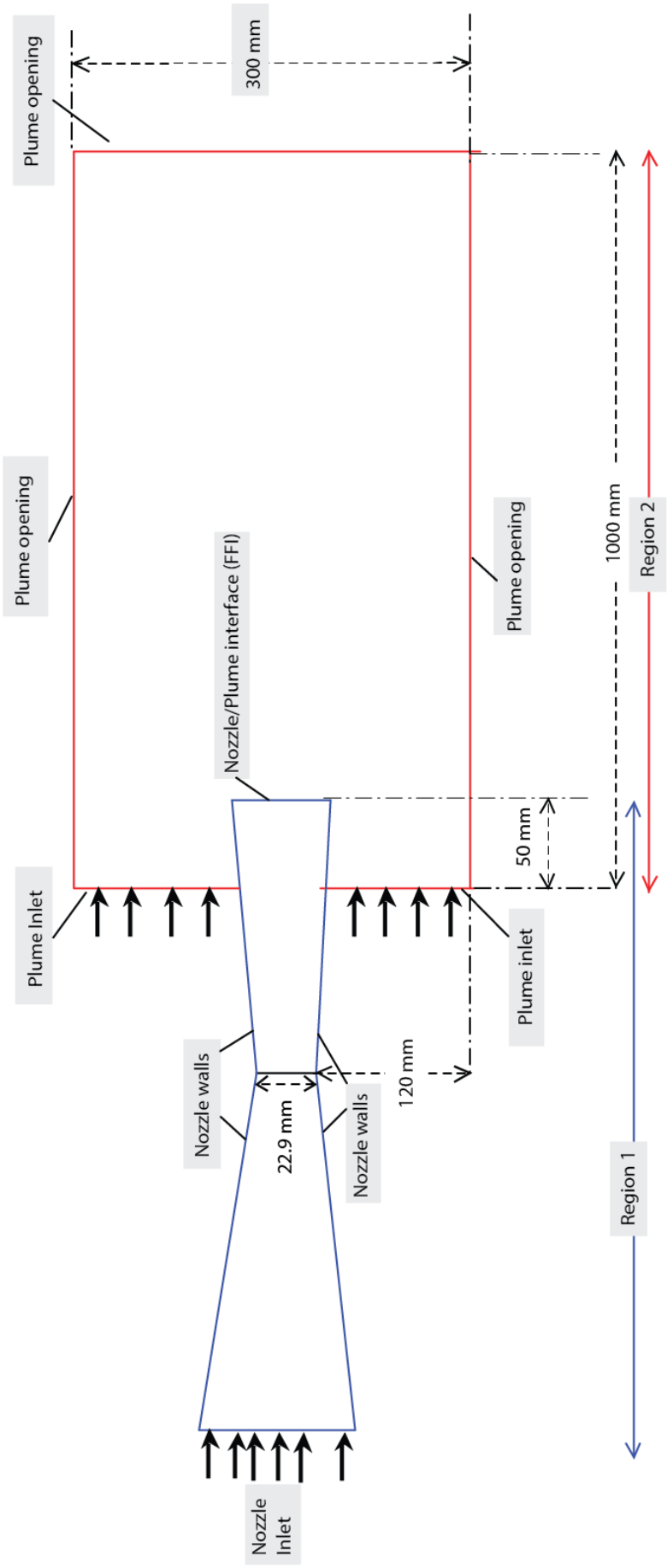

Figure 4.2: Boundary computational set up.

4.2 Mesh geometry of the models in CFX - Mesh

The Mesh generation of the two symmetric and two asymmetric models are conducted using ANSYS CFX-Mesh.

As discussed in Section 3.5 of Chapter 3, to correctly capture the internal flow separations, nozzle walls require good inflation layer mesh of the boundary layers. For a Reynolds number 5.5 $\times 10^6$ based on throat height 22.9 mm, the minimum first grid point from the wall gives the non-dimensional distance (first grid) y^+ as presented in the Table 4.2 for all models. Reynolds number is calculated using $\mathrm{Re} = \mathrm{L}\,U/\nu$, where ν is the kinematic viscosity, U is velocity based on the actual cross section area (throat area) and L is the characteristic length, which in this case is the throat diameter.

The Y plus values along the nozzle walls for Model 1a (NAR 1.5), Model 1b (NAR 1.66), Model 2 (NAR 1.14), Model 3 (NAR 1.21) for sea-level conditions for low and high NPRs are plotted and is presented in APPENDIX I.

The Mesh set-up, and the properties and parameters are summarised in Table 4.2. After conducting a Grid Independence Test (GIT), a medium unstructured mesh of 77,035 elements with 45 inflated layers for wall boundary layer meshing, was used for Model 1a (NAR 1.5) and a medium unstructured mesh of 96,693 elements with 55 inflated layers for wall boundary layer meshing, was used for Model 1b (NAR 1.66). A fine unstructured mesh of 187,767 and 268,164 elements with 45 inflated layers at the nozzle wall boundary layer meshing, for was sufficient to capture all flow instabilities for Models 2 (NAR 1.14) and 3 (NAR 1.21) respectively. The three models set in ANSYS CFX-Mesh is shown in Figure 4.3, 4.4 and 4.5. Mesh Independent test results of coarse, medium and fine meshes are provided in Figure 7.5 in APPENDIX 1.

Table 4.2: **Computational Mesh setup : Model 1a (NAR 1.5), Model 1b (NAR 1.66), Model 2 (NAR 1.14), Model 3 (NAR 1.21), see Figure 4.3, Figure 4.4 and Figure 4.5.**

Nozzle Model type	Mesh elements and parameters
Model 1a Axis-symmetric type 1 (NAR 1.5)	medium unstructured mesh 77,035 elements Y^+ value < 1, Re 5.5 $\times 10^6$ inflated layers 45
Model 1b Axis-symmetric type 2 (NAR 1.66)	medium mesh with 96,693 unstructured elements Y^+ value < 1.5, Re 5.5 $\times 10^6$ inflated layers 55
Model 2	
Asymmetric type 1 (NAR 1.14)	fine mesh with 187,767 unstructured elements Y^+ value < 1, Re 5.5 $\times 10^6$ inflated layers 45
Model 3	
Asymmetric type 1 (NAR 1.21)	fine mesh with 268,164 unstructured elements Y^+ value < 1, Re 5.5 $\times 10^6$ inflated layers 45

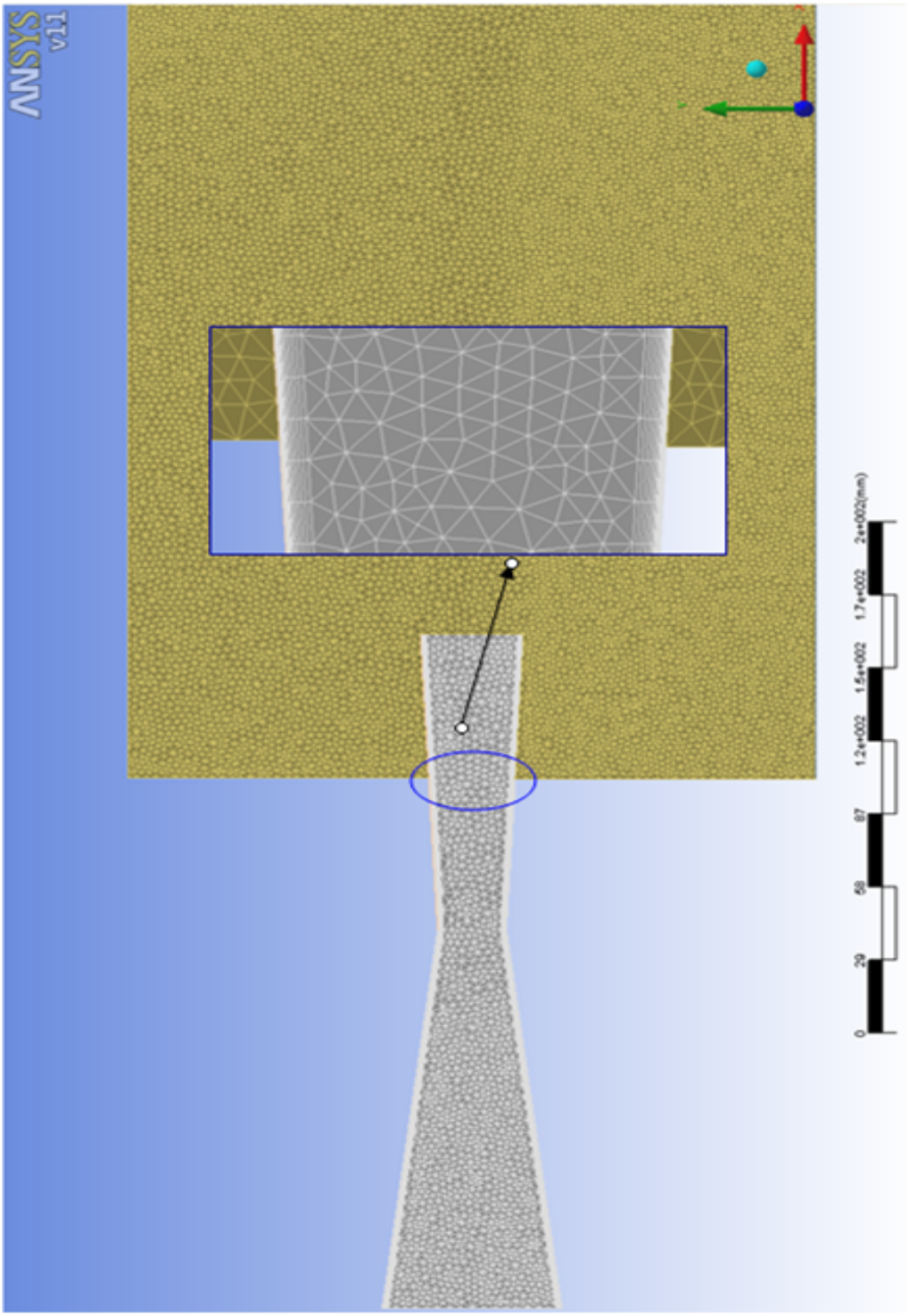

Figure 4.3: Mesh (zoomed in view) for Model 1a (NAR 1.5) with total number of 77,035 elements (unstructured).

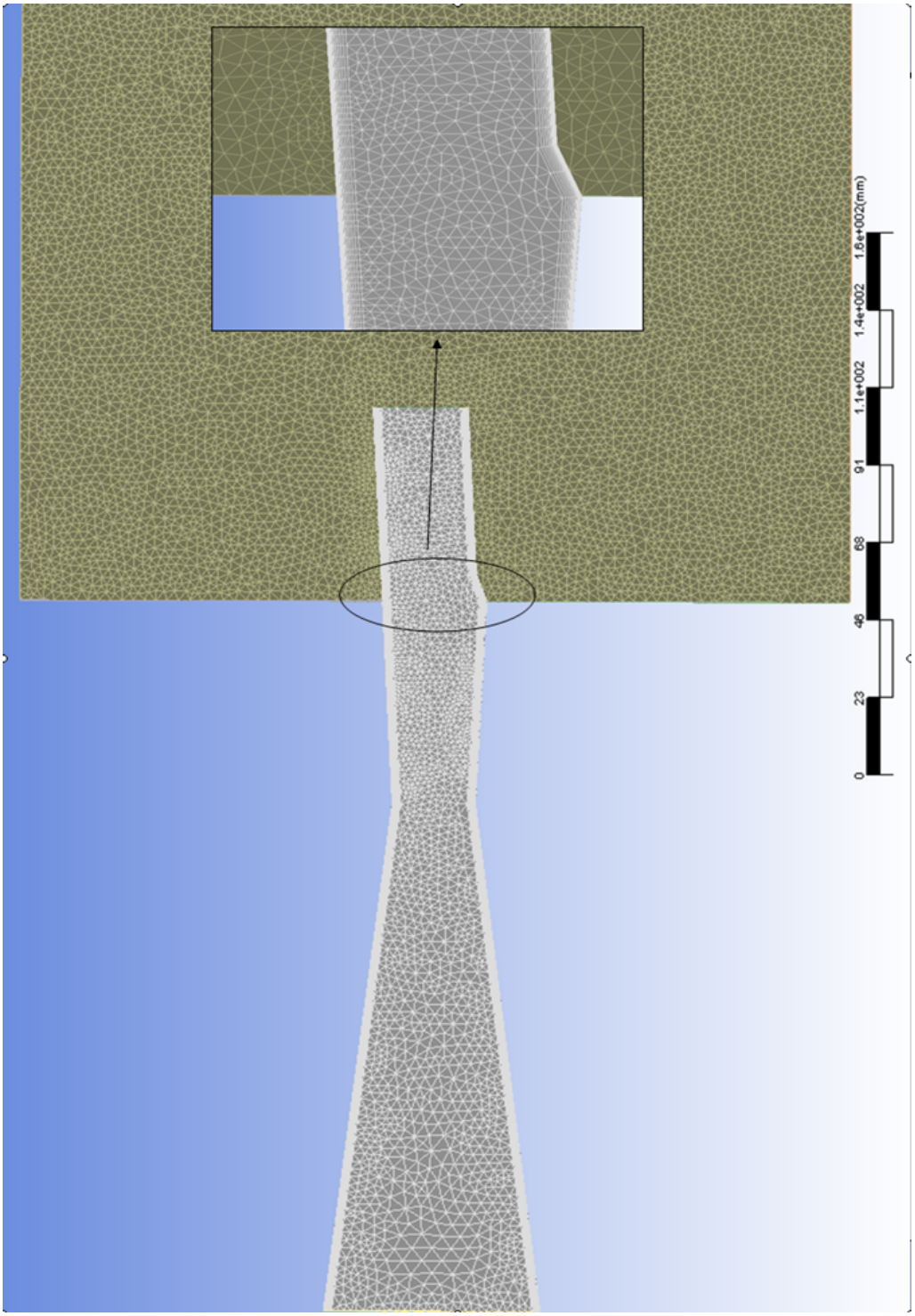

Figure 4.4: Mesh (zoomed in view) for Model 2 (NAR 1.14) with total number of 187,767 elements (unstructured).

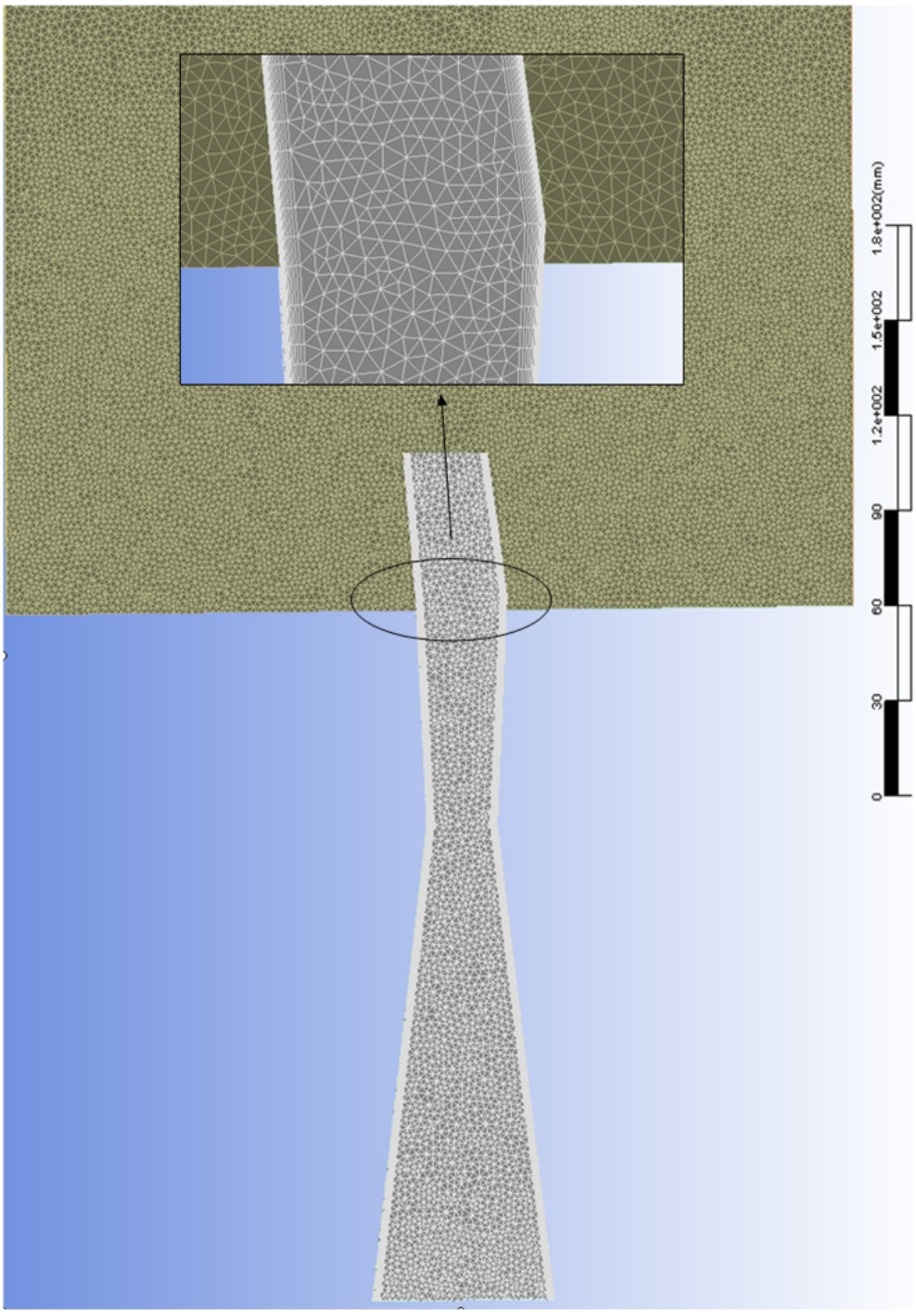

Figure 4.5: Mesh (zoomed in view) for Model 3 (NAR 1.21) with total number of 268,164 elements (unstructured).

4.3 Cruise Speed and Atmospheric conditions

To reflects the amount of thrust that the engine needs to produce. For a jet operating at low altitude where the ambient pressure is high, a propulsion devices need more thrust to expand the gas. When the altitude increases the temperature and pressure drops reducing the required thrust for the expanding gas to the operating ambient conditions. The cruising altitude of 18 - 22 km above sea level is where the temperature and pressure values are low and the air is thin. With low thrust, the jet engine can efficiently obtain high speeds, at the high altitude. The amount of thrust is directly proportional to the NPR. The graph in Figure 4.6 displays NPRs required, for designing a nozzle in the supersonic regime for an equivalent Mach number. To obtain an exhaust velocity in excess of Mach 2.0 the NPR will be ratio a of approximately 12:1. Choosing the correct operating pressure and temperature for the jet nozzle is important. Therefore, in this simulation a range of NPR 1.27 - 12.0 is used for the inlet condition settings.

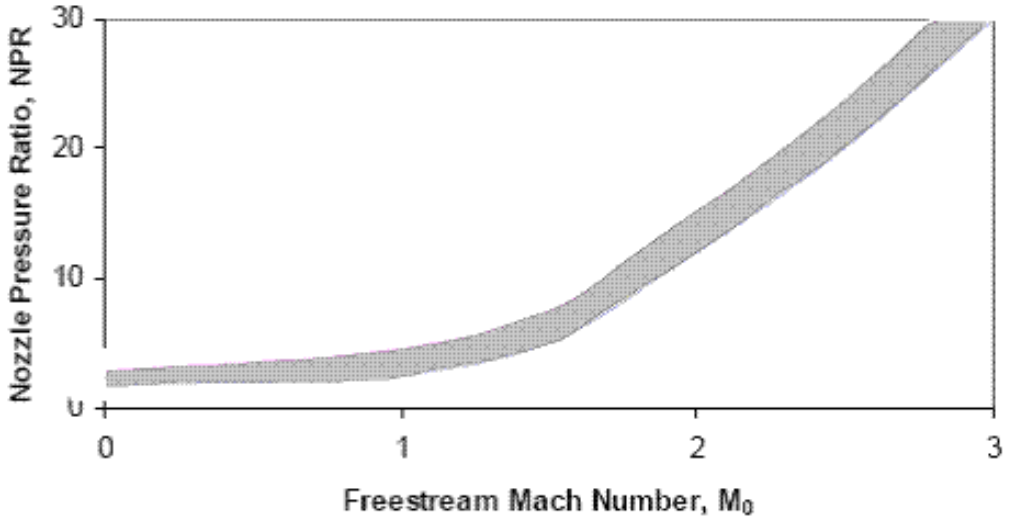

Figure 4.6: NPR vs Mach number.

4.4 Input parameters

The input parameters and assumptions made for the initial boundary conditions are summarised in Table 4.3. The initial conditions are set at sea-level conditions.

The nozzle pressure variation is modelled by increasing the inlet pressure from 1.27 atm to 12.0 atm, while keeping the nozzle ambient pressure constant, 1 atm for sea-level conditions. Flow analysis was conducted in steady state mode for all models.

Table 4.3: **Input parameters ANSYS CFX Solver**.

Input parameters	**Test data**	**Simulation condition**
Inlet pressure variation : sea-level (low NPR)	1.27 atm - 3.4 atm	NPR 1.27 to 12
Inlet pressure variation : sea-level (high NPR)	4.0 atm - 12.0 atm	NPR 1.27 to 12
Ambient pressure	1.00 atm	sea-level
Ambient temperature	290 K	sea-level
Nozzle Inlet (reservoir) temperature	500 K	Combustion temperature
Free stream velocity speed	$250 ms^{-1}$	constant around the nozzle

As presented in Table 4.4, the solver conditions are specified in ANSYS CFX solver.

Table 4.4: **ANSYS CFX Solver setting (common to all models)**.

Solver control setting ANSYS CFX Solver	solver parameter value
Advection Scheme	High resolution
Convergence control	Max iterations 5500
Convergence criteria	
Residual type	RMS
Residual target	1.E-4
Dynamic Model control	Global Dynamic Model control

The Table 4.5 lists the initial and boundary condition settings at sea level conditions of the nozzle and the plume regions in ANSYS CFX solver. In Table 4.5, the Opening boundary (Plume Opening) type describes a condition of a zero normal derivative of the fluid flow at the boundary. Whether or not the flow is supersonic or subsonic at the boundary makes no difference in the simulation results, as long as the Zero Gradient is chosen for the Turbulence Option. The residual convergence history plots for the axis-symmetric model, NAR 1.5 are provided in Figure 7.6 - 7.9 in APPENDIX 1.

Table 4.5: **Fluid-Domain and model boundary settings at sea level conditions**).

Fluid Domain : Initial Conditions	
Fluid Material	Air Ideal gas
Morphology	continues fluid
Buoyancy Model	Non Buoyant
Heat Transfer Model (Includes viscous work term)	Total Energy
Reference pressure	1 atm
Turbulence Model	SST Model
Turbulent Wall functions	Automatic
Domain Interface type	Fluid-Fluid
Mass and Momentum	Conservative Interface Flux
Boundary : Inlet	
Flow direction	Normal to boundary condition
Flow regime	subsonic
Heat Transfer	Static temperature 500 K
Relative pressure	1.27 atm - 12.0 atm
Turbulence	k and Epsilon
Boundary : Plume Inlet	
Flow regime	Subsonic
Heat transfer	static temperature (290 K)
Mass and Momentum	Cartesian Velocity Components
U V W	U= 250 ms^{-1}, V=W=0
Turbulence	Medium Intensity and Eddy Viscosity ratio
Boundary : Domain Boundary Interface	FFI Interface (Fluid to Fluid)
Mass,Momentum and Heat Transfer	Conservative Interface Flux
Turbulence	Conservative Interface Flux
Boundary : Plume Opening	
Flow regime	Subsonic
Heat transfer	opening temperature (290 K)
Relative Pressure	1 atm
Turbulence	Zero gradient
Boundary : Nozzle Walls	
Heat Transfer	Adiabatic
Mass and Momentum	No Slip Wall

4.5 Exhaust velocity Thrust and Jet Deflection Angle Calculations

Total thrust of the nozzle exhaust is a combination of total internal pressure forces, external forces and static pressure of the reservoir (combustion chamber). The following equation is used to calculate the forces acting on the divergent section of the nozzle which includes the top wall, bottom wall and the nozzle exit area. The pressure force is the total of static and dynamic pressures. Internal and external forces are acting perpendicular to the nozzle walls. The thrust (T) is given by [12];

$$T = (P_{top} - P_\infty) dA_{top}\hat{\mathbf{n}} + (P_{bottom} - P_\infty) dA_{bottom}\hat{\mathbf{n}} + (P_{exit} - P_\infty) dA_{exit}\hat{\mathbf{n}} + d\dot{m}\widetilde{\mathbf{V}} \tag{4.1}$$

When the total forces acting on X direction is T_X and Y direction is T_Y, the total thrust of the nozzle engine is given by;

$$Total\ Thrust = \sqrt{T_X^2 + T_Y^2} \tag{4.2}$$

where the angle of the total thrust is $\tan^{-1}(\mathrm{T}_Y/\mathrm{T}_X)$. This angle is known as the jet deflection angle.

P_{top} - pressure on the top nozzle wall of the divergent section.

P_{bottom} - pressure on the bottom nozzle wall of the divergent section.

P_{exit} - pressure along the vertical height at the exit of the nozzle.

P_∞ - ambient pressure

A_{top}, A_{bottom}, A_{exit} - surface areas of the top wall, bottom wall and exit of the nozzle.

$\hat{\mathbf{n}}$ - normal vector to the surface/wall.

$\dot{m}$ - mass flow rate ($\rho \times \mathbf{V} \times \mathrm{A}$)

$\widetilde{\mathbf{V}}$ - free stream velocity

Chapter 5

Results and Discussion

In this chapter, the simulation results obtained from ANSYS CFX solver on the symmetric and asymmetric nozzle configurations are presented. This investigation is carried out in two stages, which covers the two nozzle configurations tested under low and high NPRs. During the first stage of the investigation, the two symmetric nozzle types, NAR 1.5 (Model 1a) and NAR 1.66 (Model 1b) and during the second stage of the investigation, the two asymmetric nozzle types, NAR 1.14 (Model 2) and NAR 1.21 (Model 3) as described in Chapter 1 were simulated with the boundary conditions provided in Table 4.4 in Chapter 4.

The two symmetric and two asymmetric models were tested under sea-level conditions (ambient pressure 1.00 atm). The NPR variation tested during this investigation for symmetric and asymmetric models are presented in Table 5.1.

Table 5.1: **NPR variation range**.

Input condition	**NPR variation range**
symmetric models (NAR 1.5 and NAR 1.66)	NPR 1.27 - 2.7 (Low NPR) and 3.4 - 12.0 (High NPR)
asymmetric models (NAR 1.14 and NAR 1.21)	NPR 1.27 - 2.7 (Low NPR) and 3.4 - 12.0 (High NPR)

Simulation results and discussion on the symmetric and asymmetric nozzles types is structured according to the NPRs tested to accommodate the flow characteristics under low and high NPRs. The simulation is carried out for low NPRs, where the pressure variation is between 1.27 - 2.4 and high NPRs, between 3.4 - 12 on both symmetric and asymmetric nozzle configurations as listed in Table 5.1.

5.1 Symmetric Nozzle Types (NAR 1.5 and NAR 1.66)

5.1.1 Symmetric Nozzle Types : Low NPRs

The effect of NAR is compared for symmetric type nozzles, NAR 1.5 and NAR 1.66. These symmetric nozzle types are simulated under low NPRs between 1.27 - 2.4 are presented and discussed in this section.

Since this study does not perform any experimental analysis to validate the computational results, they were validated through similar investigations carried out on NAR 1.5 and NAR 1.66 in past literature. The computational results obtained under low NPRs, between 1.27 - 2.4 for symmetric models NAR 1.5, 1.66 are closely validated with the simulation results achieved for Mach numbers by Xiao, et al solved for flow separation of the supersonic flow, for investigations carried out for nozzle geometry types NAR 1.5 [31] and NAR 1.66 [32]. Further, internal nozzle flow separation, boundary layer separation and *Lambda* shocks under adverse pressure gradients, which occur internally in the nozzle divergent section were justified through the past literature.

The effects of the flow speeds (Mach Number), Mach Shock location (Mach.L(m)) and internal flow separation characteristics at low NPRs at sea-level condition with comparison to Xiao, et al [2007] on nozzle shape NAR 1.5 [31] are listed in Table 5.2.

Table 5.2: **Internal flow separation conditions on NAR 1.5, NAR 1.66 and Xiao, et al [2007] NAR 1.5 [31], at sea-level conditions (Mach.No: Mach Number, Mach.L: location to highest Mach number, axial direction from the throat)**

NAR 1.5				**NAR 1.66**				**Xiao, et al NAR 1.5**		
NPR	Mach.No	Mach.L(m)	Separation	**NPR**	Mach.No	Mach.L(m)	Separation	**NPR**	Mach.No	Separation
1.27	1.226	0.0152	asymmetric	1.27	1.385	0.0290	asymmetric	1.27	1.23	symmetric
1.34	1.316	0.0213	asymmetric	1.34	1.395	0.0384	asymmetric	1.34	1.39	symmetric
1.40	1.347	0.0226	asymmetric	1.40	1.415	0.0472	asymmetric	1.47	1.44	symmetric
1.61	1.441	0.0362	asymmetric	1.61	1.453	0.0613	asymmetric	1.61	1.50	asymmetric
1.79	1.576	0.0453	symmetric	1.79	1.779	0.0724	asymmetric	1.70	1.56	asymmetric
1.82	1.782	0.0544	shock at exit	1.96	1.818	0.1170	shock at exit	2.3	1.67	asymmetric
2.4	1.847	0.0673	Overexpanded	2.4	1.899	0.1237	uniform	2.4	1.69	symmetric

The results archived for Mach numbers for NAR 1.5 were closely validated with the computational results obtained by Xiao, et al [2007] solved for flow separation of the supersonic

nozzle, NAR 1.5 geometry configuration at low NPR [31].

Observing the data listed in Table 5.2, internal flow characteristics at lower NPRs in NAR 1.66 reaches symmetric flow separation conditions at low Mach numbers in comparison to NAR 1.5. The Mach location (Mach.L), which is the distance from the throat to the nozzle exit/plume opening to the highest Mach number measured from the throat, is summarised against low NPRs (1.27 atm to 2.4 atm), for NAR 1.5 and NAR 1.66. From the summarised data in Table 5.2, higher Mach number values are achieved from increasing the divergent angle at the divergent section of the nozzle. Internal nozzle flow separation, boundary layer separation and *Lambda* shocks under adverse pressure gradients are presented in Figure 5.1 for increasing NPRs. Figure 5.1 (c) for NAR 1.66, shows the Mach contours for a flow with low NPRs at sea-level conditions. The flow separation due to shocks is clearly visible. The *Lambda* shock wave is visible while a second *Lambda* shock is also visible further down stream (Figure 5.1(c)).

The size of the *Lambda* foot amplifies to cause a bigger separation zones. The size of the lambda foot influences the size of the separation zone on the opposite wall. As NPR increases from 1.27 to 1.76 (see Figure 5.1) (a) to (c), the separation zone moves from one wall to the other (as shown in Figure 5.1 (a) to (c)). With the increase of NPR from 1.27 to 1.76, the flow undergoes separation from asymmetric to symmetric before leaving the nozzle exit as symmetric flow (NPR 1.79). The flow separation occurs in CD nozzles as a result of pressure ratios been lower than at a design value, which generates shocks inside the nozzle. Noted by Papamoschou, D. and Zill, A., [2004] the close proximity of the wall to the separation shear layer has been cited as a possible reason [28]. Density drop across at the divergent section, where the Lambda shocks and shock induced boundary layer separation occurs inside the nozzle under low NPRs. Density Contours of the model, NAR 1.66 at NPR 1.27 and 1.40 are shown in Figures 5.3, 5.4 and 5.5.

This transition from one wall to the other is due to the build up of turbulent kinetic energy on the opposite wall, as the pressure increases. TKE for NAR 1.66 is shown in Figure 5.2. TKE dissipation is observed highest when the nozzle's separation bubble is bigger, see Figures 5.1 (b) and 5.2 (b).

High sensitivity of the turbulence model, SST has captured the internal nozzle flow characteristics such as, shock induced flow separation and *Lambda* shocks, which is thoroughly visible from the case carried out at low NPRs for NAR 1.66, see Figure 5.1. The flow downstream

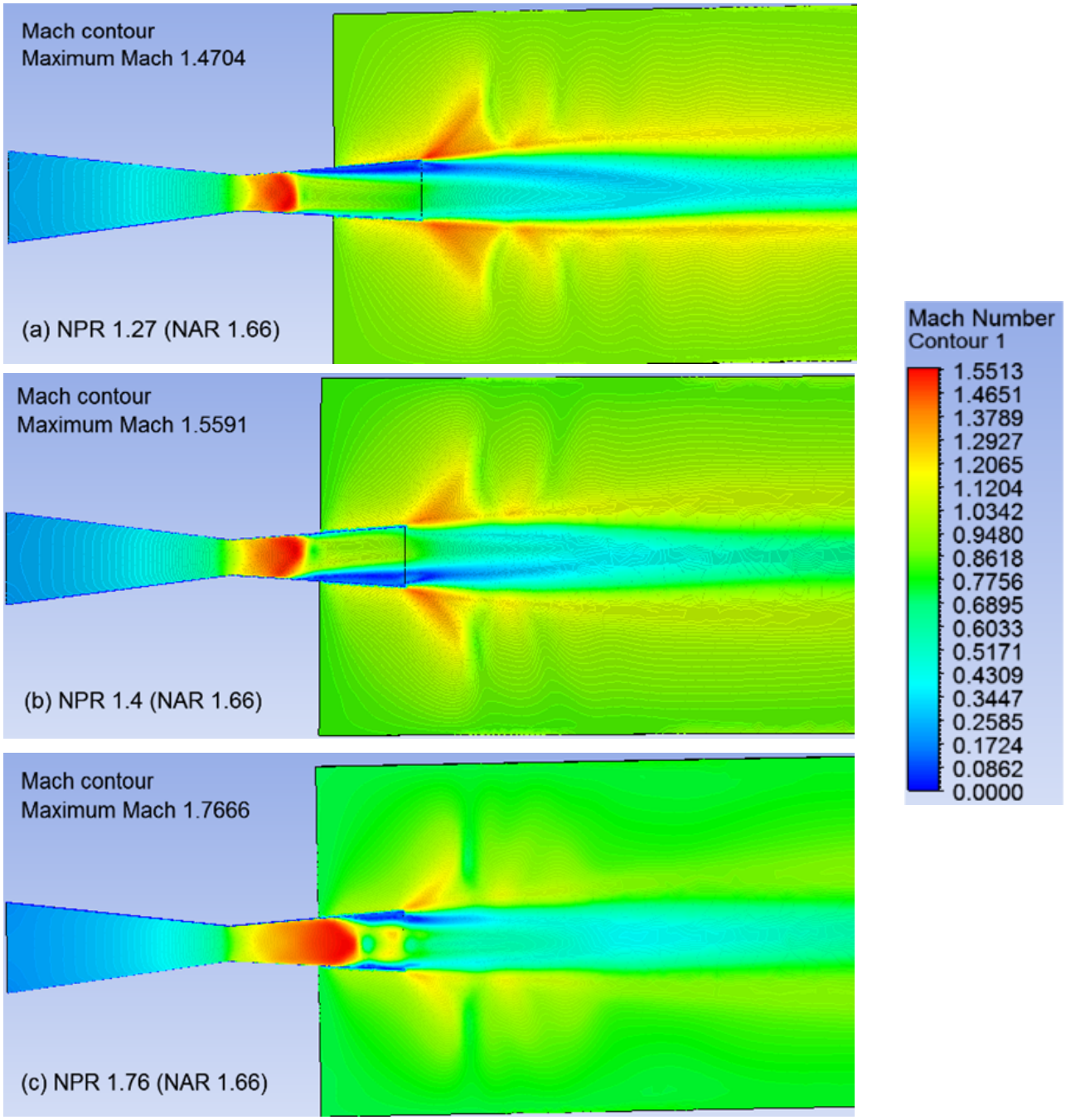

Figure 5.1: Mach Contours : NAR 1.66 Nozzle flow separation and shock formation NPR: (a) 1.27 (b) 1.4 (c) 1.76.

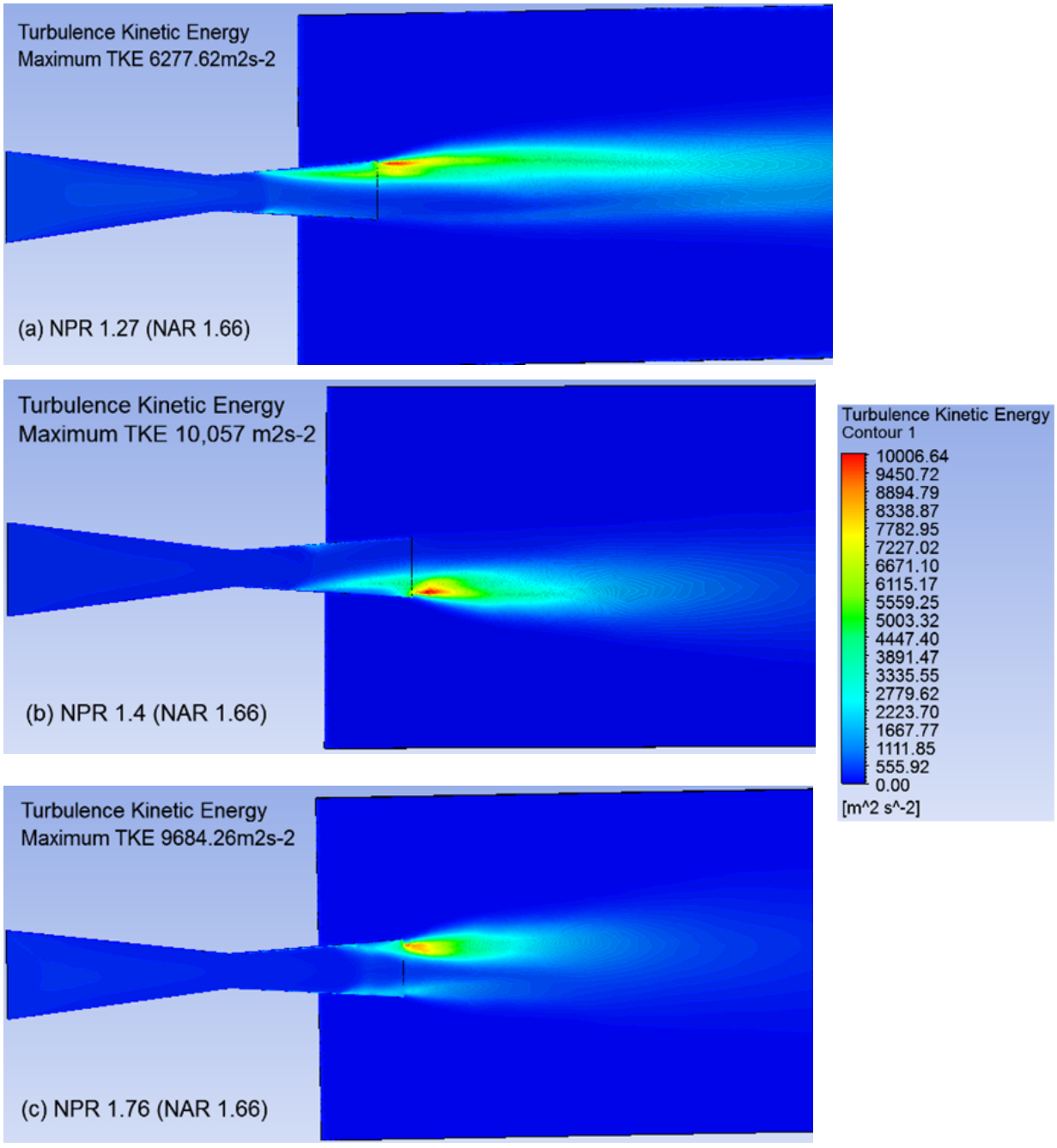

Figure 5.2: Turbulent Kinetic Energy (TKE) values NAR 1.66 NPR: (a) 1.27 (b) 1.4 (c) 1.76.

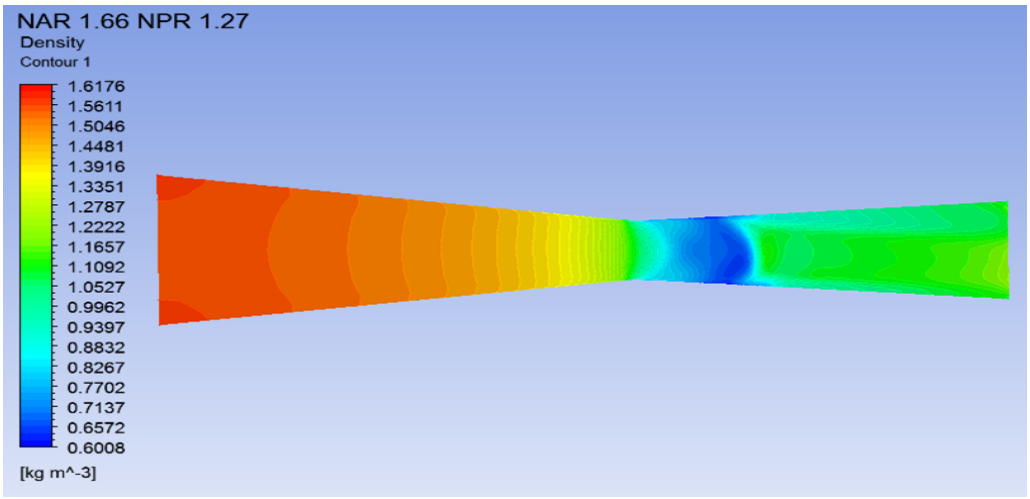

Figure 5.3: Density contours, NAR 1.66, NPR 1.27

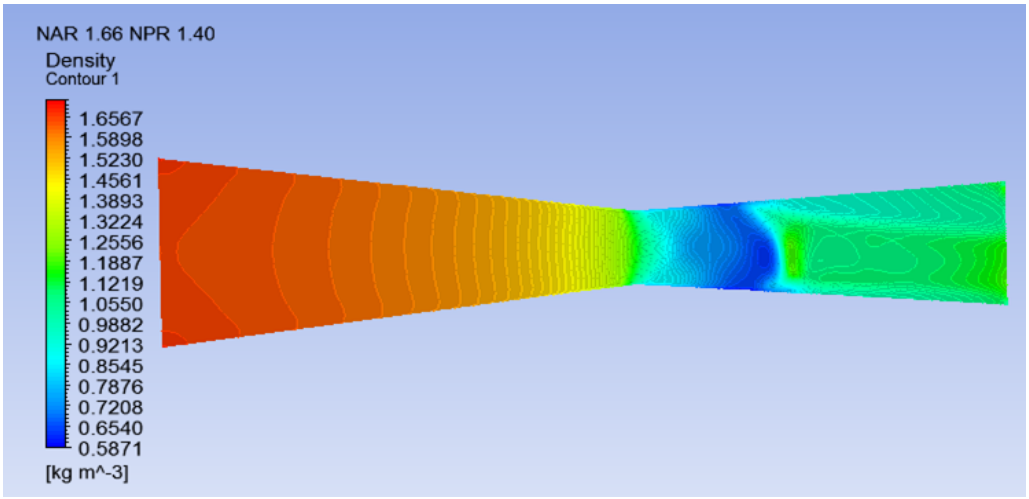

Figure 5.4: Density contours, NAR 1.66, NPR 1.40

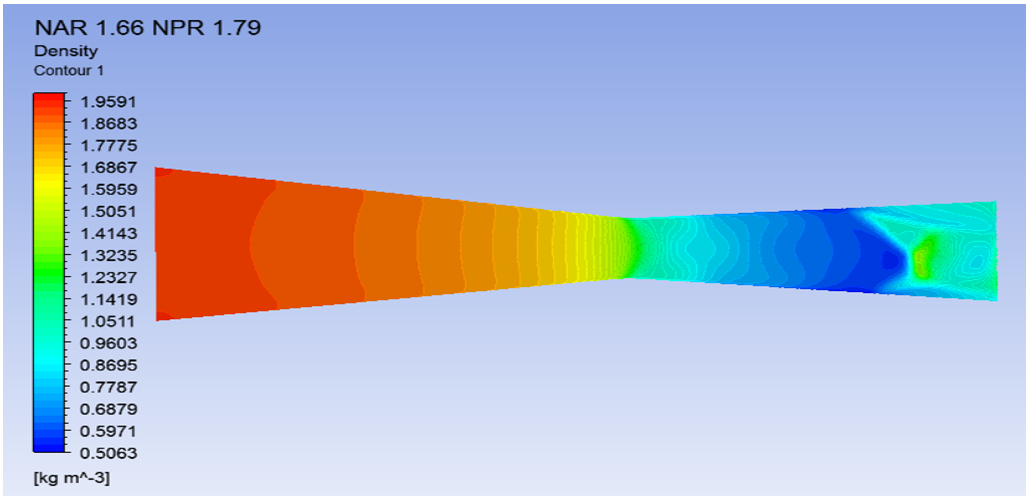

Figure 5.5: Density contours, NAR 1.66, NPR 1.79

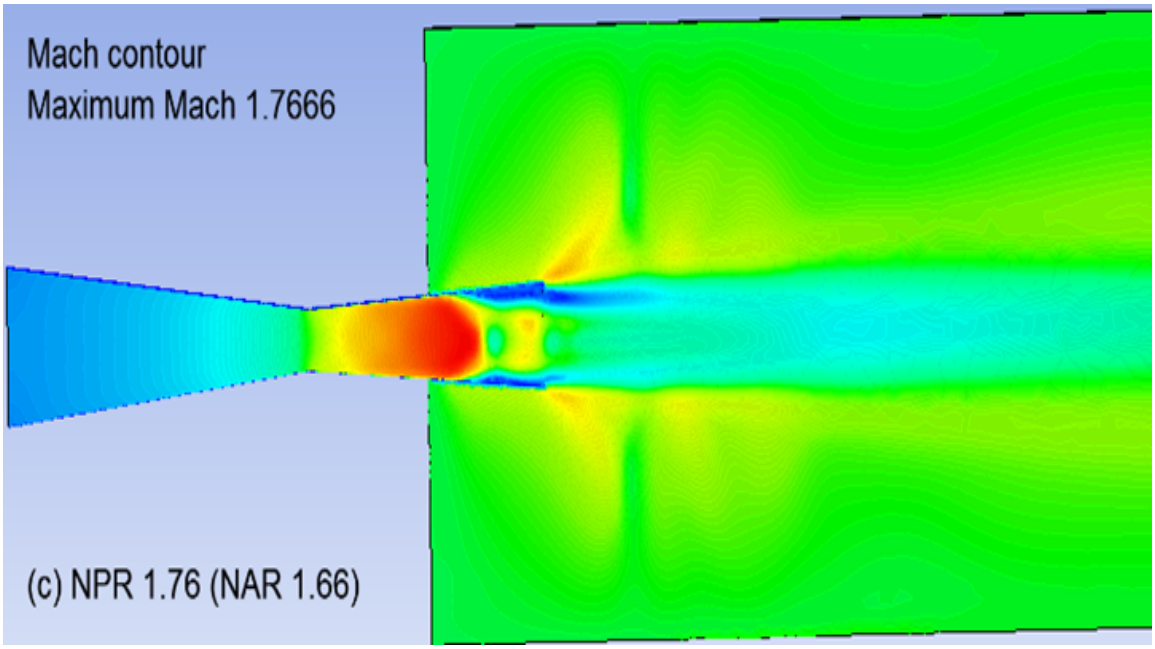

Figure 5.6: Flow Separation and Lambda shocks, NAR 1.66, NPR 1.76

of the nozzle experiences asymmetric separation due to the boundary layer detachment from the wall creating a *Lambda* foot shock wave which is followed by a second *Lambda* foot shock, see Figure 5.6. Increase in an adverse pressure gradient near the walls influence the flow to reverse which causes the flow separation along the boundary layer (nozzle walls) of the divergent section of the nozzle.

Figure 5.7 shows the Mach number variation across the total horizontal nozzle length for NPR 1.80, Model 1b (NAR 1.66) when the shock induced flow separation and *Lambda* shocks are experienced by the symmetric type nozzles. The separation of the flow becomes symmetric with small separation bubbles at both top and bottom walls, see Figure 5.6.

Mach number variation on different heights measured vertically upwards from the center of the throat is displayed, see Figure 5.7. Mach contours for various distances measured vertically, starting 1 mm to 11.5 mm at the nozzle throat across the total horizontal nozzle length (horizontal distance X[m] - 150 mm to convergent section and 117 mm to the divergent section of the nozzle) at NPR 1.80 is displayed in Figure 5.7. This is a flow phenomena under similar pressure ratio condition, as shown in Figure 5.6. Mach contours measured at the vertical heights 0.01 mm and 1 mm from the nozzle walls no significant influence by the shock variation is visible, see Figure 5.6 and Figure 5.7. This is due to the vertical height of the *Lambda* foot shock not reaching the total throat height. The first drop of the Mach number value is due

to the *Lambda* shock wave. The flow regains velocity and subsequently drops again due to the formation of the second *Lambda* shock. The maximum Mach number is displayed for the variation across 17.5 mm from the bottom of the nozzle wall.

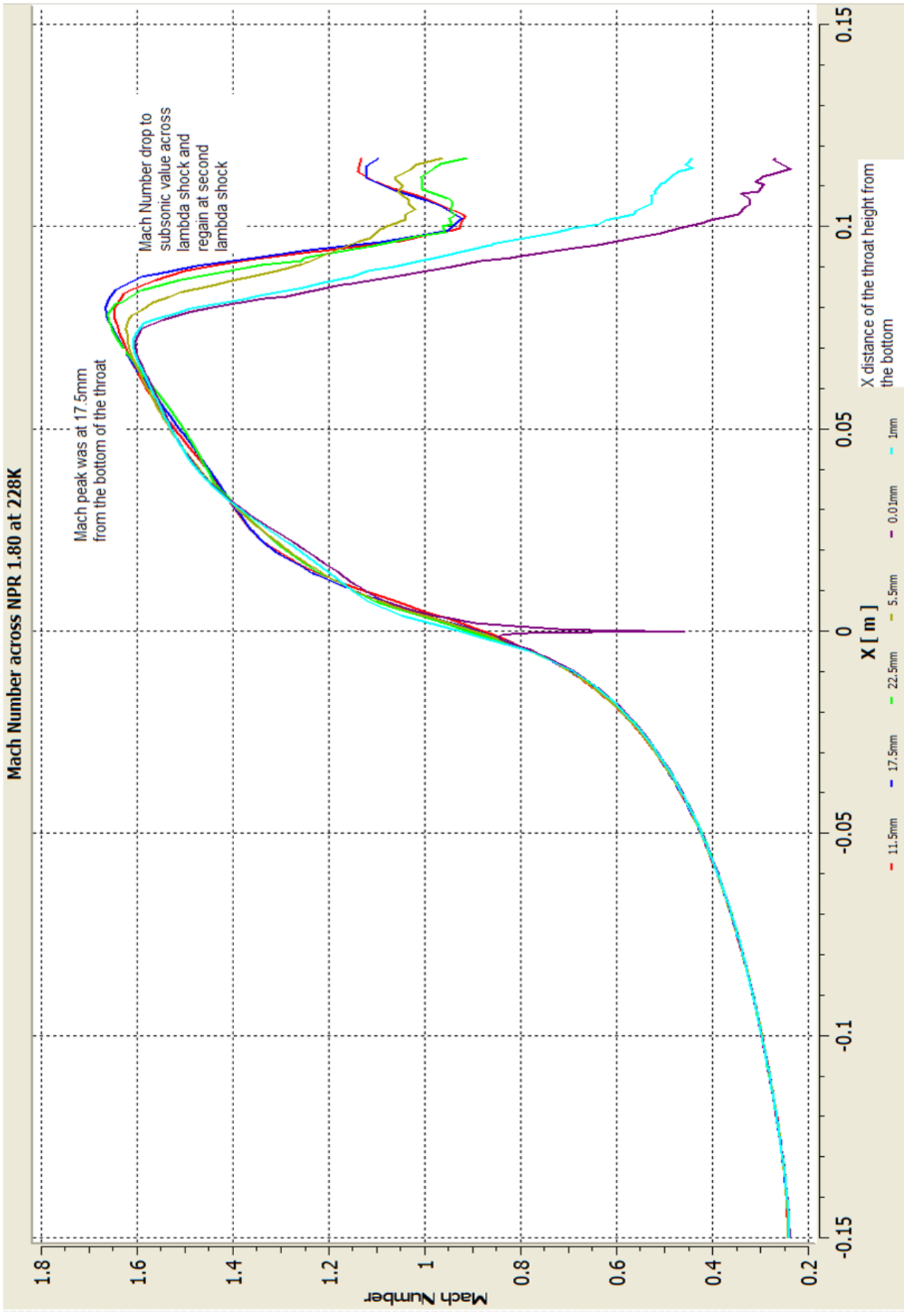

Figure 5.7: Mach number across the total horizontal nozzle length for NPR 1.80, NAR 1.66

With the increase of the NPR to the symmetric model, the flow becomes *Overexpanded* and the *Oblique* shock waves at the exit of the nozzle turns inward. This is caused when the external free stream flow passing on the top and bottom walls at the end of the divergent section of the nozzle is met at the exit with the internal shocks, as described in Section 2.2, Chapter 2 which is visible in NAR 1.66 at NPR 2.1, see Figure 5.8.

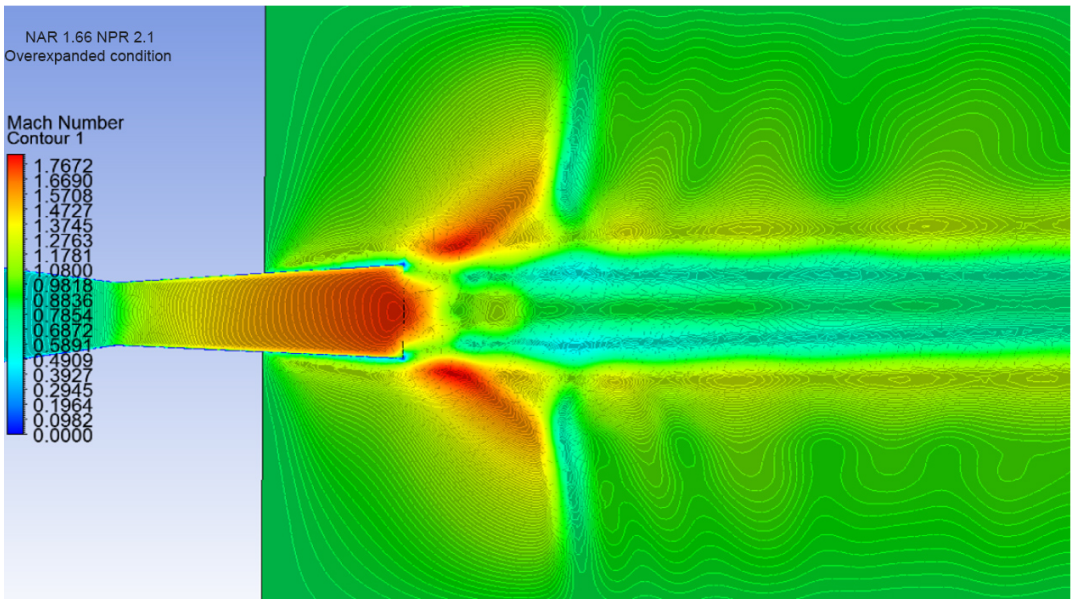

Figure 5.8: NAR 1.66 *Overexpanded* condition with *Oblique* shock waves formed at the nozzle exit.

5.1.2 Symmetric Nozzle Types : High NPRs

The NAR 1.5 and NAR 1.66 is tested under high NPRs, varying between 3.4 - 12.0 are presented in this section. The flow is subjected to high NPRs to observe the flow characteristics at the external jet plume region. In Table 5.3 is summarized against high NPRs (3.4 - 12.0), for NAR 1.5 and NAR 1.66.

The effect of the symmetric nozzle with different divergent area ratios are tested. In Table 5.3, it is evident that the nozzle type NAR 1.66, shows a significant increase in the Mach number when compared to nozzle type NAR 1.5, which is influenced by having a larger divergent angle, that is from 2.801 degrees to 3.89 degrees. The flow characteristics such as uniform flow and *Underexpansion* flow conditions, for nozzle type NAR 1.66, were gained faster in comparison to nozzle type NAR 1.5, see Table 5.3.

Table 5.3: **Mach Number against High NPR for NAR 1.5, 1.66 under sea-level conditions**

NPR	**NAR 1.5 Mach No**	**NAR 1.66 Mach No**	**Flow Condition**
5.5	1.8199	2.0801	*Overexpanded*
7.0	1.8275	2.0998	Uniform flow
10.0	2.0412	2.1042	*Underexpanded*
12.0	2.1689	2.1993	*Underexpanded*

Since the free stream speed surrounding the nozzle is set to 250 ms^{-1}, the influence of this external nozzle flow is observed when the flow is highly *Underexpanded*.

Mach contours for the nozzle type NAR 1.5 at low and high NPRs are shown in Figure 5.9 and 5.10. When the NPR is increased from low to high values, the shocks propagation from inside the nozzle to the jet plume regions is shown in the Figure 5.9 and 5.10. From the stage of internal nozzle flow being asymmetric (flow separation, see Figure 5.9) to jet plume Mach Shock Diamonds outside the nozzle are visible from low to high NPR increase, see Figure 5.10.

Internal flow characteristics (asymmetric flow separation) to Mach Diamond shocks in jet plume region in a traditional CD nozzle as shown in Figure 2.2 in Chapter 2, is visible in Mach contour plots obtained from the simulation results, see Figures 5.9 and 5.10.

Increasing the nozzle pressure ratio (NPR) from 1.27 to 2.4 for the traditional CD nozzle, the unique flow phenomena starting of internal asymmetric flow separation to *Overexpansion* of the nozzle under low NPRs, as described in Chapter 2 are shown in simulation results for symmetric model NAR 1.5, see Figure 5.9. The flow being *Overexpanded*, with further increase of NPR, flow regains speed under the influence of the *Overexpansion*, and becomes uniform flow known as ideal condition, and finally becomes *Underexpanded* which forms the shapes of the Mach Shock Diamonds as described in Figure 2.2, Chapter 2, see Figure 5.10.

5.1.3 Mach Contours: Symmetric model NAR 1.5: Low NPR

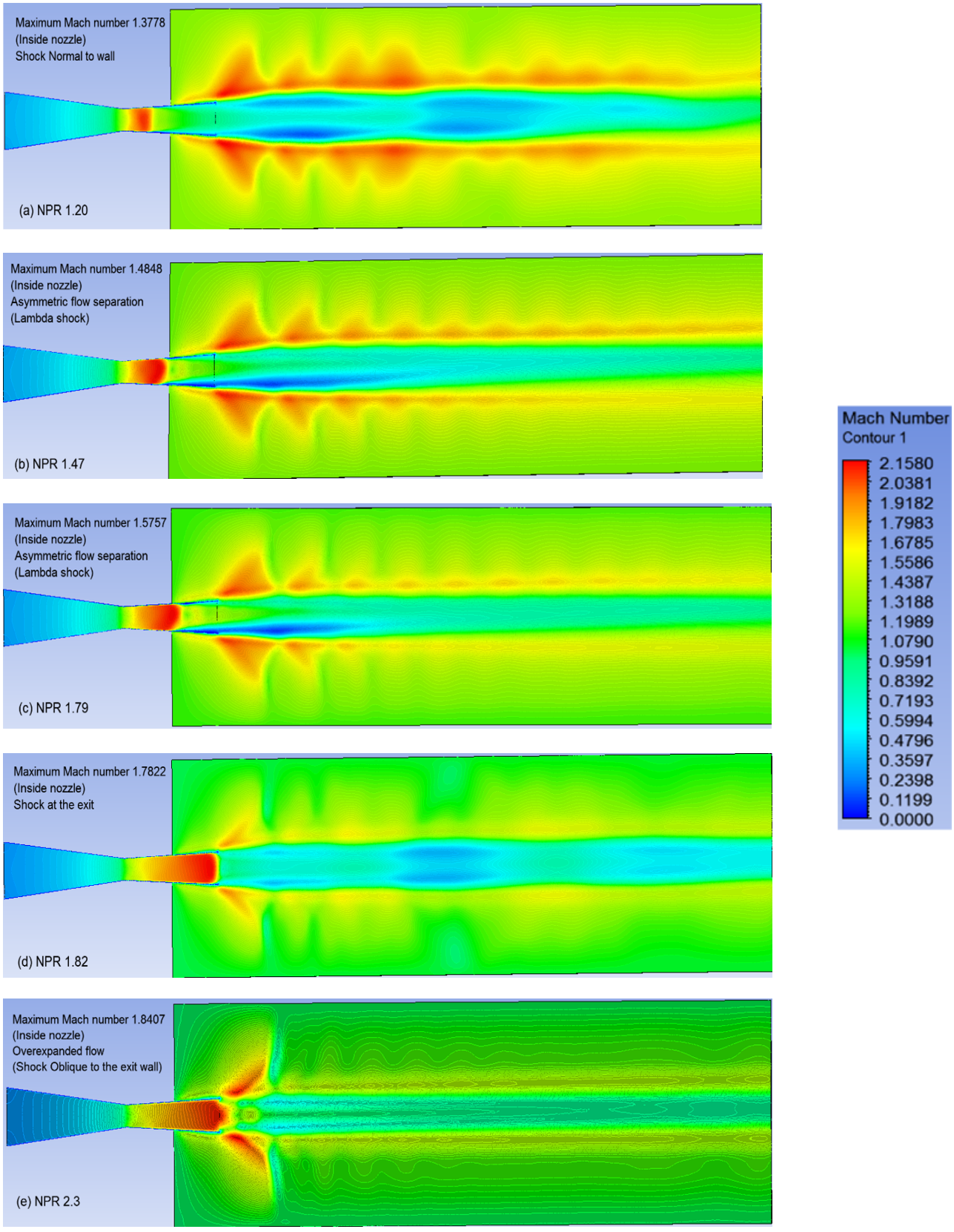

Figure 5.9: Mach contours: NAR 1.5, NPR: (a)1.2 (b)1.47 (c)1.79 (d)1.82 (e)2.3

5.1.4 Mach Contours: Symmetric model NAR 1.5: High NPR

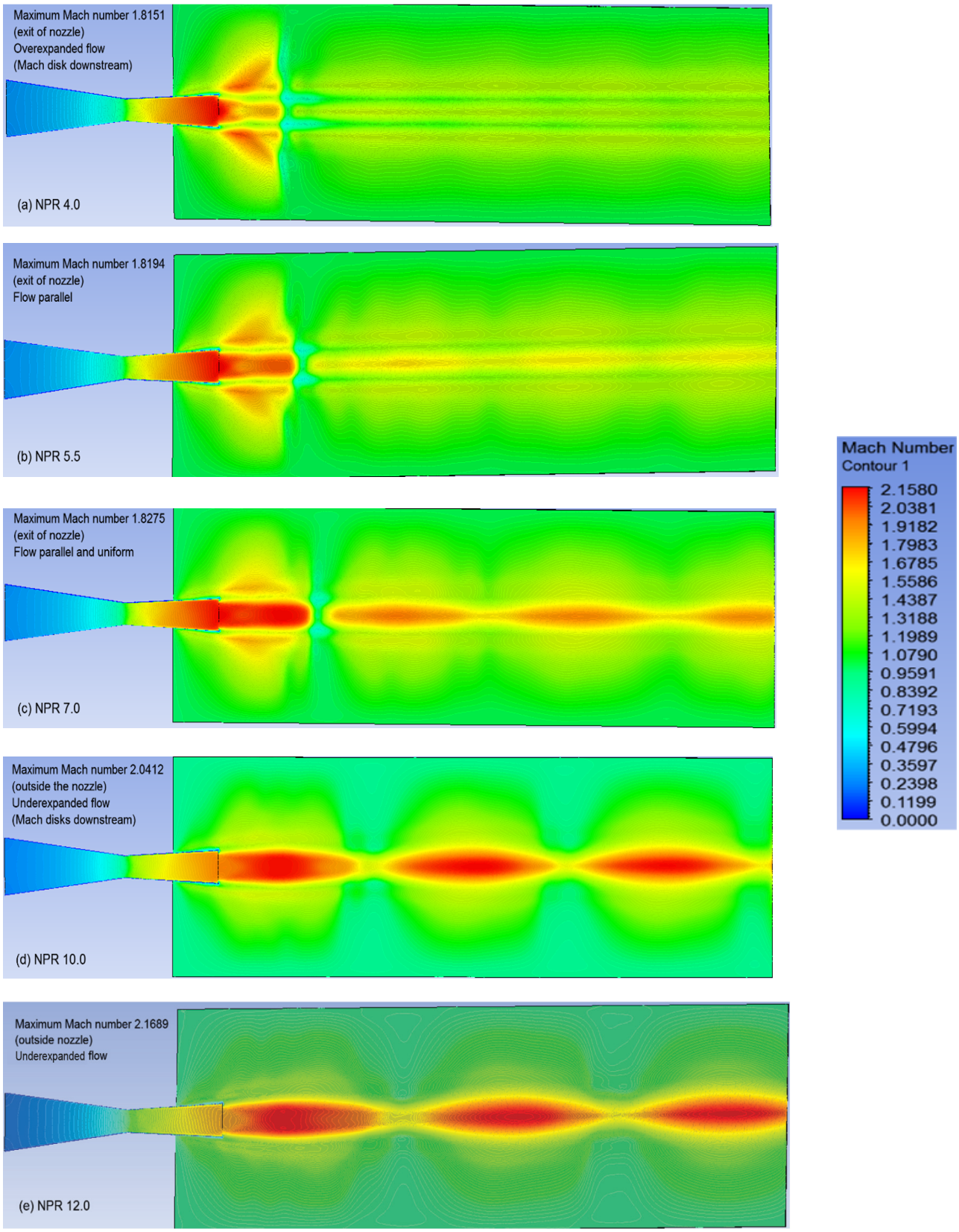

Figure 5.10: Mach contours : NAR 1.5, NPR: (a)4.0 (b)5.5 (c)7.0 (d)10.0 (e)12.0

5.2 Asymmetric Models

5.2.1 NAR 1.14 and NAR 1.21: Low NPRs

Asymmetric nozzle types, NAR 1.14 (Model 2) and NAR 1.21 (Model 3) are under medium to low NPRs presented in this section. The range of the NPR chosen for this asymmetric configuration are higher than of the symmetric types. Internal flow characteristics subjected to geometry variations at the divergent section of the nozzle in comparison to the symmetric nozzle types are compared.

It was observed, at NPRs varying from 2.4 - 3.4, the nozzle still remained choked and shocks were still close to the nozzle throat. When the nozzle NPR is increased further, flow separation with *Lambda* foot shock and second half *Lambda* foot shock is observed for asymmetric type NAR 1.14 at NPR 4.4, which is shown in Figure 5.10.

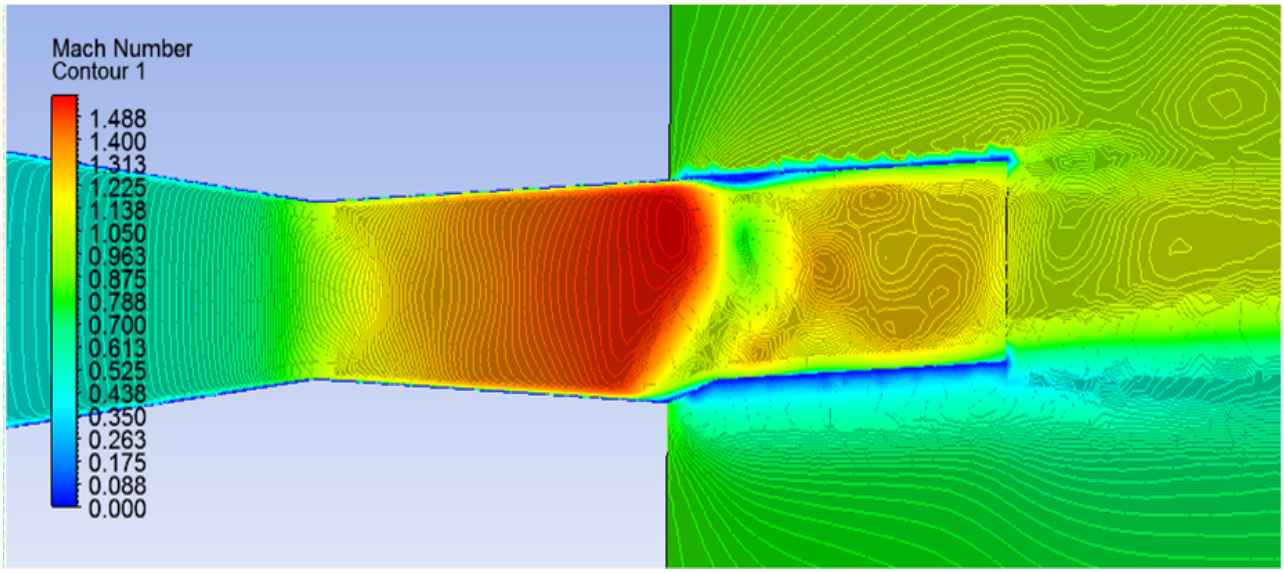

Figure 5.11: Flow Separation with *Lambda* Shock formation for Model 2 (NAR 1.14), NPR 4.4.

Asymmetric type NAR 1.14 and type NAR 1.21 are compared under low-to-medium NPRs for internal flow characteristics subjected to geometry variations at the divergent section of the nozzle. When the nozzle is under low pressure ratio, flow separation with *Lambda* foot shock and second half *Lambda* foot shock is observed for asymmetric types NAR 1.14 at NPR 5.0, as shown in Figure 5.11. Introduction of the contraction angle has an influence towards the size of the foot of the *Lambda* shocks.

The *Lambda* foot shock was not visible in nozzle type NAR 1.21 as shown in Figure 5.12. For

medium to high NPRs, flow separation and internal shocks will not be formed for this geometry shape, hence exhaust flow with less energy loss in thrust can be obtained. The NAR 1.21, with an angle variation to top and bottom walls, generates a different shock pattern internally at the divergent section of the nozzle reducing the Mach number value in comparison to traditional CD nozzle under same NPR. The influence of change in geometry at the divergent section of the

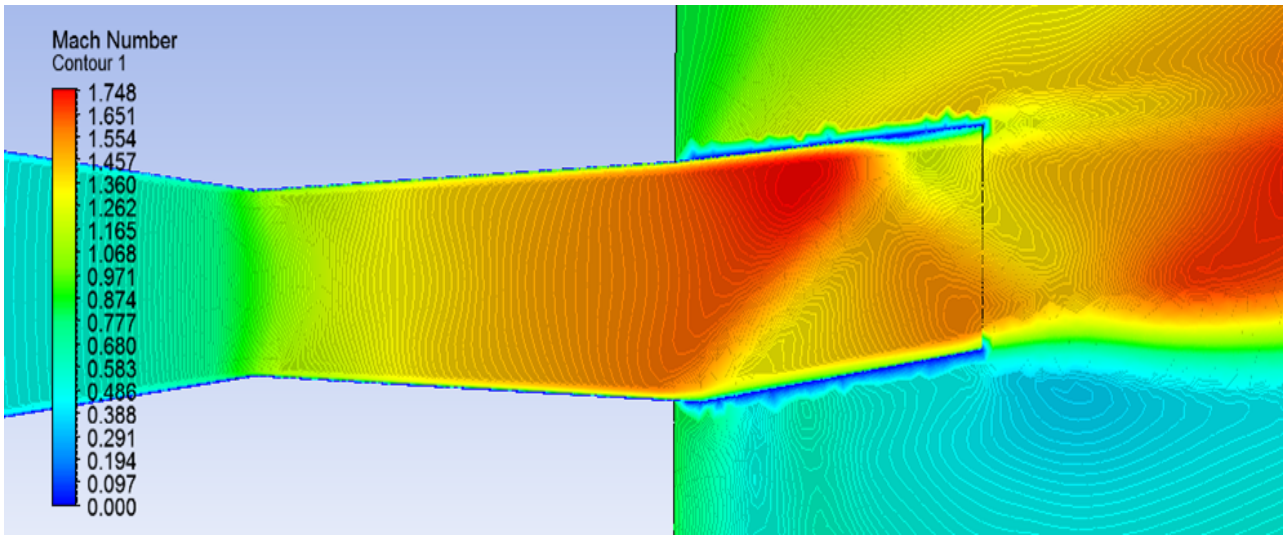

Figure 5.12: Shock formation inside the nozzle for NPR 5.0, Model 3 (NAR 1.21).

nozzle when an angle variation is added to the traditional CD nozzle can be observed between Figure 5.11 and Figure 5.12. When the two asymmetric geometry shapes are compared, the nozzle type NAR 1.21 has high Mach values at the divergent section of the nozzle, and no flow separation is experienced internally. At NPR 5.0, nozzle type NAR 1.21 generates shocks internally, which is not visible in the traditional CD nozzle or asymmetric type NAR 1.14. As presented in see Table 5.4. Further, among the Mach number values obtained for the asymmetric nozzle types, the asymmetric nozzle types displayed lower Mach number values in comparison to symmetric nozzle types at low NPRs.

Table 5.4: **Mach numbers for Models: NAR 1.5, NAR 1.66 at NPR 3.4 and NAR 1.14, NAR 1.21 at NPR 4.4**

NPR	Model 1a (NAR 1.5)	Model 1b (NAR 1.66)	Model 2 (NAR 1.14)	Model 3 (NAR 1.21)
3.4	1.8066	1.998	1.5767	1.7577
	Overexpanded flow	Overexpanded flow	Asymmetric separation	unknown

5.2.2 NAR 1.14 and NAR 1.21: High NPRs

During the second segment of the investigation, the asymmetric nozzle types, Model 2 (NAR 1.14) and Model 3 (NAR 1.21) were investigated under high NPRs (4.0 - 12.0). The two asymmetric models were tested for the highly *Underexpanded* condition and compared with the symmetric models. As described in Section 1.1, in Chapter 1, the divergent angle at the nozzle throat for both asymmetric models is set to 2.801 degrees while the modifying the contraction angles at the divergent walls downstream.

The Mach number values for NPR 5.5 - 12.0 are listed in Table 5.5. As described in Chapter 2, the nozzle type NAR 1.14 has a bigger contraction angle (29.64 degrees) in comparison to nozzle type NAR 1.21, where contraction angles of 15 and 8 degrees on the upper walls at the divergent section of the nozzle. The Mach number values for nozzle type, NAR 1.21 are lesser than of nozzle type NAR 1.14. However, relatively closer Mach number values to nozzle type NAR 1.14 can be achieved with a small contraction angle that of the nozzle type NAR 1.21.

Table 5.5: **Mach numbers for NAR 1.14 and NAR 1.21, at sea-level (1 atm) conditions.**

NPR	Model 2	Location of the shocks	Model 3	Location of the shocks
4.4	1.5015	*Overexpanded*	1.7331	Shocks at nozzle
5.5	1.5605	*Overexpanded*	1.7451	Shocks at nozzle
7.0	1.7593	*Overexpanded*	1.8760	Shocks at nozzle
10	2.1123	*Underexpanded*	2.0096	*Underexpanded*
12	2.3044	*Underexpanded*	2.0998	*Underexpanded*

With NAR being lower in both asymmetric models NAR: 1.14 and 1.21 in comparison to Model 1a and Model 1b, the Mach numbers for the high NPRs range shows an lower in Mach number value for NAR 1.21 and higher for NAR 1.14. These Mach number values can be compared to results of the symmetric models listed in Table 5.3. Shock formation at the jet plume region at highly *Underexpanded* condition for symmetric type, NAR 1.5 is compared with symmetric types NAR 1.14 and type NAR 1.21. The asymmetric nozzle type, NAR 1.21 generates different types of Mach shock configurations that of a traditional CD nozzle under highly *Underexpanded* conditions.

5.3 Contour Plots - Asymmetric models

5.3.1 Mach Contour plots for NAR 1.14 - high NPRs

Mach contours for the Model 2 (NAR 1.14) at high NPRs at NPR 5.5 - 12.0 is shown in Figure 5.13 to 5.14.

The shock waves become more enlarged as the nozzle pressure is increased (for a given distance in the jet plume region). As the NPR increases, the amount of Mach Diamonds formed within a given distance of the jet plume decreases. This could be due to the difference of the ambient pressure, free stream velocity over the nozzle and the nozzle NPR. The size of the Mach disks and the free jet boundary tend to increase with the increase of NPR see Figures 5.13 to 5.14.

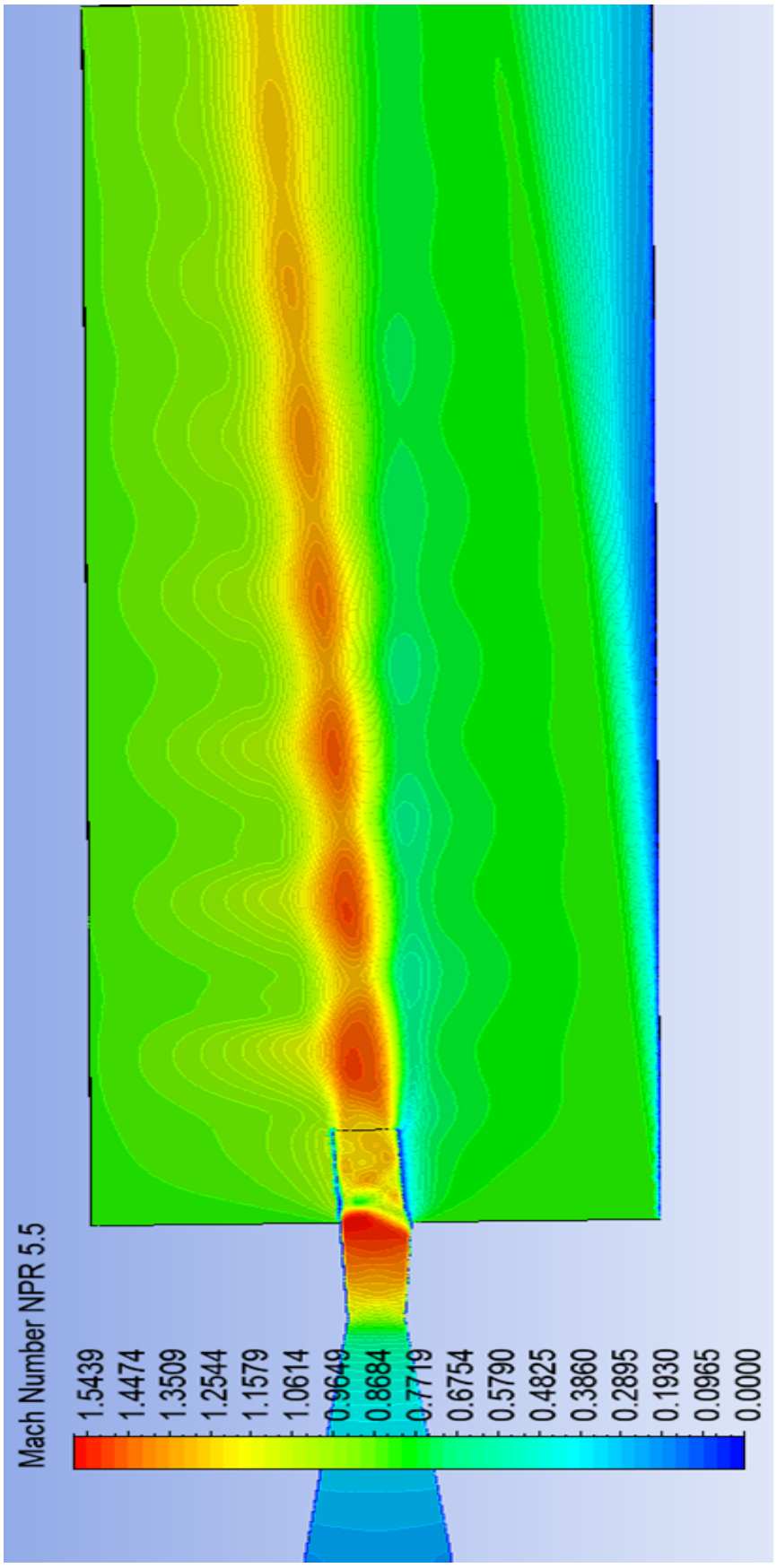

Figure 5.13: Mach number contours for Model 2 (NAR 1.14) at NPR 5.5.

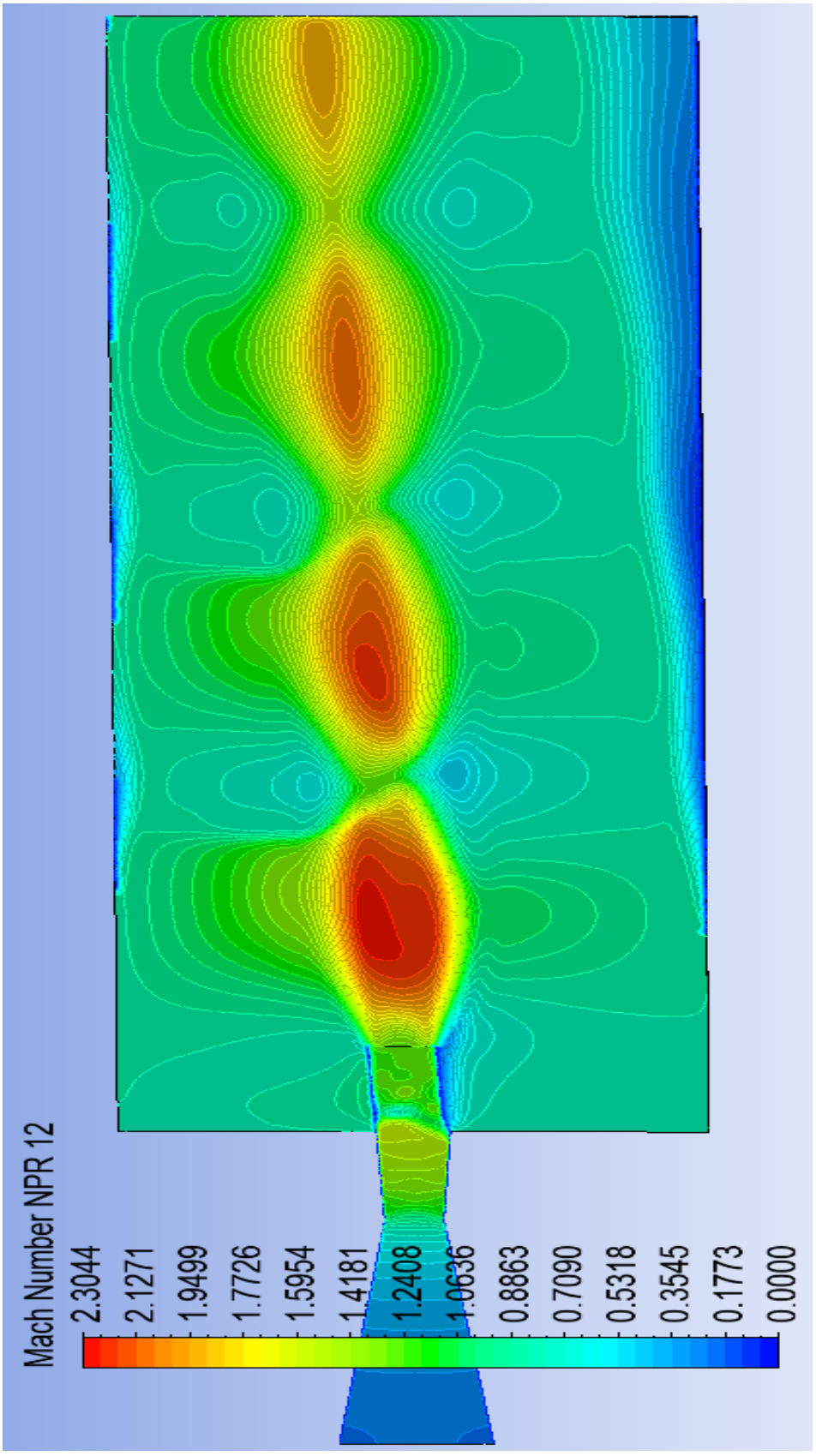

Figure 5.14: Mach number contours for Model 2 (NAR 1.14) at NPR 12.0.

5.3.2 Mach Contour plots for NAR 1.21 - high NPRs

Mach contours for the nozzle type NAR 1.21 at high NPRs are shown in Figure 5.15 to 5.16.

In comparison to nozzle type NAR 1.14, significant differences can be seen internally and downstream of the nozzle of the nozzle type NAR 1.21. Since the angle variation is added to both top and bottom walls of the nozzle, the exhaust flow at the exit of the nozzle deflects away from the axial line. All models decrease the number of Mach Shocks Diamonds per given distance as the NPR increases. The shape of the Mach Shock Diamonds in nozzle type, NAR 1.21 is different compared to the other three Models NAR 1.5, NAR 1.66 and NAR 1.14.

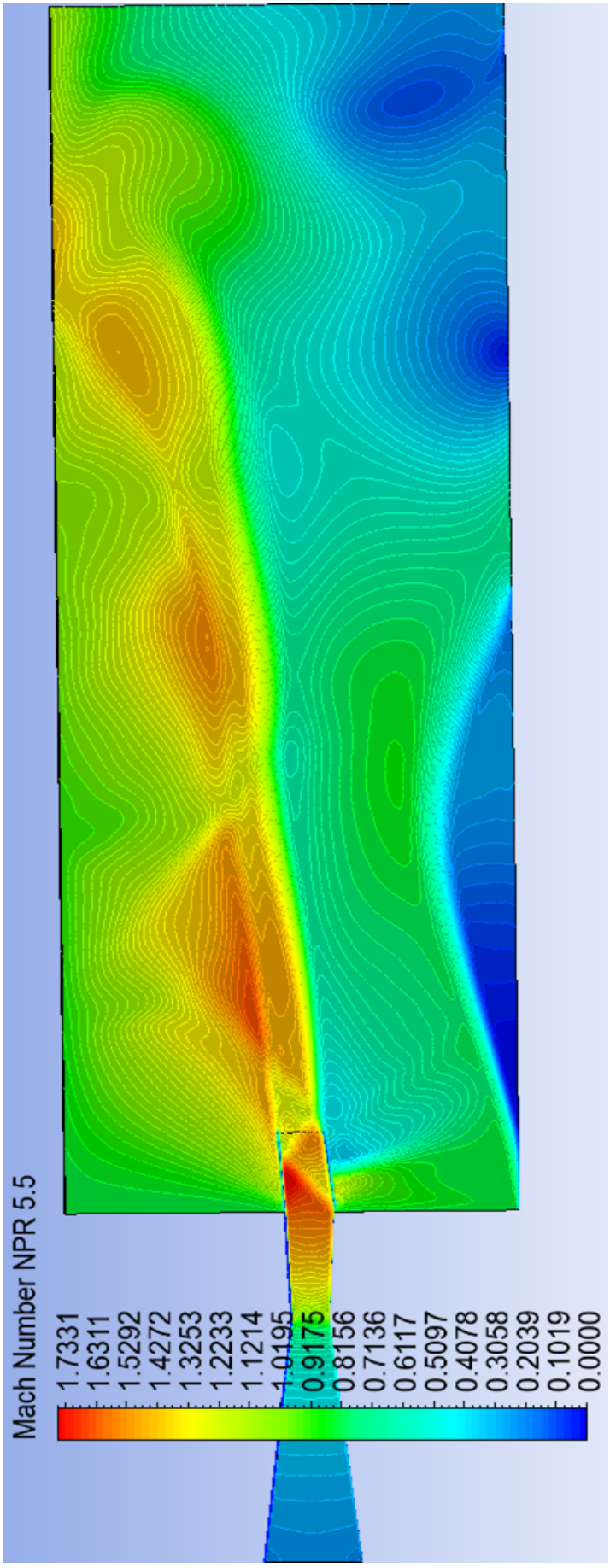

Figure 5.15: Mach number contours for Model 3 (NAR 1.21) at NPR 5.5.

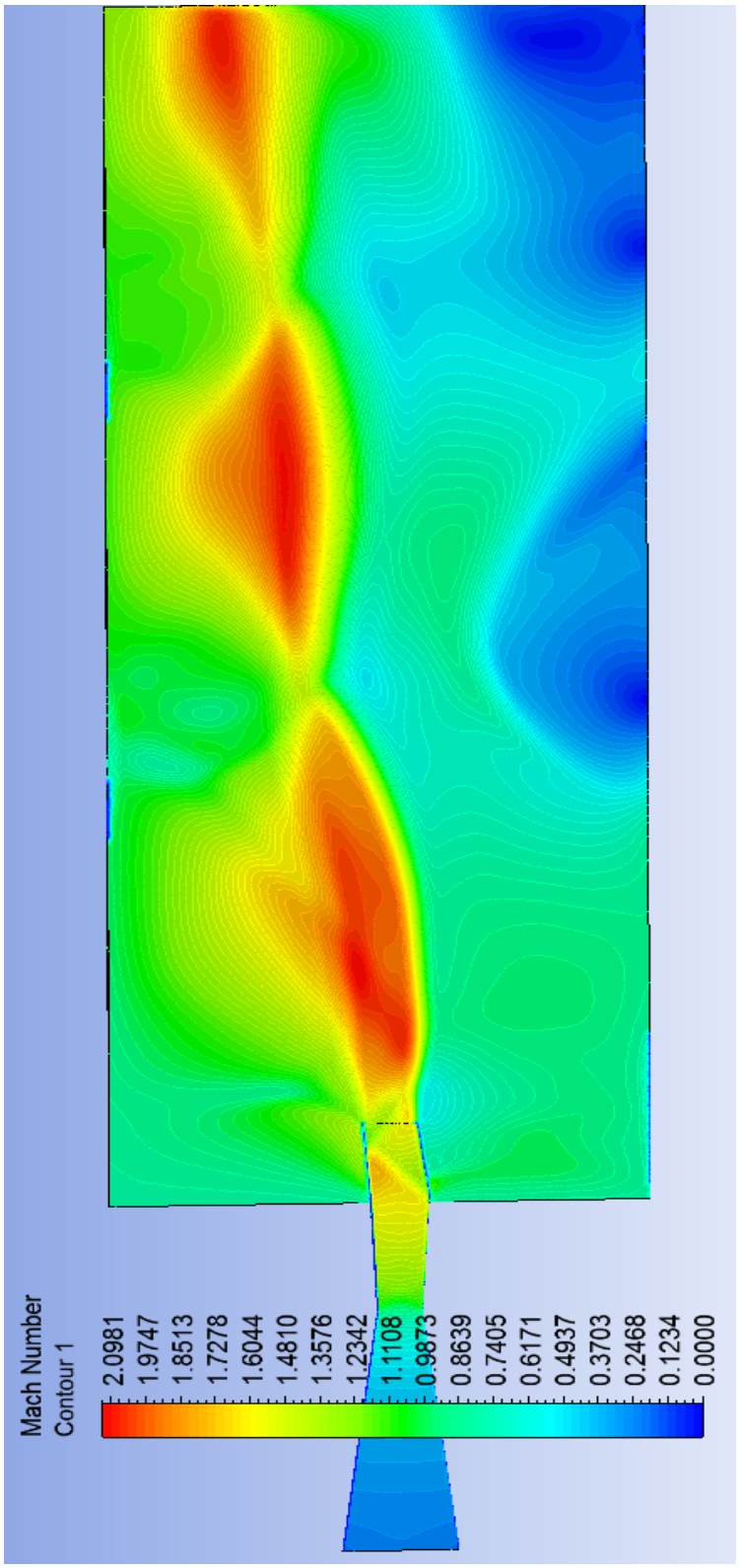

Figure 5.16: Mach number contours for Model 3 (NAR 1.21) at NPR 12.0.

5.3.3 Density Contours for NAR 1.14 and NAR 1.21

Density contours for asymmetric models, NAR 1.14 and NAR 1.21 for *Underexpanded* condition at NPR 10.0 is shown in Figure 5.17.

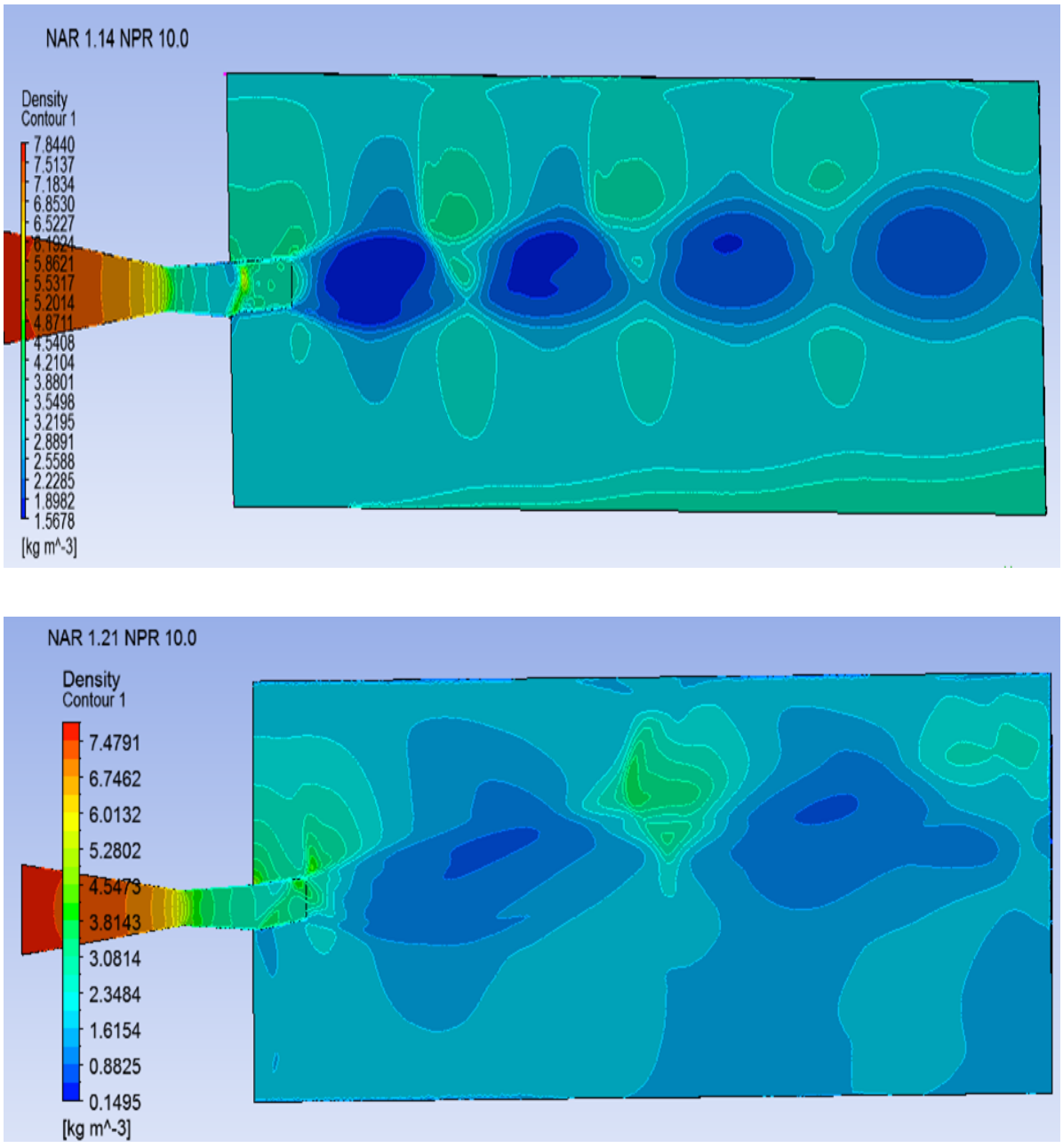

Figure 5.17: Density contours : NAR 1.14 (top) and NAR 1.21 (bottom) at NPR 10.0

5.3.4 TKE Contours for NAR 1.14 and NAR 1.21

The relevant TKE energies for the jet plume regions are displayed in, Figures 5.18. These figures compare the energy dissipation in two asymmetric models: Model 2 (NAR 1.14) and

Model 3 (NAR 1.21) at NPR 12.0 to analyze the amount of energy dissipation and the location of dissipation. TKE (production, transport and dissipation) which can be produced by fluid shear, friction and is transferred down the turbulence energy cascade, is dissipated by viscous forces at the Kolmogorov scale [11]. As shown in nozzle type NAR 1.21, the kinetic energy build-up and spreads on a bigger region along bottom of the jet plume channel.

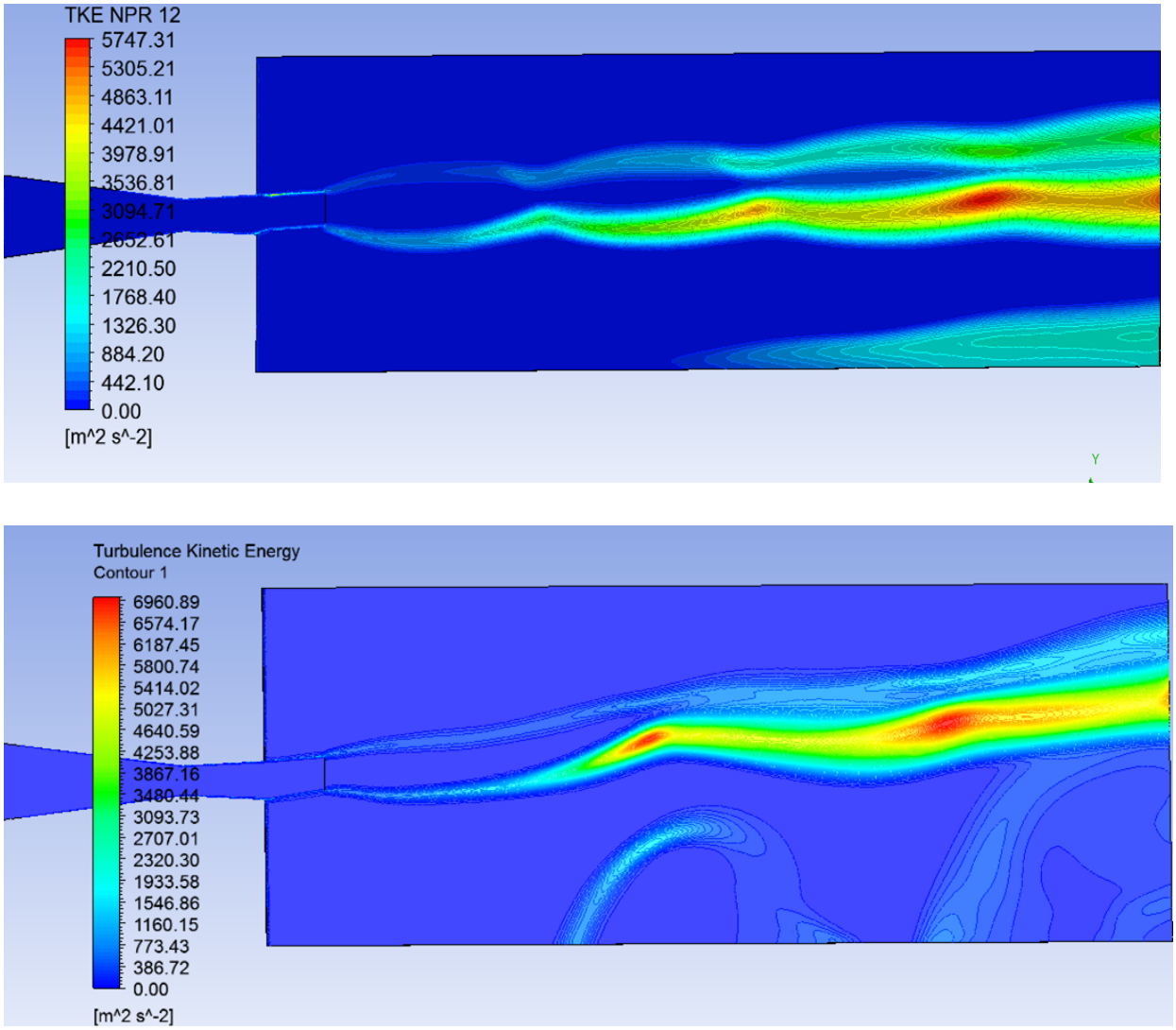

Figure 5.18: TKE contours : NAR 1.14 (top) and NAR 1.21 (bottom) at NPR 12.0

5.4 Contour Plots: NAR 1.5, NAR 1.14 and NAR 1.21 - low NPRs

5.4.1 Mach Contours - across horizontal nozzle length

The effects of the Mach number (see Figures 5.19, 5.20 and 5.21) for the three models : symmetric Model 1a (NAR 1.5), asymmetric Model 2 (NAR 1.14) and Model 3 (NAR 1.21), subjected to low NPR is plotted as having same divergent angle of 2.801 degrees at the throat. The Mach contour variations plots for NPR 3.4 are shown in Figures 5.19, 5.20 and 5.21.

Contour lines across the vertical height along the divergent cross-section of the nozzle is plotted to observe the variation Mach values under low NPRs. These contour lines starting at the bottom wall from 0.25 mm to the top wall at 22.85 mm, through inlet of the convergent to the divergent outlet of the nozzle. The separation location occurs at a shorter distance from the throat in NAR 1.14 compared to NAR 1.5 and NAR 1.21 for the given NPR 4.4. Since the value of the Mach number for the given NPR is lower in two asymmetric models than of the symmetric type NAR 1.5, the Mach number drop close to zero in NAR 1.14 and NAR 1.21 at the vicinity of the bottom wall, across the separation zone.

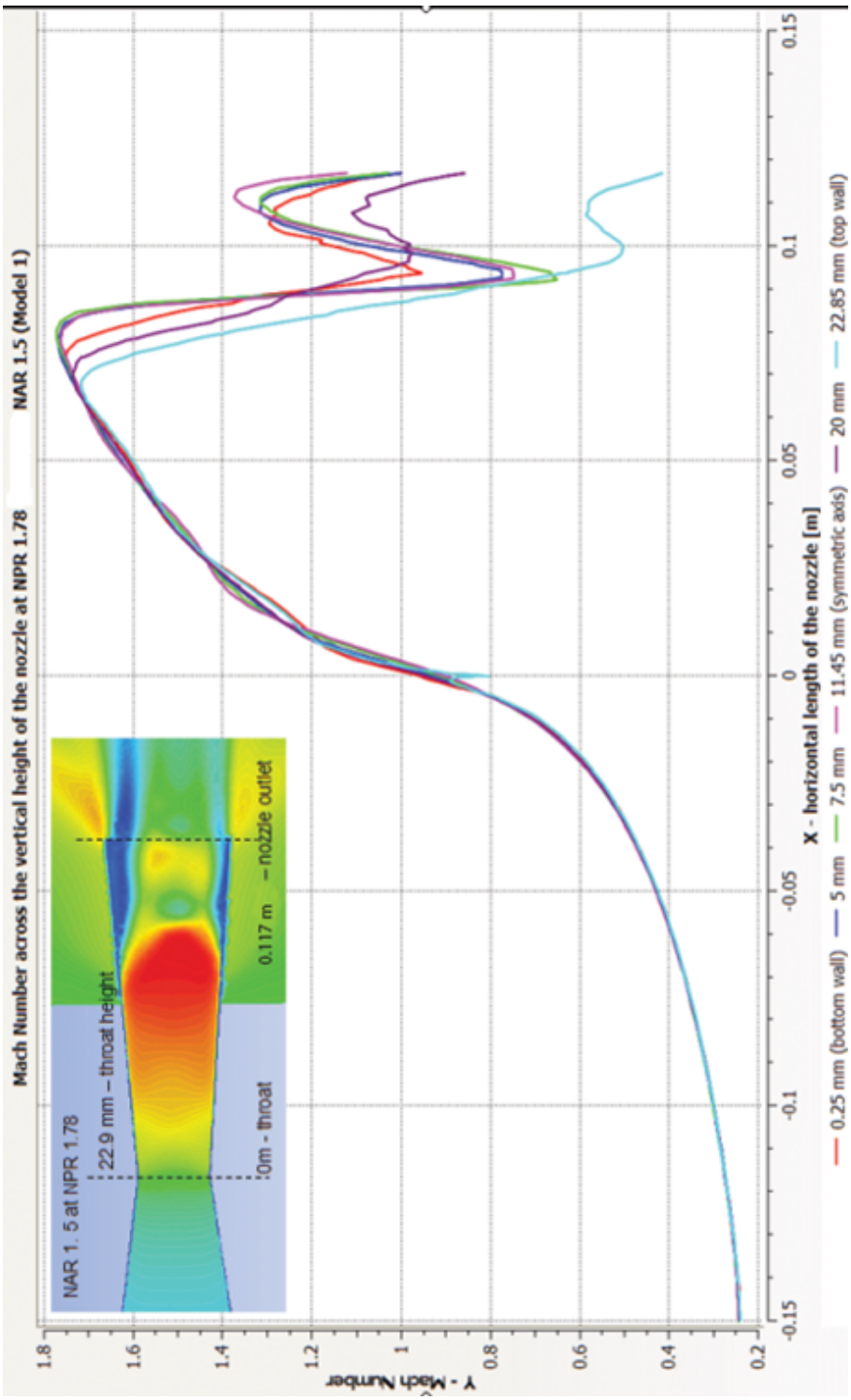

Figure 5.19: Mach number across the total horizontal nozzle length for Model 1a (NAR 1.5) at NPR 1.78.

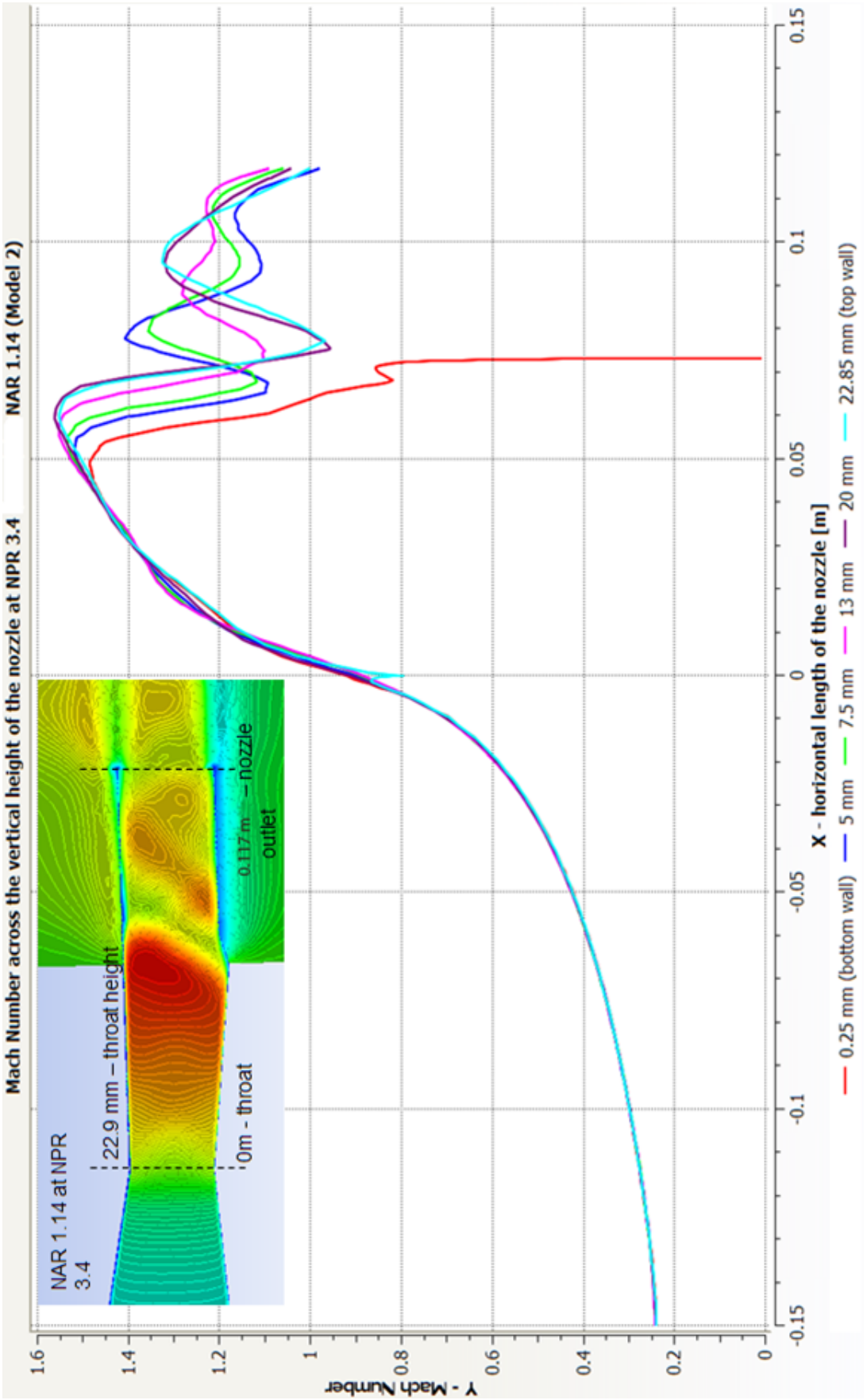

Figure 5.20: Mach number across the total horizontal nozzle length for Model 2 (NAR 1.14) at NPR 4.4.

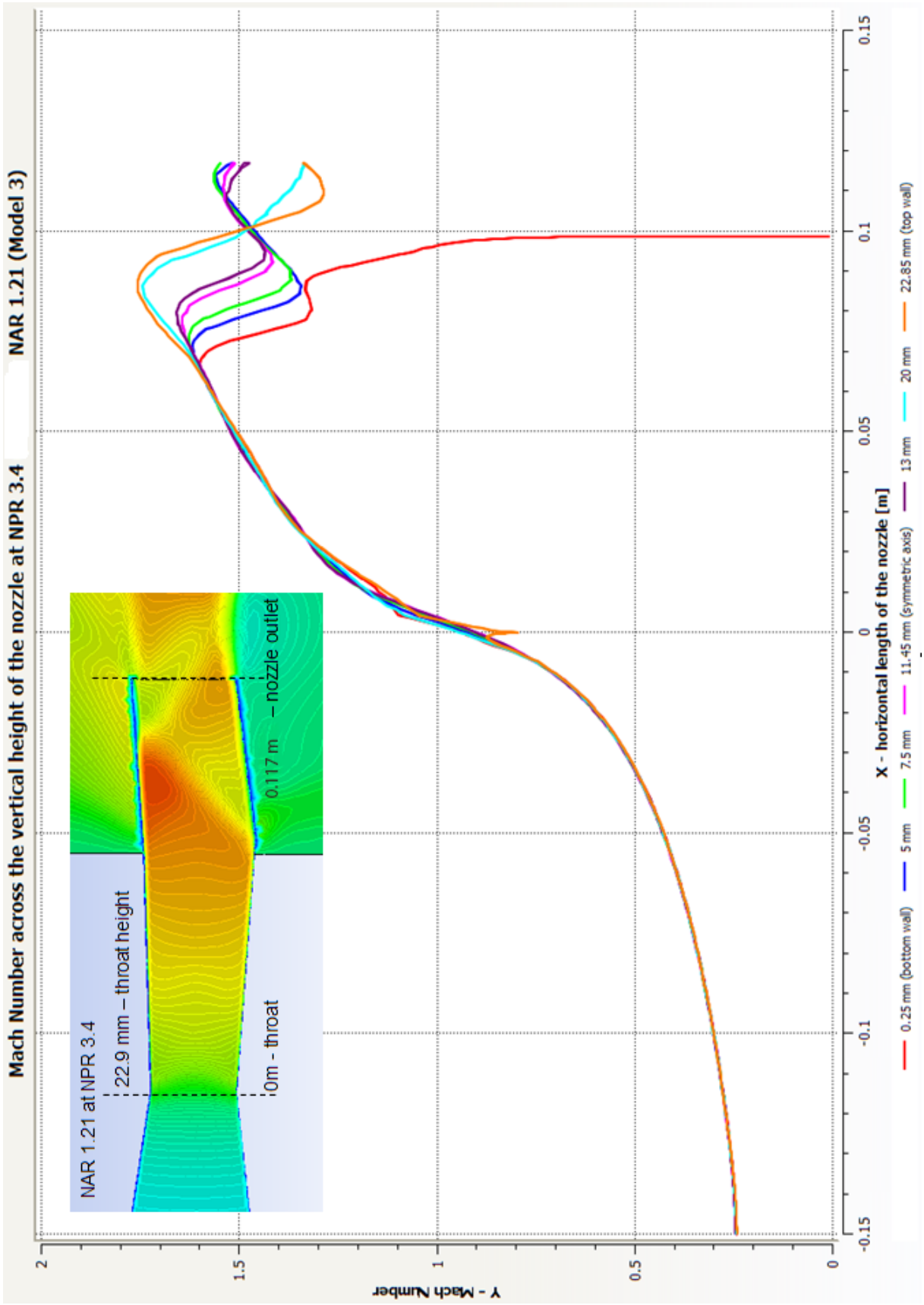

Figure 5.21: Mach number across the total horizontal nozzle length for Model 3(NAR 1.21) at NPR 4.4.

5.4.2 Pressure Contours - across horizontal nozzle length

The effect of pressure (see Figures 5.22, 5.23 and 5.24) for the three models : symmetric Model 1a (NAR 1.5), asymmetric Model 2 (NAR 1.14) and Model 3 (NAR 1.21), subjected to low NPR is plotted as having the same divergent angle of 2.801 degrees at the throat.

The contour plots for NPR 3.4 for pressure variations are shown in Figures 5.22, 5.23 and 5.24.

The plots shown in Figures 5.22, 5.23, 5.24 are for pressure contour variations for NPR 3.4. Contour lines across the vertical height along the divergent cross section of the nozzle is plotted to observe the variation pressure variations under low NPRs. These contour lines start at the bottom wall from 0.25 mm to the top wall at 22.85 mm, through inlet of the convergent to the divergent outlet of the nozzle. Since the pressure drop for the given NPR is higher across the shock and separation in the asymmetric nozzle type NAR 1.21, compared with types NAR 1.5 and NAR 1.14. The pressure re-gains after the separation and shocks for type NAR 1.14 is higher. Pressure re-gains near the bottom wall for Model 3 (NAR 1.21) before dropping down again at the second shock at the divergent exit.

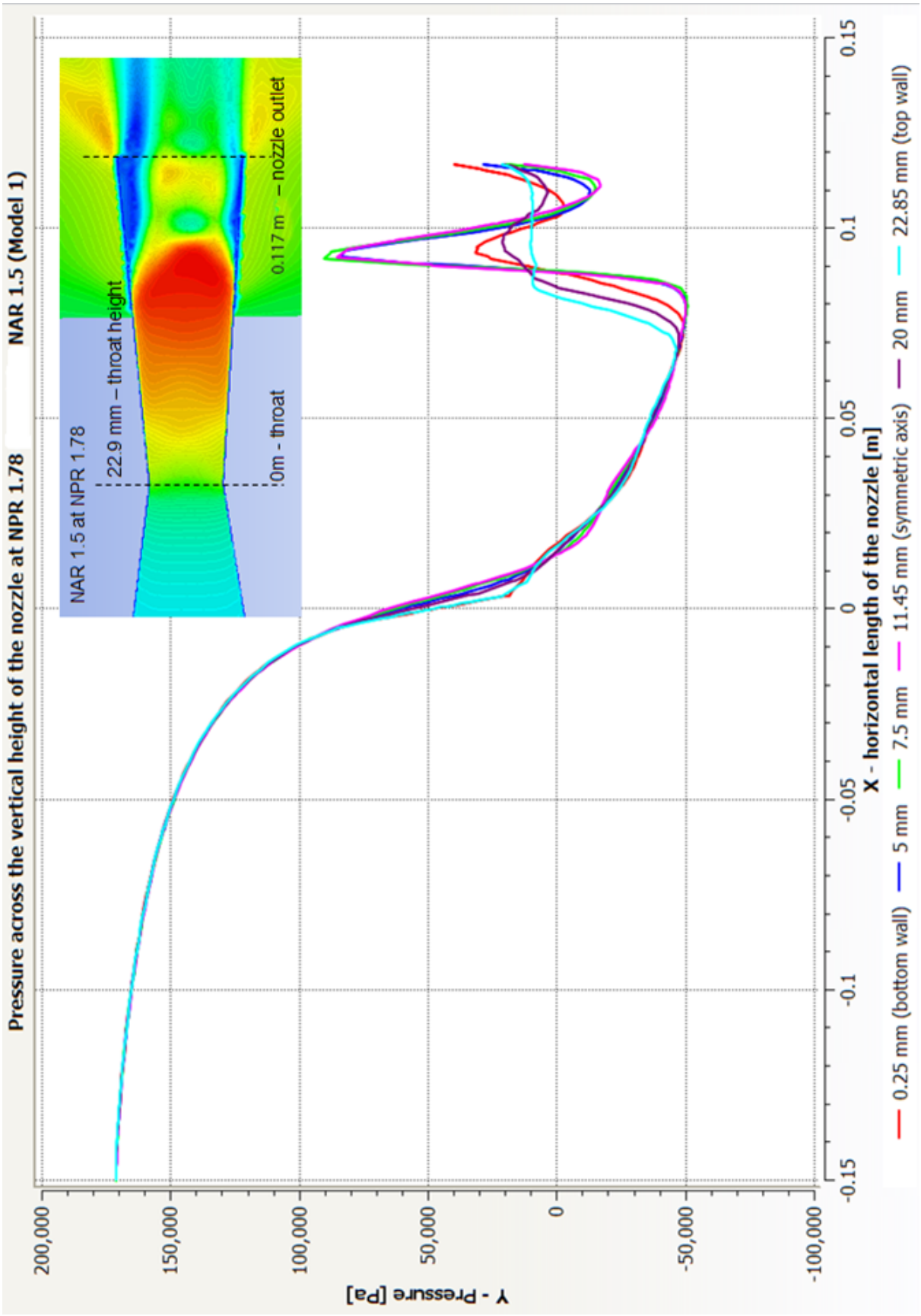

Figure 5.22: Pressure distribution across the total horizontal nozzle for Model 1a (NAR 1.5) at NPR 1.78.

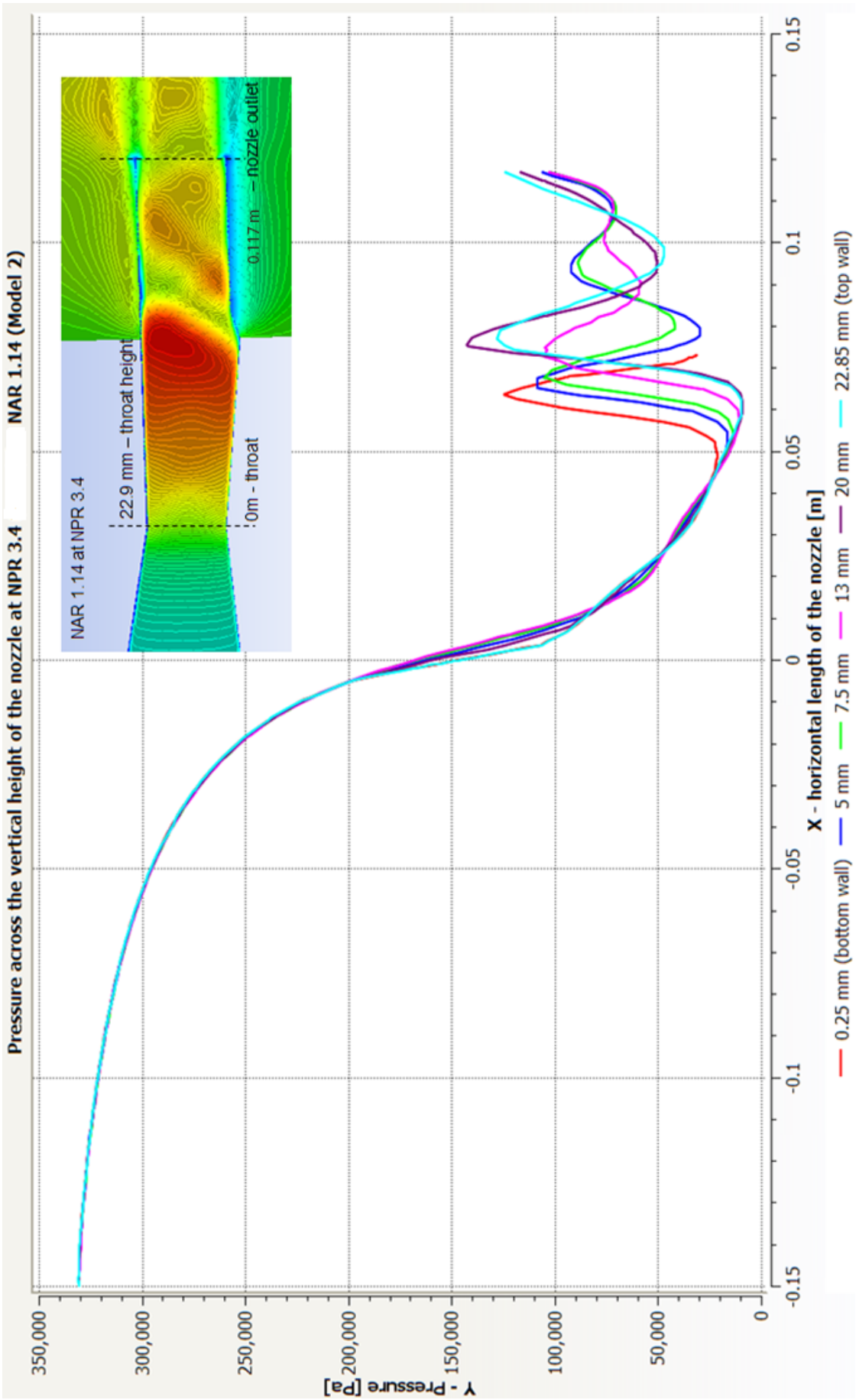

Figure 5.23: Pressure distribution across the total horizontal nozzle for Model 2 (NAR 1.14) at NPR 4.4.

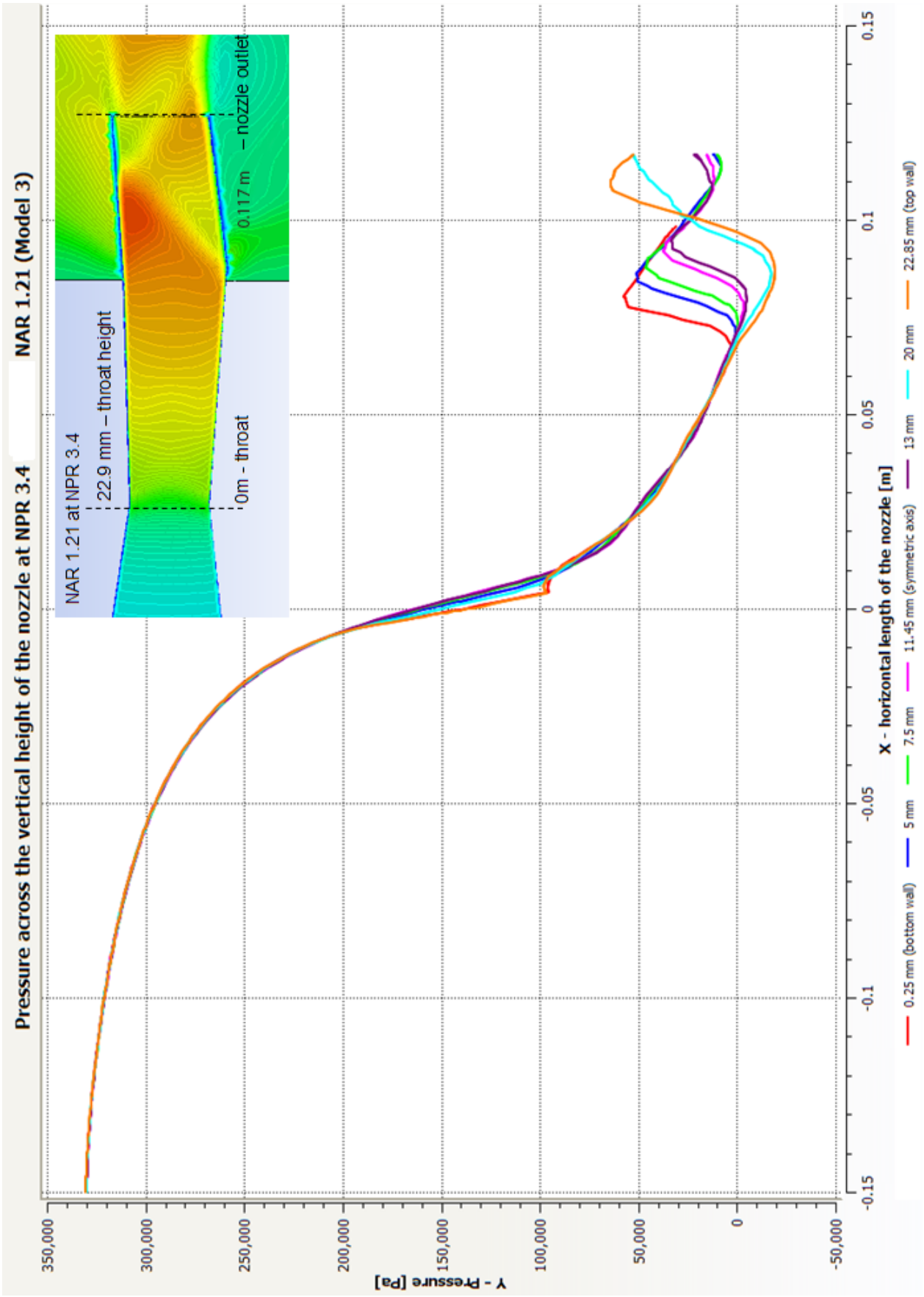

Figure 5.24: Pressure distribution across the total horizontal nozzle for Model 3 (NAR 1.21) at NPR 4.4.

5.4.3 TKE Contours - across horizontal nozzle length

The effect of the Turbulent kinetic energy (TKE) (see Figure 5.25, 5.26 and 5.25) for the three models : symmetric Model 1a (NAR 1.5), asymmetric Model 2 (NAR 1.14) and Model 3 (NAR 1.21), subjected to low NPR is plotted as having same divergent angle of 2.801 degrees at the throat.

The plots shown in Figures 5.22, 5.23, 5.24 are for TKE dissipations for NPR 3.4 for symmetric type and NPR 5.5 for asymmetric types. Contour lines across the vertical height along the divergent cross-section of the nozzle are plotted to observe the energy dissipation (negative rate of change in kinetic energy) under low NPRs. These contour lines start at the bottom wall from 0.25 mm to the top wall at 22.85 mm, through inlet of the convergent to the divergent outlet of the nozzle.

A significant variance is observed in TKE dissipation within the three models. For the given NPR, higher dissipation is visible on the top walls for NAR 1.14 and NAR 1.21, and on the bottom wall in NAR 1.5. Physically, energy is dissipated because of the work done by the fluctuating viscous stresses in resisting deformation of the fluid material by the fluctuating strain rates [11].

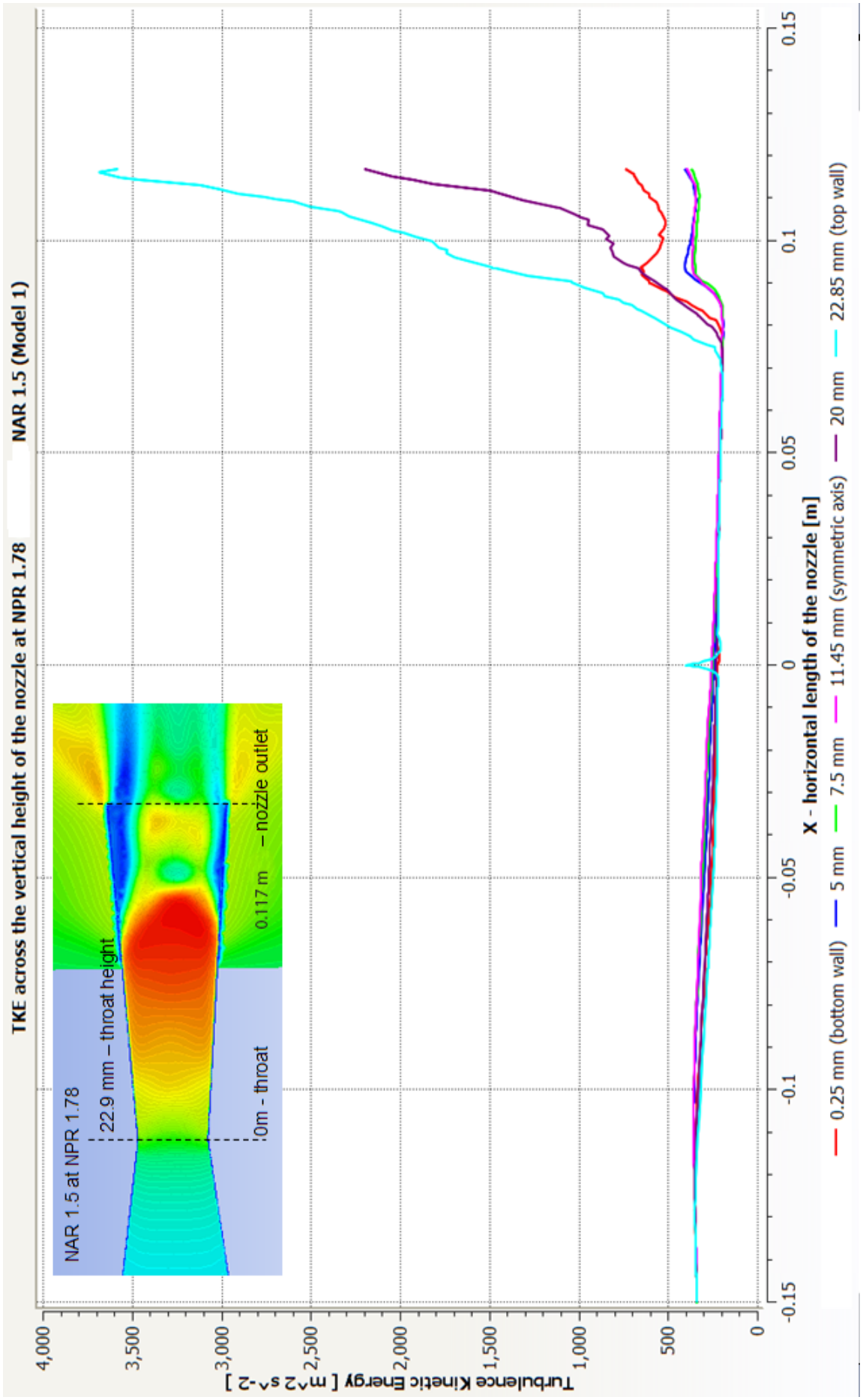

Figure 5.25: TKE distribution across the total horizontal nozzle for Model 1a (NAR 1.5) at NPR 1.78.

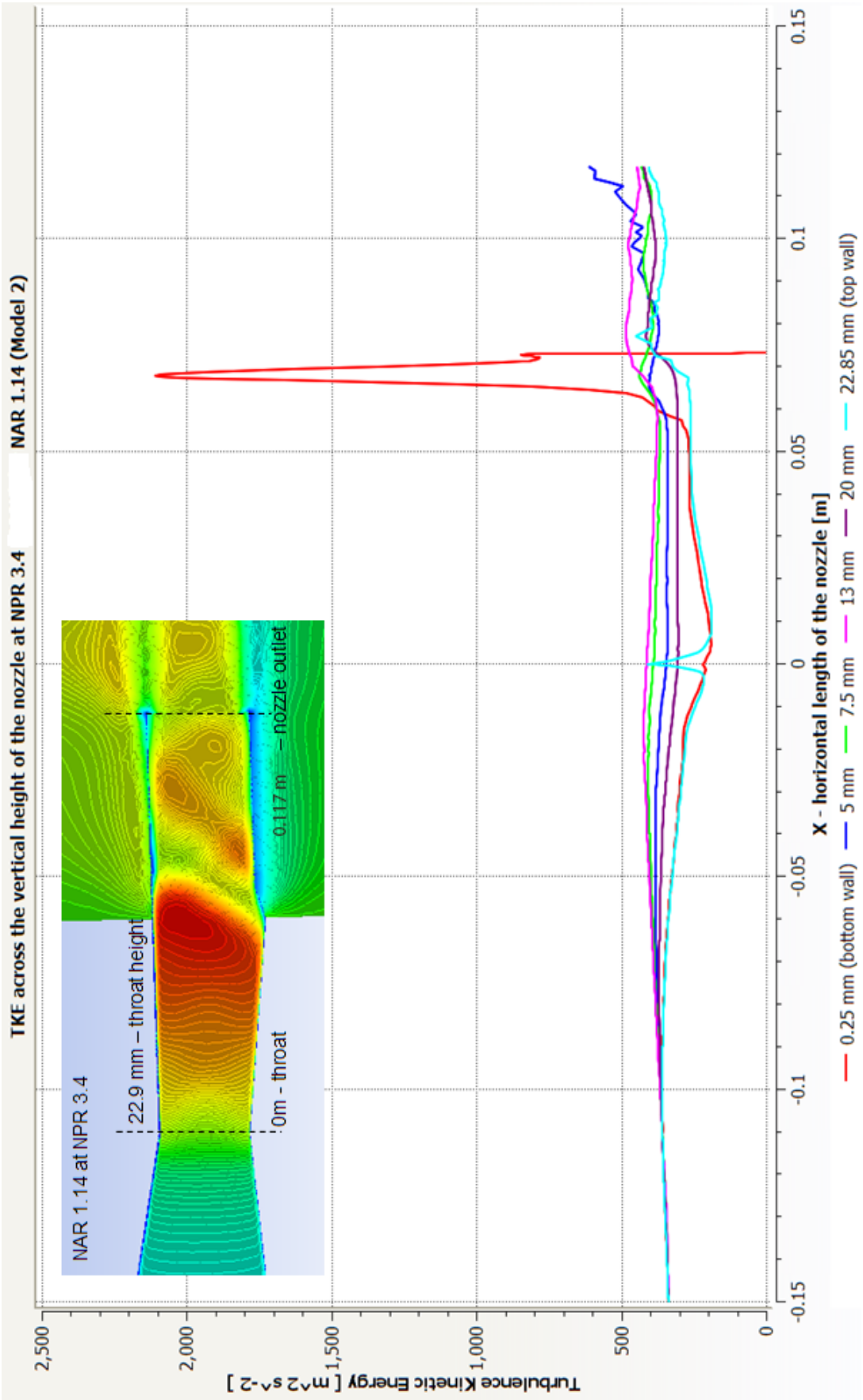

Figure 5.26: TKE distribution across the total horizontal nozzle for Model 2 (NAR 1.14) at NPR 5.5.

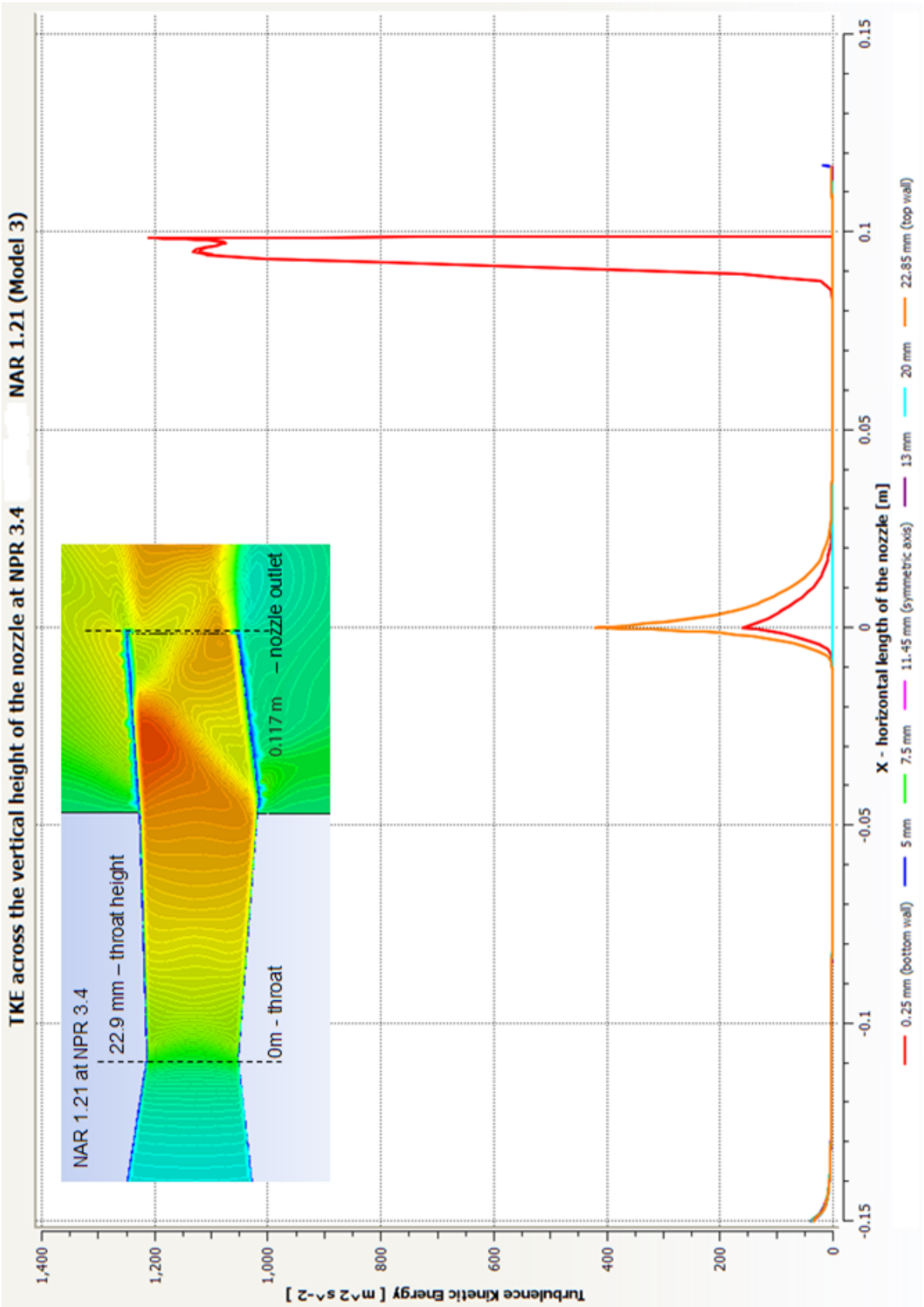

Figure 5.27: TKE distribution across the total horizontal nozzle for Model 3 (NAR 1.21) at NPR 5.5.

5.5 Steering Thrust and Deflection Angle - Asymmetric Models

The jet deflection is an important factor used in nozzle flow analysis, since the angle of deflection of the flow significantly contribute towards the device's direction of motion. Since the introduction of the contraction angles to the divergent section of the symmetric nozzle, it was the prime interest of this projet to observe the influence of the contraction angles towards to jet deflection. The steering thrust (kN) and plume jet deflection (degrees) at the exit of the divergent section was calculated for NPR 5.5 and NPR 10.0.

The Mach contour plots obtained for the highly *Underexpanded* condition, displayed these mach shocks been diverted away from the center axial line. Varying the divergent section of the nozzle and with the influence of the increasing NPR, we observed the increase of the vectored flow path in respect tot he axial line. In comparison with the nozzle type NAR 1.21, the Mach contour values are slightly less than of type NAR 1.14, see Table 5.6. The flow is significantly offset in the desired direction and is considerably different from the traditional Mach Diamond shock patterns. The steering thrust calculations used for nozzle type NAR 1.14 and NAR 1.21

Table 5.6: **Steering Thrust comparison for asymmetric models: Geometrical configuration of F/A-18 [13] with nozzle types NAR 1.14 and NAR 1.21.**

Model type	Mach No	NPR	Force (kN)	Jet deflection angle (degrees
F/A-18 [13]	N/A	2.0	63.92	20.607
F/A-18 [13]	N/A	6.0	65.50	15.821
Model 2 (NAR 1.14)	1.5706	5.5	30.69	11.05
Model 3 (NAR 1.21)	1.7585	5.5	38.32	10.85
Model 2 (NAR 1.14)	2.1998	10.0	82.25	16.33
Model 3 (NAR 1.21)	2.3044	10.0	79.96	14.48

are presented in Section 4.5 in Chapter 4. The deflection jet angle has similar values for both Models for NPR 12, while the NPR 5.5 of NAR 1.14 has higher deflection angles compared to NAR 1.21. In NAR 1.21 with a smaller divergent variation (8 degrees bottom wall) similar deflections were achieved.

The results listed in Table 5.6 closely measure with the experimental and computation re-

sults obtained for jet deflection angles [13]. The studies conducted for the F/A-18 configuration vehicle with deflection vanes [13] closely measure with results investigated during this research.

In comparison to geometrical configuration of F/A-18 with deflection vanes studied [13], for jet deflection turning angles (exhaust plume turning effectiveness), the asymmetric nozzle geometrical configuration in this study have performed with lower contraction angles (divergent section) offering similar plume deflection angles. It was noticed the NPRs of this study in comparison to geometrical configuration of F/A-18 with deflection vanes was lower for a given NPR.

Some results obtained from the ground based investigation carried out for geometrical configuration F/A-18 symmetric configuration vehicle, in comparison to simulation results obtained for nozzle types NAR 1.14 and NAR 1.21 at NPR 5.5 and NPR 10.0.

Chapter 6

Conclusion

6.1 Summary of the Research

6.1.1 Contributions to the Original Work

This research focused on making modifications to the design of the nozzle (divergent section) that improved the performance characteristics of the convergent divergent (CD) nozzle. Through this research, the asymmetry introduced to the conservative CD model at the divergent section of the nozzle is novel and expands on existing investigations related to nozzle flow analysis.

The modifications of the design of the device is mainly focused on the two asymmetric models, where the contraction angles was added to the divergent section at the nozzle walls. The asymmetry introduced to nozzle type, NAR 1.14 with two contraction angles at the bottom wall and the nozzle type, NAR 1.21 with two contraction angle variations to both top and bottom walls, while retaining the same divergent angle at the throat of all nozzle cases. The asymmetry introduced to the divergent section of the nozzle is original to previously conducted numerical and experimental studies carried out in this area to the best of the authors knowledge.

Some additional parameters (initial and boundary conditions) were introduced to the model, at the simulation stage of the project contributing to the original work. These parameters (initial and boundary conditions) accommodated the effects around the nozzle such as the free stream velocity which passes around the nozzle to visualise the free stream fluid immersing with the Mach shock Diamonds emerging at the exit of the nozzle and shock interaction with the external atmospheric. The numerical parameter set-up on previous studies do not

accommodate this effect of external flow speeds on the flow down stream specially on the jet plume regions. Further, the nozzle was tested under high NPRs, to understand the shocks patterns (jet plume region) when the exiting internal flows (at the end of the divergent section) are immersed with the free stream flows at supersonic speeds.

The nozzles internal flow phenomenons, *Lambda* shocks and Shock Induced Flow Separation (SIFS) were compared using variables such as Mach number, pressure and turbulent kinetic energy variations between the asymmetric models and traditional symmetric model under low NPRs.

Further the jet plume shock patters and jet plume deflections and thrust at the nozzle exit were compared with the asymmetric models. The impact of introducing contraction angles to divergent sections of the nozzle on the jet plume region was also investigated.

6.1.2 Research Achievements

This research demonstrated that, varying the divergent section of the nozzle results in an increase in the Mach number which influence the thrust generated at the nozzle outlet. Further, this study also verifies the significance of the geometry variation towards the deflection angle of the jet flow.

Nozzle under Low NPRs

Corresponding to the nozzle performance with geometry variation (asymmetry model type NAR 1.21) added to both top and bottom walls, no internal boundary layer separation was observed. Under low NPRs, separation bubbles (zones) were generated due to increase in adverse pressure gradients creating reverse flow effects.

This phenomena of flow separation is likely to be observed in a traditional convergent divergent nozzle under low NPRs; however, was not visible for the geometry of the asymmetric model with contraction angles introduced to both walls in nozzle type, NAR 1.21. Hence, internal shock formation in asymmetric nozzles produces a different flow patterns inside the divergent section of the nozzle to that produced by the traditional convergent divergent nozzle under low NPRs. Lowest internal Mach number values at asymmetric type, NAR 1.21 is observed among the remaining model types, where no internal separation along the nozzle walls is seen.

Nozzle under High NPRs

The net steering force of the nozzle with geometry variation (asymmetry type NAR 1.21) to both top and bottom walls at higher NPRs was lesser than that of the nozzle with geometry variation (asymmetry type NAR 1.14) to the bottom wall only. However, the jet plume deflection angles of both asymmetric nozzles produced closely similar angles same at high NPRs. The nozzle type, NAR 1.14 with a relatively small contraction angle produced in higher exhaust speeds and deflection angles compared to nozzle type NAR 1.14 for highly *Underexpanded* condition.

The introduction of the contraction angles to the divergent section of the nozzle is unique and has demonstrated some distinct results which were previously not investigated under high NPRs. These results including Mach Diamond shock patterns at the jet plume region previously unseen for higher NPRs.

6.1.3 Significance of the Achievement

We can modify the divergent section of the nozzle by adding a small contraction angle to the walls, and this can significantly improve the net thrust produced at the outlet of the nozzle and the direction of the flow path.

The flow is significantly offset in the desired direction and is considerably different from the Mach Diamond shock patterns observed at traditional CD nozzles.

Further, modifications added to the divergent section of the nozzle could be implemented to enhance other possible flow phenomena. These modifications would increase the thrust and flow path directions, while impeding flow phenomenons such as Shock Induced Boundary Layer Separations (SIBLS) at the boundary layer, thus reducing the fluctuating pressure loads acting on the walls.

6.2 Further Work

A possible suggestion for future is the application of future high speed nozzles, such as nozzles used in supersonic missiles. The geometry variation added on both top and bottom walls may enhance the exhausting gas to vector the net thrust in desired parabolic trajectories.

The geometry variation added in asymmetric type, NAR 1.21 could be implemented to

direct the exhaust flow to the desired path in a jet nozzle during sharp turns.

Since no flow separation was observed at low NPRs on the asymmetric type, NAR 1.21, where the contraction angels introduced to both top and bottom walls, this asymmetric geometry type could be further studies numerically and experientially to reduce further internal Shock Induced Flow Separations (SIFL) in internal nozzle flows.

The possibility of alternating the jet flow up or down wards at higher NPR could be tested. Such vectoring added to the trajectory could be implemented in long range weapon vehicles or other form of high speed nozzles.

Testing with further variations in the divergent sections, may improve the jet plume deflection capabilities in future supersonic nozzle devices.

Chapter 7

Appendix I

Y plus plots along nozzle walls for NAR 1.5, NAR1.66, NAR 1.14 and NAR 1.21

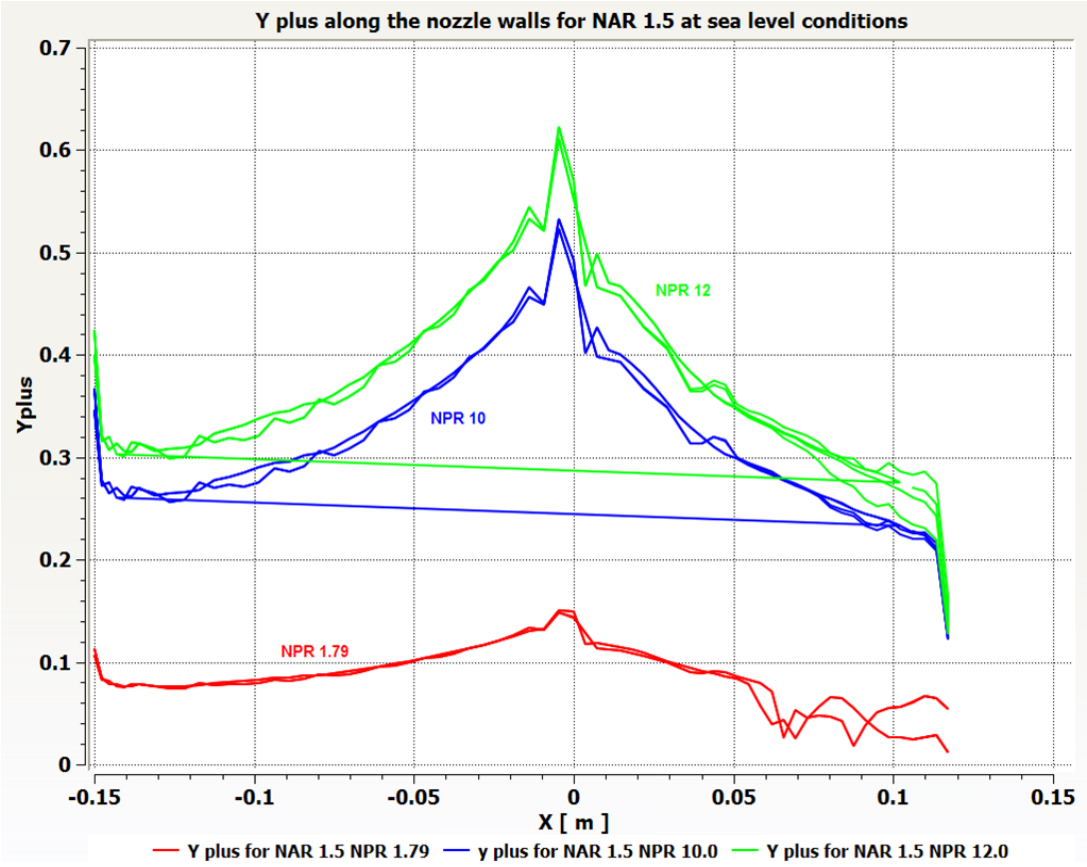

Figure 7.1: Y plus values along the nozzle walls of **NAR 1.5**, NPR 1.79, 10, 12.

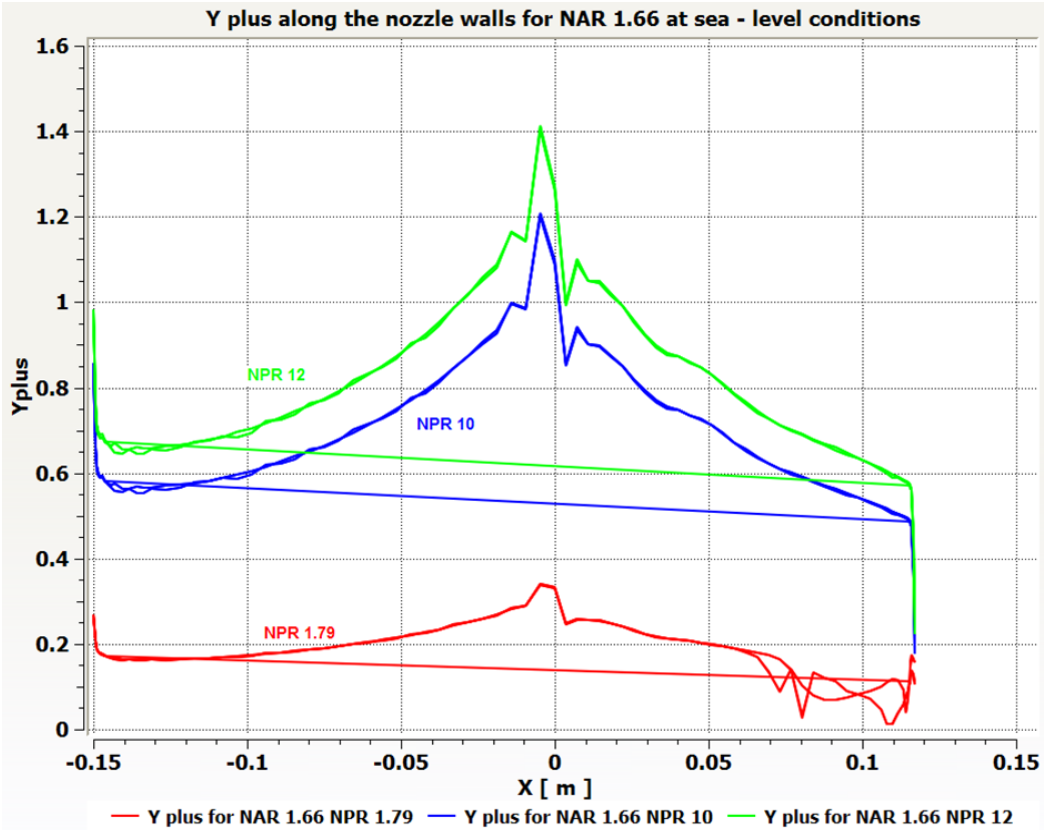

Figure 7.2: Y plus values along the nozzle walls of **NAR 1.66**, NPR 1.79, 10.

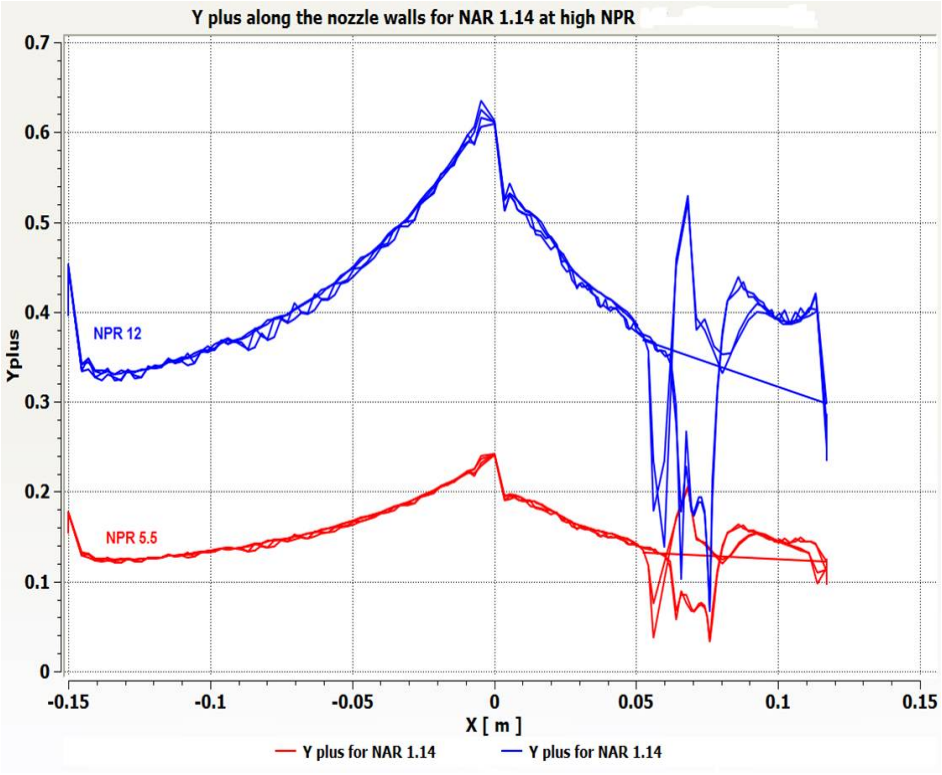

Figure 7.3: Y plus values along the nozzle walls of **NAR 1.14**, NPR 5.5, 12.

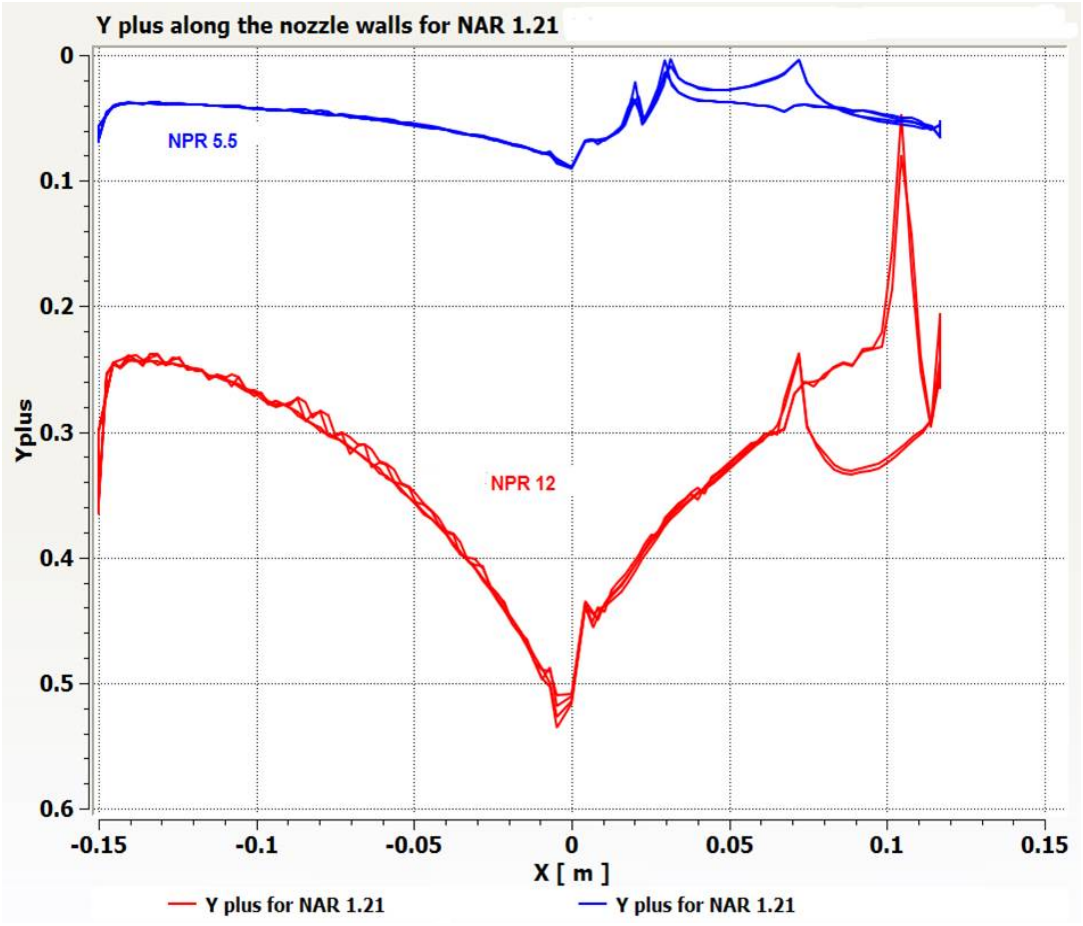

Figure 7.4: Y plus values along the nozzle walls of **NAR 1.21**, NPR 5.5 and 12.

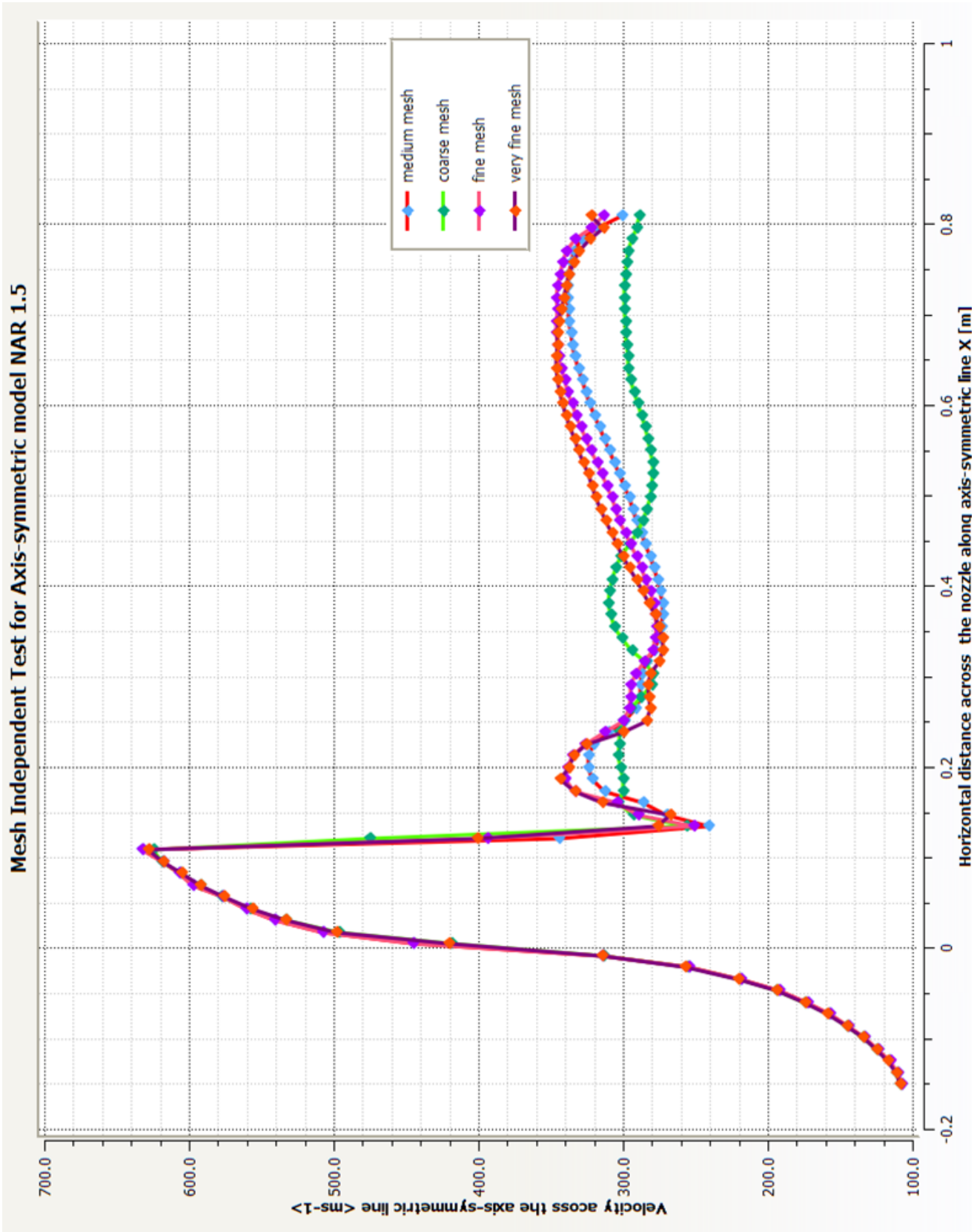

Figure 7.5: Mesh Independent Test for Axis-symmetric model, NAR 1.5

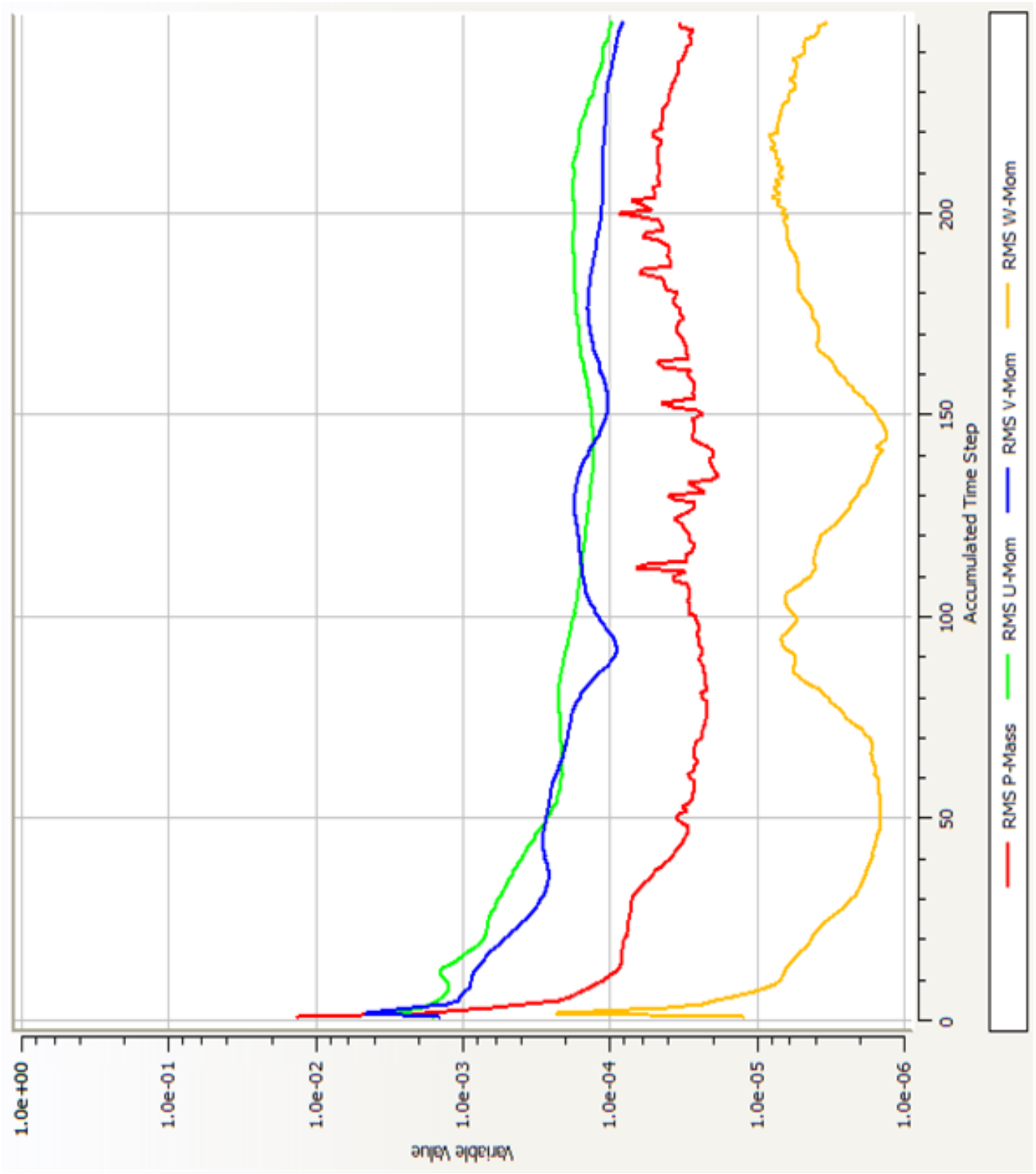

Figure 7.6: Residual Convergence history for Axis-symmetric model (coarse mesh), NAR 1.5

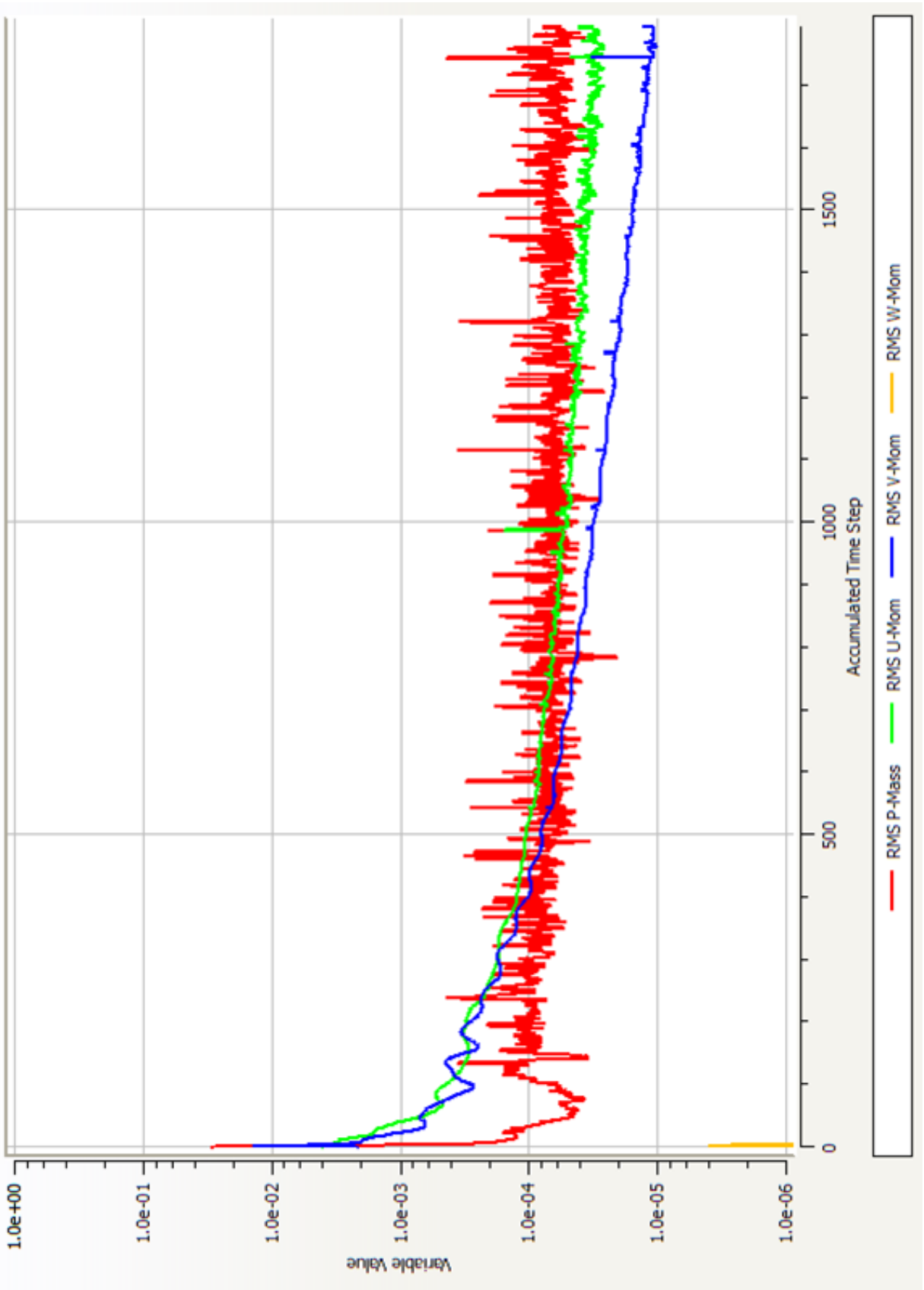

Figure 7.7: Residual Convergence history for Axis-symmetric model (medium mesh), NAR 1.5

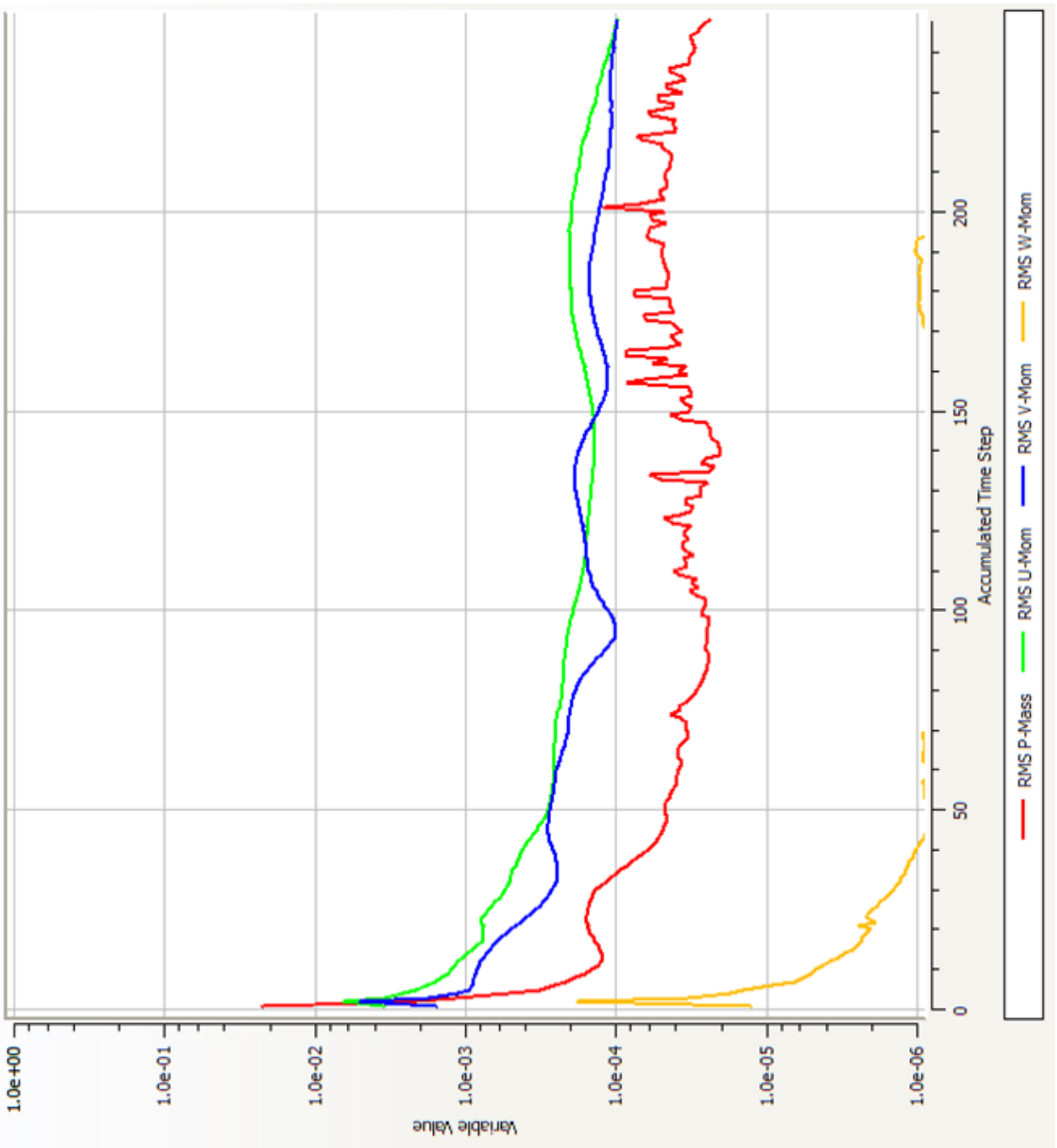

Figure 7.8: Residual Convergence history for Axis-symmetric model (fine mesh), NAR 1.5

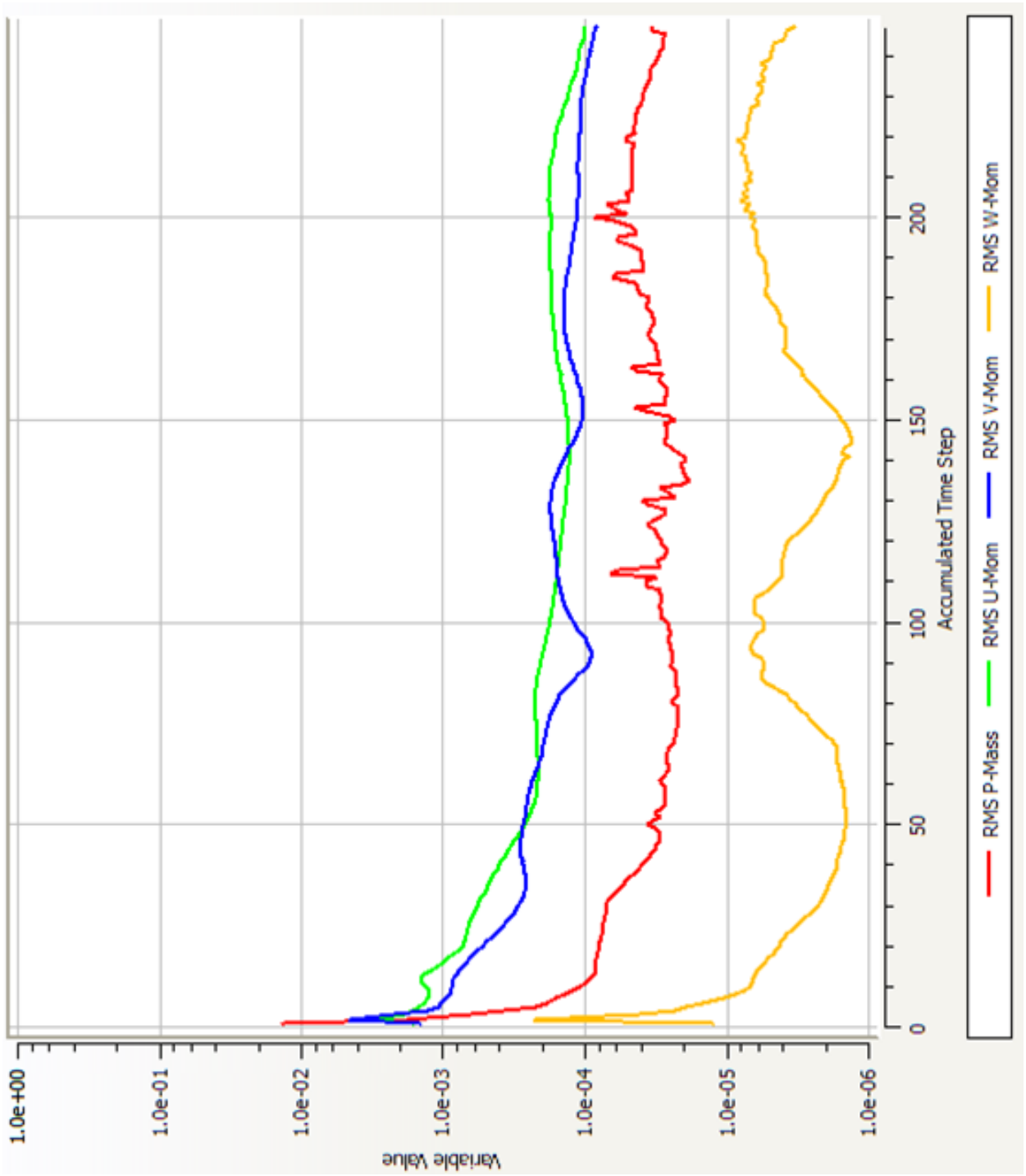

Figure 7.9: Residual Convergence history for Axis-symmetric model (very fine mesh), NAR 1.5

References

[1] 2005. http://www.aerospaceweb.org/question/propulsion/q0224.shtml.

[2] 2007. http://www.globalaircraft.org/top50.htm.

[3] 2008. www.engapplets.vt.edu/fluids/CDnozzle/cdinfo.html.

[4] 2009. http://en.wikipedia.org/wiki/File:F-22A_Raptor-03-4058.jpg.

[5] 2009. http://www.grc.nasa.gov/WWW/k-12/airplane/nozzle.html.

[6] 2009. http://en.wikipedia.org/wiki/Flow separation.

[7] 2010. http://en.wikipedia.org/wiki/Propelling-nozzle.

[8] 2010. http://personalpages.manchester.ac.uk/staff/david.d.apsley/lectures/comphydr/introcfd.pdf.

[9] 2010. ANSYS CFX Help Guide - Solver Thoery Guide, Section - 10.1.1; ANSYS Release 13.0.

[10] 2011. http://www.computationalfluiddynamics.com.au/tips-and-tricks/.

[11] 2011. http://en.wikipedia.org/wiki/Turbulence kinetic energy.

[12] J.D. Anderson. *Modern Compressible Flow with Historical Perspective*. McGraw -Hill, 3rd edition, 2003.

[13] A.H. Bowers, G.K. Noffz, S.B. Grafton, M.L. Mason, and L.R. Peron. Multiaxis thrust vectoring using axisymmetric nozzles and postexit vanes on an f/a -18 configuration vehicle. *NASA Technical Memorandum 101741*, April 1991. Technical notes.

[14] E.M.S. Ekanayake, J.A. Gear, and Y. Ding. Flow simulation of a two dimentional rectangular supersonic convergent divergent nozzle. *ANJIAM Journal 2009*, pages C377–C392, 2009.

[15] E.M.S. Ekanayake, J.A. Gear, and Y. Ding. Numerical simulation of a supersonic convergent divergent nozzle with divergent angle variations for underexpanded condition. *17th Australasian Fluid Mechanics Conference Proceedings*, 51, 2010. 327 paper.

[16] G. Eric, T. Dwain, and D. Rich. Nozzle selection and design criteria. *AAIA-2004-3923*, 2004.

[17] Gear J.A. 2007. Lecture notes of Continuum Mechanics, RMIT University.

[18] A. Jiyuan Tu, Guan H. Y., and L. Chaoqun. *Computational Fluid Dynamics - A Practical Approach*. Elsevier, 1st edition edition, 2008.

[19] A.A. Khan and T.R. Shembharkar. Viscous flow analisys in a convergent-divergent nozzle. *Proceedings for International Conference on Aerospace Science and Technology, Bangalore, India*, (IN-CAST 2008-004), 26-28 June 2008. http://nal-ir.nal.res.in/4982/01/INCAST-004.pdf.

[20] E. Luke and X.L. Tong. Turbulence models and heat transfer in nozzle flows. *AIAA Journal*, 42(11), 2004. Technical notes.

[21] N. Menon and Skews B.W. Rectangular underexpanded gas effects: effect of pressure ratio, aspect ratio and mach number. *Shock Waves 1, 26th International Symposium on Shock Waves.*, 2, 2008.

[22] N. Menon and Skews B.W. Effect of nozzle inlet geometry on underexpanded supersonic jet characteristics. *Shock Waves 1, 26th International Symposium on Shock Waves.*, Volume 2:pp 955–960, 2009.

[23] F. R. Menter, M Kuntz, and Langtry R. Ten years of industrial experience with the sst turbulence model. *Turbulence, Heat and Mass Transfer 4*, 2003. http://cfd.mace.manchester.ac.uk/flomania/pds-papers/file-pds-1068134610Menter-SST-paper.pdf.

[24] A. Mohamed and Hamed A. Supersonic rectangular over-expanded jets of single and two-phase flows. *American Institute of Physics- Physics of Fluids -Issue 12.*, ISABE 2003-1119, 2003.

[25] Y. Otobe, H. Kashimura, S. Matsuo, T. Setoguchi, and H.D. Kim. Influence of nozzle geometry on the near-field structure of a highly underexpanded sonic jet. *Journal of Fluids and Structures,Pages 281 - 293*, Volume - 24, February 2008.

[26] K.M. Pandey, J. Rajshekharan, and S. Roga. Wall static pressure variation in sudden expansion in flow through de laval nozzles at mach 1.74 and 2.23 in circular ducts without cavities: A fuzzy logic approach. *International Journal of Soft Computing and Engineering (IJSCE)*, ISSN: 2231 - 2307, Volume - 2, Issue - 1, 2012.

[27] D. Papamoschou and A. Johnson. Unsteady phenomena in supersonic nozzle flow separation. *36th AIAA Fluid Dynamics Conference and Exhibit AIAA 2006-3360*, June 2006.

[28] D. Papamoschou and A. Zill. Fundamantal investigation of supersonic nozzle flow seperation. *AAIA 2004-1111*, 2004. http://supersonic.eng.uci.edu/download/20041111.pdf.

[29] K. Teshima. Structure of supersonic freejets issuing from a rectangular orifice. *Progress in Astronautics and Aeronautics.*, Volume -185:pp 375–380, 1994.

[30] Wlezien R. W. and Kibens. V. Influence of nozzle asymmetry on supersonic jets. *AIAA Journal.*, 26(1), January 1988.

[31] Q. Xiao, H.M. Tsai, and D. Papamoschou. Numerical investigation of supersonic nozzle flow seperation. *AIAA Journal*, 45(3), March 2007.

[32] Q. Xiao, H.M. Tsai, and D. Papamoschou. Numerical study of jet plume instabilty from an overexpanded nozzle. *45th Aerospace science Meeting and Exhibit, AIAA 2007-1319 Journal, Reno Nevada*, 8 - 11 January 2007.

[33] Q. Xiao, H.M. Tsai, D. Papamoschou, and A. Johnson. Experimental and numerical study of jet mixing from a shock-containing nozzle. *Journal of Propulsion and Power*, 25(3), May - June 2009.

[34] Ding Y. 2007. CFD in Engineering Modelling, Lecture notes of MATH 2175, RMIT University.

[35] K. B. Yuceil and Otugen M.V. Scaling parameters for underexpanded supersonic jets. *American Institute of Physics- Physics of Fluids -Issue 12.*, 14, 2002.